Title	Natural Ventilation Assessment using Computational Fluids Dynamics to Improve Air Quality in Urban Areas
Author(s)	Gonzalez Olivardia, Giselle Franchesca
Citation	大阪大学, 2021, 博士論文
Version Type	VoR
URL	https://doi.org/10.18910/82243
rights	
Note	

Doctoral Dissertation

Natural Ventilation Assessment using Computational Fluids Dynamics to Improve Air Quality in Urban Areas

GONZALEZ OLIVARDIA FRANCHESCA GISELLE

January 2021

Division of Sustainable Energy and Environmental Engineering
Graduate School of Engineering
Osaka University

ACKNOWLEDGEMENTS

I want to acknowledge the following people who have supported me, not only during my studies but also throughout my life in Japan.

Firstly, I would like to express my gratitude to my supervisor Professor Akira Kondo, for his unwavering support, guidance, and insight during all these years. To Professor Tomohito Matsuo and Professor Hikari Shimadera, for patiently sharing your knowledge, pieces of advice, and comments.

I'll always be grateful for this unique opportunity to the Ministry of Education, Culture, Sport, Science, and Technology Japan and Osaka University.

I want to thank all my Japanese friends, especially my lab friends, for making me feel at home even in a place very far from home, for their kindness, and for showing me all the beauty of the Japanese culture.

And finally, I would like to express my deepest gratitude to my family; you made this crazy journey called life worthwhile.

SUMMARY

Urban areas represent a major environmental challenge because the degradation of the air quality in urban environments could impact a great part of the global population. The dispersion of air pollutants in urban areas is conditioned by the interaction of three main factors: the pollution sources, the urban form and components, and meteorological variables. Appropriate quantitively and qualitatively assessment of these interactions will allow better urban planning practices to reduce air pollution in cities.

In chapter 3, a qualitative and quantitative assessment of the interaction between meteorological variables and the urban form and components is evaluated. Three ideal urban environments are studied to investigate urban features such as building packing density, street width, and building heights, and the relationship with meteorological variable. Also, two real urban environments located in Osaka city, Osaka prefecture, Japan are presented. The locations are selected with the purpose of identify the variables influencing the ventilation efficiency in urban areas. For these scenarios the performance of three ventilation efficiency indices —the local age of air, the purging flow rate, and the air exchange efficiency— were evaluated. For the ideal urban environment —Case A, Case B, and Case C— the relationship between the street width was directly related with the local age of air, so when the street is narrower the time required to refresh the same space takes 192 seconds as it is in Case C. When the streets widener, the local age of air decreases to 188 seconds for Case B and 149 seconds for Case A. For the real urban environment, the time required for Hiranomachi (128 seconds) is more than four times the required to clean the air in Maishima (30 seconds). The results showed the influence of the number of building and building height on the capacity of the wind to refresh the urban environment. The purging flow rate, which represents the ability at which the wind can remove pollutants from the domain, for the ideal urban environment was 3252 m^3/s, 2577 m^3/s, and 2521 m^3/s for Case A, Case B and Case C, respectively. For the actual urban environment, the purging flow rate for Maishima analysis domain was 32377 m^3/s meanwhile Hiranomachi was 5220 m^3/s. The air exchange efficiency for the ideal urban environment was 31 % for Case A, 30 % for Case B, and 30 % for Case C. The actual urban environment air exchange efficiency was 35 % and 77 % for Hiranomachi and Maishima, respectively. The air exchange efficiency results indicated to have a low air exchange efficiency (apart from Maishima). The results indicated that the local age of air, the purging flow rate, and the air exchange efficiency are ventilation efficiency indices that can help describe characteristics of urban environments. However, the air exchange efficiency requires further considerations.

Also, the results indicated that similarly when the spread of contaminants is diminished for certain packing densities, same occurs to street widths.

In Chapter 4, the interaction between meteorological variables —wind speed— and urban component —urban intersections— were quantitative and qualitative assessed to know the role in the distribution of pollutant in secondary streets, and the influence of emission sources. In urban intersections, the ventilation efficiency was evaluated using the local age of air. The urban environment consisted in an idealized building blocks of packing density ($\lambda_p = 0.25$) with a four-way intersection of two perpendicular (90°) streets. The results indicated that the intersection with the best ventilation was Case 1a–intersection A for the different wind conditions evaluated.d Additionally, the results indicated that intersection A in Case 1a, intersection B in Case 1b, and intersection A and intersection B in Case 1c improved their pedestrian ventilation proportionally with the wind velocity increment. In summary, the variation of the inlet wind velocity —meteorological variable— has little influence on the contaminant's displacement to secondary streets. Also, the variation of the inlet wind velocity —meteorological variable— reduce the levels of pollutants but does not alter the distribution of contaminants in the intersections.

In chapter 5, a description of the interaction between the emission source, urban form and components and meteorological variables was presented. The emission source was evaluated considering reactive pollutants (nitrogen monoxide, nitrogen dioxide and ozone) in a realistic urban environment located in Umeda Shin-Michi, Osaka Prefecture Japan. A 24 hours simulation by integrating a CFD model coupled with a chemical reaction model (CBM-IV), a radiation model, and boundary conditions from WRF-CMAQ was conducted. The results indicated that the production of NO_x or fading of O_3 were especially found in regions with low wind speed and high turbulence. Also, the distribution of O_3 was directly affected by chemical reactions near the roadside, where fresh NO was being emitted (NOx titration). The same urban form under different meteorological variables — wind speed, wind direction— and emission rates leads to very different patterns of distribution of contaminants during the day.

Considering that in the following decades, accelerate urbanization will take place mainly in developing countries where access to this type of analysis is very scarce. Further studies about the interaction of emission sources, meteorological variables, and urban form and components will be highly beneficial. It is encouraged to pursue future investigations that evaluate the variation of the urban forms and components (introduction of urban trees, open spaces, water bodies, building packing density), and different meteorological variables (wind direction, humidity, temperature), and other types of ventilation efficiency indices. Moreover, the availability of experimental data (wind tunnels, on-site measurements) will further advance CFD modelling as a reliability tool to study the urban environment. Finally, we can conclude that the study of the urban areas is imperative because architects, researchers, city designers, government, engineers, and all the institutions involved in the urban development process would benefit from a more comprehensive understanding of the urban area dynamics.

CONTENTS

TABLE OF FIGURES

TABLE OF SYMBOLS

ε_a	:	Air exchange efficiency
$\overline{C_p}$	:	Average over the dataset of the model predictions
$\overline{C_o}$	:	Average over the dataset of the observations
τ_{exc}	:	Average time of exchange of air or contaminant
F	:	Body force per unit mass, for example the volume force
λ_p	:	Building packing density
α_{bs}	:	Building surface albedo
C_H	:	Bulk heat transfer coefficient
x_i	:	Cartesian space coordinate
$\alpha, \beta, \sigma, \sigma_d$	:	Closure coefficients in the specific dissipation-rate equation
β^*, σ^*	:	Closure coefficients in the turbulence-kinetic-energy equation
C_1, C_2, C_μ	:	Coefficients in approximated turbulent transport equations
$C(t)$	:	Concentration at steady state
c_p	:	Concentration of the contaminant leaving the control volume
q	:	Conductive heat flux vector
ρ	:	Density
D	:	Diffusivity (also called diffusion coefficient)
$\nabla \cdot$	:	Divergence
$R \downarrow$	:	Downward longwave radiation
C_f	:	Drag coefficient for canopy
$\dot{m}$	:	Effective uniformly distributed emission rate
EI	:	Emission intensity
E_{vol}	:	Emission volume
n	:	Empirically known constant
η	:	Fraction of the area covered with trees
G_b	:	Generation of turbulent kinetic energy due to buoyancy
G_k	:	Generation of turbulent kinetic energy due to mean velocity gradient
∇	:	Gradient
g	:	Gravity
α_g	:	Ground albedo
Q_w	:	Heat flux from the building into the air
Q_G	:	Heat flux into the ground
L_x, L_y	:	Horizontal dimension of roughness (building) element
D_x, D_y	:	Horizontal distance between centers of consecutive roughness (building) elements
U_{in}	:	Inlet wind velocity
u	:	Instantaneous velocity
u'	:	Instantaneous velocity fluctuation
e	:	Internal energy per unit mass
a	:	Leaf area density depending on the tree species
$\bar{\tau}_p$	:	Local age or air
c	:	Local concentration
$\langle\bar{\tau}\rangle$	:	Mean internal age or mean age of air

$\bar{u}$	:	Mean velocity
C_p	:	Model predictions
μ	:	Molecular viscosity
S_{chem}	:	Net chemical production rate of the species calculated by the CBM-IV model
τ_n	:	Nominal time constant
C_n	:	Normalized concentration
U_n	:	Normalized wind velocity
C_o	:	Observations
A_p	:	Plan area of roughness (building) elements
A_T	:	Plan area of total surface
P	:	Pressure
U_p	:	Purging flow rate
Z_{ref}	:	Reference height
l	:	Reference length scale
$\bar{\tau}_{p,ref}$	:	Reference local age of air
U_{ref}	:	Reference wind velocity
$\dot{m}_p$	:	Release rate
H	:	Sensible heat flux
τ	:	Shear stress
$S\downarrow$	:	Shortwave radiation
$f_{i,sky}$	:	Sky view factor for element *i*
R	:	Source of the variable c
c_p	:	Specific heat at a constant pressure
ω	:	Specific rate of dissipation
σ	:	Stefan-Boltzmann constant
i, j, k	:	Subscripts denoting Cartesian coordinate directions
T_{ao}	:	Temperature of air above T_{bso}
T_i	:	Temperature of an element in the ground surface
T_j	:	Temperature of surface *j*
T_{bso}	:	Temperature of the outer building wall
t	:	Time
Δt	:	Time step of the simulation
σ	:	Total stress tensor
I	:	Turbulence intensity
μ_t	:	Turbulent (eddy) viscosity
ε	:	Turbulent dissipation rate
k	:	Turbulent kinetic energy
c	:	Variable de interest (for this work, concentration)
$f_{i,j}$	:	View factor of each surface element *j* from element *i*
vol	:	Volume of the four intersections 4W × 4W × 0.25H

ABBREVIATIONS

A/A	:	Air conditioner
ASHRAE	:	American Society of Heating, Refrigerating and Air-Conditioning Engineers
ADMS	:	Atmospheric Dispersion Modeling System
AEROS	:	Atmospheric Environmental Regional Observation System
CALINE4	:	California line source dispersion model
CB05	:	Carbon Bond mechanism developed in 2005
CBM-IV	:	Carbon bond mechanism IV
CO_2	:	Carbon dioxide
CO	:	Carbon monoxide
CMAQ	:	Community Multiscale Air Quality model
CFD	:	Computational fluids dynamics
UTC	:	Coordinated Universal Time
DNS	:	Direct Numerical Simulation
FAC2	:	Fraction of predictions within a factor of two observations
FB	:	Fractional bias
GDP	:	Gross Domestic Product
HV	:	High velocity
JEI-DB	:	Japan Auto-Oil Program Emission Inventory-Data Base for vehicles
JMA	:	Japan Meteorological Agency
JST	:	Japanese Standard Time
LES	:	Large Eddy Simulation
LV	:	Low velocity
MV	:	Medium velocity
MMM	:	Mesoscale meteorological models
MOE	:	Ministry of the Environment of Japan
MOST	:	Monin-Obukhov Similarity Theory
NO_2	:	Nitrogen dioxide
NO	:	Nitrogen monoxide or nitric oxide
NO_x	:	Nitrogen oxides
O_3	:	Ozone
$PM_{2.5}$	:	Particulate matter
PFR	:	Purging flow rate
RNG	:	Re-Normalization Group
RANS	:	Reynolds-averaged Navier-Stokes
RMSE	:	Root-mean-square deviation
SIMPLE	:	Semi-Implicit Method for the Pressure-Linked Equations
SO_2	:	Sulfur dioxide
3D	:	Tridimensional
VOCs	:	Volatile organic compounds
WRF	:	Weather Research and Forecasting model
WHO	:	World Health Organization

CHAPTER 1. INTRODUCTION

1.1. Background

Urban areas are defined as a limited region with a characteristic built-up infrastructure, with a high density of inhabitants that serve specific economic and social functions (Weeks, 2010).

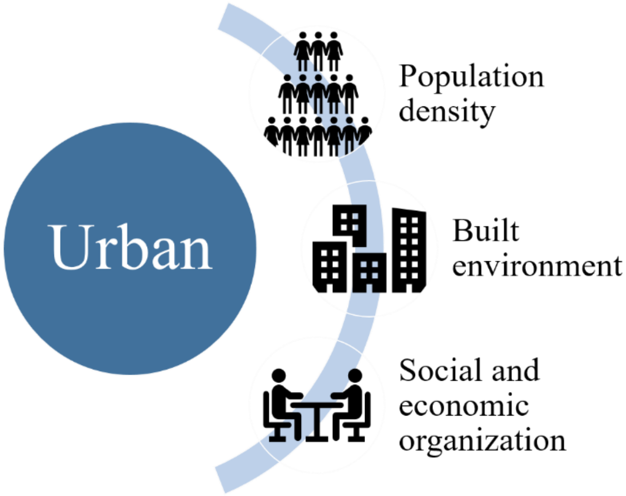

Figure 1.1. Definition of urban.

Urban areas represent a major environmental challenge because the degradation of the urban environment could impact a great part of the global population. United Nations (2019) estimated that by the year 2007 the urban population surpassed the rural population and it is expected that by the year 2050 more of two-thirds of the world population (approx. 68%) will be residing in urban areas (Figure 1.2).

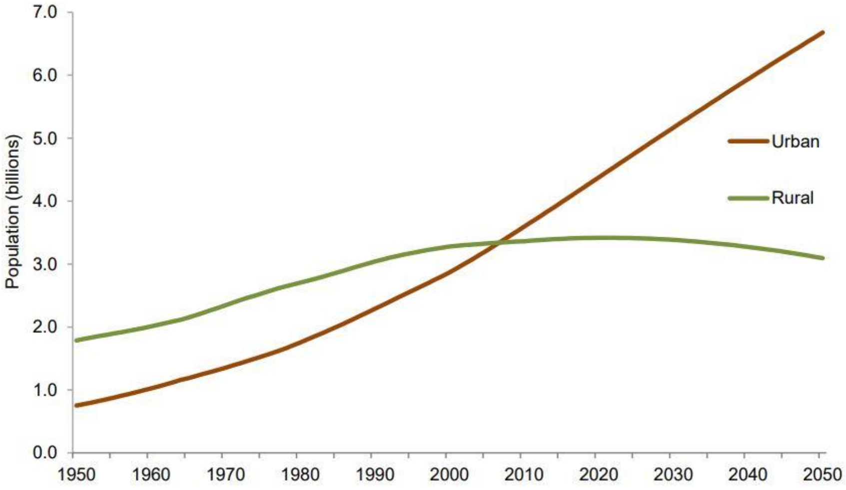

Figure 1.2. Urban and rural population of the world, 1950-2050 (United Nations, 2019).

Due to technological advancement, more regions worldwide are replacing the natural landscape with a characteristic built-up infrastructure. According to Weeks (2010), technological developments have allowed expanding the possibilities for city size and structure. For example, in the past urban areas were limited because (1) cities had to be compact enough to be traversed easily on foot; (2) roads did not have to be very wide or regular in shape because they did not have to accommodate fast-moving motorized traffic; (3) population size was limited by the ability to supply the city with water and with some way of getting rid of human waste; (4) population size was limited by the ability to supply the city with food, which in the absence of refrigeration limited locations of cities of those places near a ready agricultural supply; (5) economic activity was labor-intensive, and so there were no particular spatial advantages to having manufacturing done in the city; rather it could be ¨farmed¨ out to people living outside the city, meaning that cities were mostly service (including government and finance) and commercial centers, which limited the variability in land use.

Due to these developments, urban area size and built-up infrastructure have been horizontally (sprawl) and vertically (high-rise buildings) expanded. However, this expansion has resonated in the quality of life of dwellers. Within urban areas, the inhabitants are exposed to mobile and stationary sources of contaminants that have negative impacts on their health. The World Health Organization (WHO (2018)) estimated that there were 1.34 million worldwide premature deaths due to urban outdoor air pollution in 2008. This number was linked to the increment in air pollution concentration, and the total population affected as cities grew. Zhang *et al.* (2007) concluded that air pollution represents a health problem and has an economic impact accounting for about 6.55% of Beijing’s gross domestic product (GDP) on average. Dauchet *et al.* (2018) studied the air pollution levels in two urban areas in northern France and showed that even the moderate air pollution levels could impact respiratory health on the general population, not only susceptible individuals. Duan *et al.* (2020) sustained the relationship between air pollution and adverse human health respiratory diseases, such as chronic obstructive pulmonary disease.

The distribution of air pollutants inside urban areas is conditioned by the interaction of three main factors: the pollution sources, the urban form and components, and meteorological variables (Figure 1.3). Many studies have addressed these three factors to determine their relationship and predict air pollution dispersion by knowing their behavior.

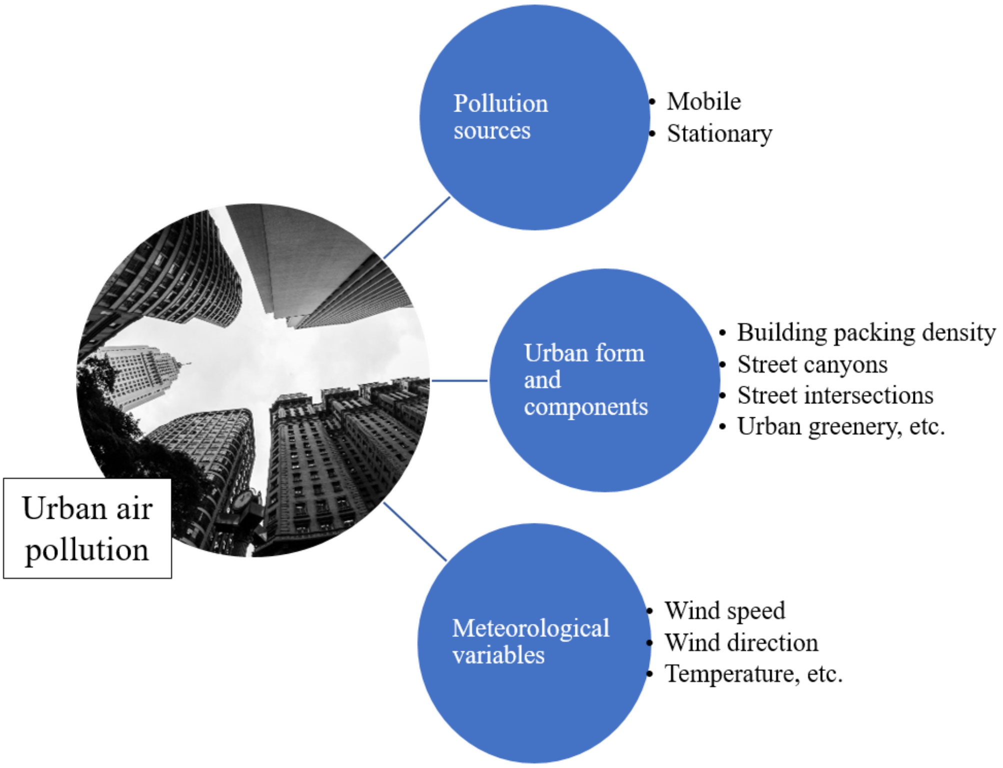

Figure 1.3. The main three factors involved in the urban air pollution: pollution sources, urban form and components, and meteorological variables.

Some recent works have addressed the interaction of two or more of these three factors inside urban areas:

- Brady and O'Mahony (2011) studied how the introduction of electric vehicles — mobile pollution source— could improve urban air quality. The results indicated a net reduction of 3% in carbon dioxide (CO_2) could be observed in the most likely scenario, but the benefits could only be seen after ten years when the current fleet might be gradually replaced by electric vehicles.
- Yuan *et al.* (2018) studied the relationship between urban form and particulate matter ($PM_{2.5}$) concentration in 269 prefectural-level cities in China using spatial regression models. When planning the urban form, they found that considerations about road traffic, green land spaces, buildings, and urban heat island effect are binding because they might arouse haze pollution in small, medium, and large cities.
- Y. Liu *et al.* (2018) analyzed 83 cities in China. They found that urban air pollution increases with city size, and the relationship between the urban form and air pollution changed depending on the season and the monsoons.

- Paraschiv and Paraschiv (2019) investigated the temporal distribution of nitrogen dioxide (NO_2) in two urban areas in Romania during 2016 and 2017 and concluded that the traffic emissions had a higher contribution than the industrial type. Also, they pointed out that emissions control systems improved NO_2 emission, but it is not enough to reduce the NO_2 concentration.
- Gao *et al.* (2019) evaluated the air pollution distribution of $PM_{2.5}$ in two Shanghai communities, using a generalized additive model and land-use regression. They found that the $PM_{2.5}$ variation in central urban communities was related primarily to traffic volume and was also significantly influenced by the building heights, local traffic, and commercial pollution sources. In contrast, the $PM_{2.5}$ background level was the key factor impacting the $PM_{2.5}$ variation in the suburban study area. The authors recommend to strength the outdoor ventilation via intervening urban forms to change $PM_{2.5}$ levels.
- Li *et al.* (2019) studied the relationship between air pollution and urban form. They concluded that the distance to primary road, the standard deviation of building floors, and average building floors were the most important features affecting the spatial variations of the eight pollutants analyzed. However, the standard deviation of building floors, the average building floors, and the building density played significant roles in dispersing the pollutants, except ozone (O_3) and particulate matter ($PM_{2.5}$). They also identified wind ventilation as a critical index for air quality-oriented urban design.

Understanding the interaction of the pollutant sources, urban form and components, and the meteorological variables, besides appropriate quantitively and qualitatively assessment of these interactions will allow better urban planning practices to reduce air pollution in cities.

1.2. Aims of the research

The present study has recognized the prominence of natural outdoor ventilation to reduce air pollution in urban areas. The idea is that cool sea or rural breeze intentionally induced into the polluted urban area, through proper urban planning, could reduce air pollution inside urban environments in a natural way.

Studies have shown that enhancing the natural wind not only helps with the reduction of the air pollution and urban heat island levels (Rao, 2014), it may also contribute to improving the indoor air quality and indoor thermal conditions, considering that the demand for air conditioning will also decrease (Santamouris, 2006). In the past, Akashi recognized that the sea breeze has a certain influence (2°C) on the outdoor temperature of urban built-up areas, and the breeze flows are affected by the locations and shapes of the artificial structures as buildings and elevated highways. Wong (2012) reported the urban ventilation could be used as a countermeasure for heat island for high-density cities. Adequate urban living spaces can be achieved by combining town planning and urban design, building design, and transport planning supported by policies on energy, transportation, land administration, environmental protection, and others. Kittaka and Miyazaki (2014) indicated by a study in Osaka Center City that the wind by itself influences the built-up areas, but its direction plays a role in the temperatures. Kubota and Ahmad (2006) evaluated the urban configuration for a major town in Malaysia based on the wind properties. Some of their conclusions were that the wind flow plays an important role in diffusing air pollution and heat at urban scale as well as a neighborhood scale. Rajagopalan *et al.* (2014) concluded from their investigation in Malaysia of various urban geometry that the step-up configuration was the most practical geometry, allowing the wind to reach even the leeward side of each building in a typical tropical city. Gál and Unger (2009) identified potential ventilation paths of the city presenting the urban roughness mapping method and concluded that ventilation paths could play an important role in developing the urban heat island circulation and reduce air pollution in the inner part of Szeged city in Hungary. Meanwhile, Hsieh and Huang (2016) studied ventilation paths expected to draw in breezes from suburban areas and the sea to mitigate the urban heat island effect.

In addition to the benefits that harnessing the urban ventilation could represent in air pollution levels, some studies have indicated that ventilation efficiency indices are able to describe some characteristics of the urban environment (Peng *et al.*, 2020). Ventilation efficiency indices, mainly known for indoor applications, have been employed to evaluate the ventilation performance and air quality in outdoors settings (Bady *et al.*, 2008; Hang and Li, 2011; Hang *et al.*, 2009a).

For example, Buccolieri *et al.* (2010) used a ventilation efficiency index to define the city "breathability" term that measures the ventilation in the city. The results showed the methodology was practical, but the application of these results to real scenarios require further analyses. Moreover, Ramponi *et al.* (2015) specified that outdoor ventilation is very important for a healthy and livable urban environment, but indicated the lack of studies for urban configurations with heterogenous characteristics.

This doctoral dissertation attempts to use computational fluids dynamics (CFD) to accomplish two main objectives: (1) to quantitatively assess the ventilation performance of urban areas using suitable ventilation efficiency indices and (2) to model in a more comprehensive way the urban environment processes and their influence on the dispersion of pollutants to reduce urban air pollution levels.

1.3. Scope of research

This doctoral dissertation is divided in three chapters. In chapter 3, a qualitative and quantitative assessment of the interaction between meteorological variables and the urban form and components is evaluated. Three ideal urban environments are studied to investigate urban features such as building packing density, street width, and building heights, and the relationship with meteorological variable and determine the ventilation efficiency indices. Also, two real urban environments located in Osaka city, Osaka prefecture, Japan are presented. The locations are selected with the purpose of identify the variables influencing the ventilation efficiency in urban areas. For these scenarios the performance of three ventilation efficiency indices —the local age of air, the purging flow rate, and the air exchange efficiency— were evaluated.

Moreover, the interaction between meteorological variables and urban form were indicated. The meteorological variable, in this case wind, was modified and the urban components was kept the same. Urban intersections were quantitative and qualitative assessed to know the role in the distribution of pollutant in secondary streets, and the influence of emission sources. In urban intersections, the ventilation efficiency was evaluated using the local age of air.

A description of the interaction between the emission source, urban form and components and meteorological variables was introduced in chapter 5. The emission source was evaluated considering reactive pollutants (nitrogen monoxide, nitrogen dioxide and ozone) in a realistic urban environment. The urban environment was located in Umeda Shin-Michi, Osaka Prefecture Japan.

All the cases were conducted using Reynolds-Averaged Navier-Stokes (RANS) equations, so time-average values were investigated. Some simplification to the domain size and mesh were adopted in this research. All the simulations were for three dimensional layouts.

This work highlights attention to environmental issues such as the urban air pollution assessment and extent the modelling for fields such as wind engineering and urban form and components aerodynamics. Furthermore, despite all the methodologies that have stated how important is to harness the natural wind inside urban areas, the field still requires further considerations to evaluate the very unique characteristics of urban environments.

The study of the urban areas is imperative because architects, researchers, city designers, government, engineers, and all the institutions involved in the urban development process would benefit from a more comprehensive understanding of the urban area dynamics.

1.4. Outline of the thesis

The chapters in this doctoral thesis are organized in the following way. The first chapter introduces the theme of this doctoral dissertation. It is divided into sections to provide background, the aim of the research, and the research scope. A review of the urban environment modeling was documented in the second chapter, including the equations employed. The third chapter refers quantitative and qualitative assessment of the relationship between meteorological variables and urban form and components using ventilation efficiency indices to study the urban environment. The fourth chapter also evaluates quantitative and qualitative the meteorological variables and urban components, especially urban intersections, emission sources, and their role in distributing urban pollutants. The fifth chapter qualitative assess the interaction between meteorological variables, urban form and components and pollution sources and their influence of the urban form in reactive pollutants. In the last chapter, some findings, conclusions, and recommendations are mentioned.

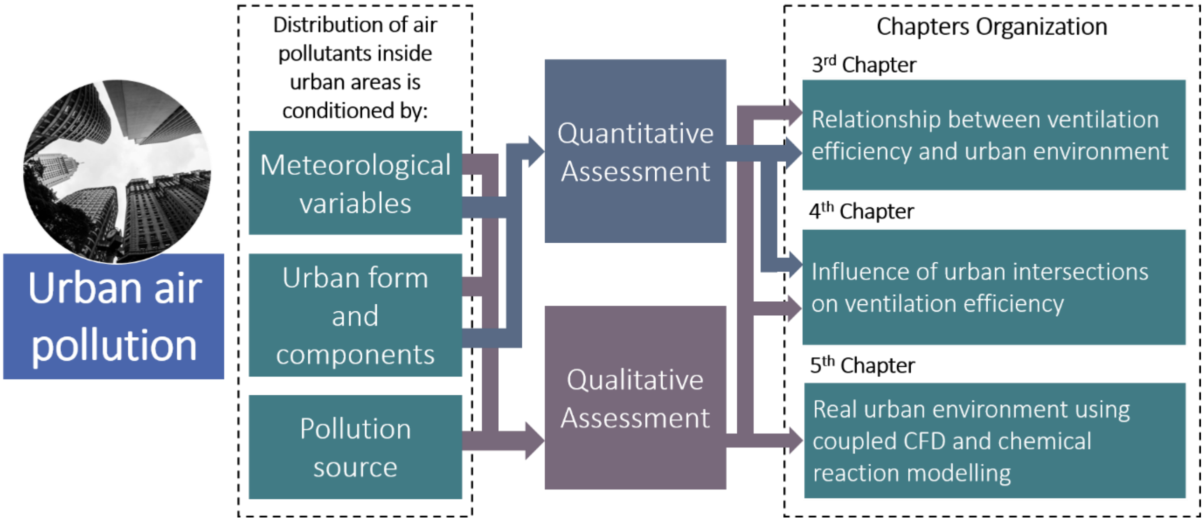

Figure 1.4. Outline of this doctoral dissertation

CHAPTER 2. MODELING THE URBAN ENVIRONMENT

2.1 Urban areas modelling scales

In climate modeling, the atmospheric phenomena are categorized in different spatial scales: mesoscale (< 200 km), microscale (< 2 km), building (< 100 m), and indoor (< 10 m) (Blocken, 2015; Toparlar *et al.*, 2017). On the other hand, Hang *et al.* (2015) defined the microscale size as lower than 10 km to 100 m and subdivided the microclimate as city-scale (up to 10 km), neighborhood-scale (up to 1 km), and street-scale (up to 100 m). These spatial scales are related to model categories. For example, mesoscale is simulated using mesoscale meteorological models (MMM), and microscale with CFD (Blocken, 2015). However, there is not a general standard about size and range for each model application. Recently, models of different scales are coupled so they can be used as boundary conditions (Baik *et al.*, 2009; Kwak *et al.*, 2015; Tewari *et al.*, 2010).

Urban environment modeling is usually referred to as a microscale category. In this dissertation, the terms city and microscale are used referring up to about 2 km.

2.2 Description of urban form and components

As introduced in the first chapter, the pollutant dispersion in urban areas depends substantially on urban forms and components. In this doctoral dissertation, two main urban geometries have been defined: real urban areas and ideal urban areas, and special interest have been focused on urban intersections. Moreover, urban parameters such as the urban compactness has been stablished to describe the geometric characteristics of the urban environment.

2.2.1 Real urban areas

The simulations referring to real, actual, asymmetrical, or heterogeneous urban areas are based on existing cities. The main objective of studying real urban layouts is to define the complexity of urban form and components. Toparlar *et al.* (2017) mentioned that most studies on real urban areas are conducted for locations in mid-latitude climates. They are usually referred to as study cases and could cover only a few buildings to a city portion. The performance of the simulation of the real urban environments is usually compared against on-site (field) measurements.

Real urban morphologies represent specific features found in real urban areas, and the modeling requires a higher level of analysis and complexity. One example of analysis in real urban areas (Figure 2.1) is presented by Antoniou *et al.* (2017) in Nicosia, Cyprus, categorized as low-rise and medium-rise buildings. Another example of a real urban environment is the study of a neighborhood area in Marylebone Road and Gloucester in central London, United Kingdom (Di Sabatino *et al.*, 2017; Panagiotou *et al.*, 2013).

a)

Aerial view of Nicosia, Cyprus

Computational representation of Nicosia, Cyprus

b)

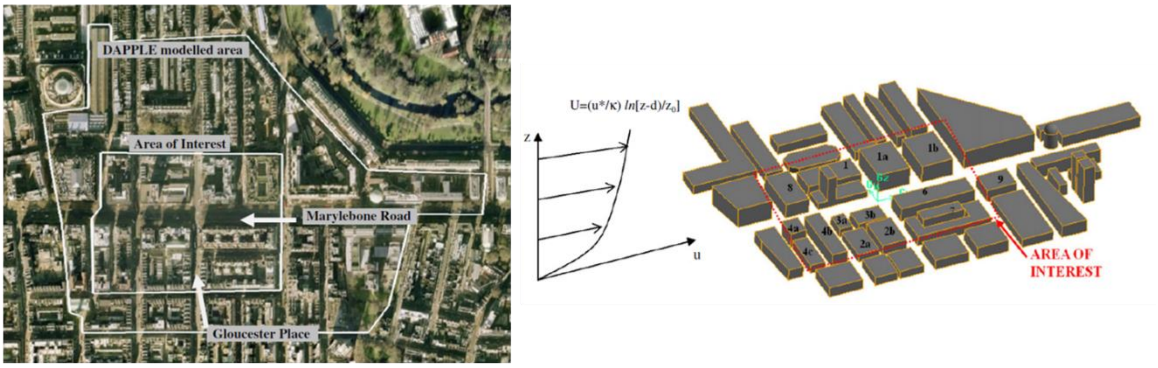

Aerial view of Marylebone Road and Gloucester Place, Central London (UK)

Computational representation Marylebone Road and Gloucester Place, Central London (UK)

Figure 2.1. Real urban environments: (a) Aerial view of Nicosia, Cyprus (left), computational representation of Nicosia, Cyprus (right) (Antoniou *et al.*, 2017), (b) Aerial view of Marylebone Road and Gloucester Place, Central London (UK) (left), computational representation of Marylebone Road and Gloucester Place, Central London (UK) (right) (Panagiotou *et al.*, 2013).

2.2.2 Ideal urban areas

It is common to find in the literature related to urban environments the simplification of urban geometry. These simplifications are sometimes considered ideal scenarios, regular or generic geometries. Studies using CFD for generic urban areas typically comprise simple building shapes, such as cubes or rectangular prisms (Figure 2.2).

Early CFD models employed for microclimate analysis considered generic domains for model development and validation purposes. Later studies were generally conducted to investigate generic aspects of fluid flow or heat transfer in urban areas that can provide basic insights to understand real urban areas processes (Toparlar *et al.*, 2017). The studies about ideal urban areas are usually simplified depending on the urban form to be evaluated: round simple city, square simple city, and long simple rectangular city (Hang *et al.*, 2009a, 2009b), urban-like geometries (Buccolieri *et al.*, 2010), high-rise urban areas (Hang and Li, 2011), regular cubical buildings (Chen, Hang, Sandberg, Claesson, Di Sabatino, *et al.*, 2017), long street canyons (Huang *et al.*, 2019).

a)

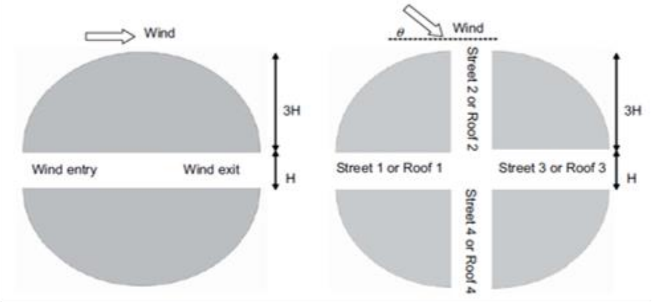

Round simple city model

b)

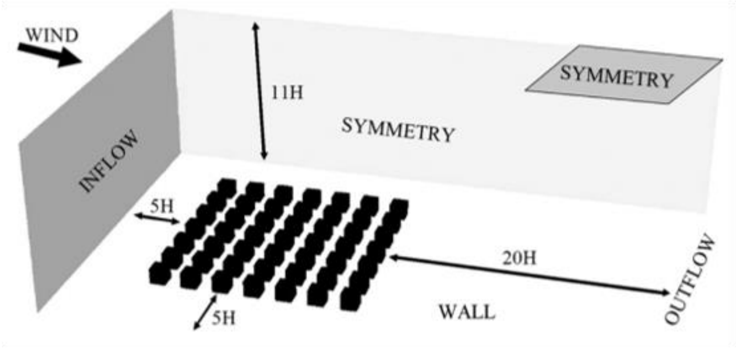

Array of cubical buildings

c)

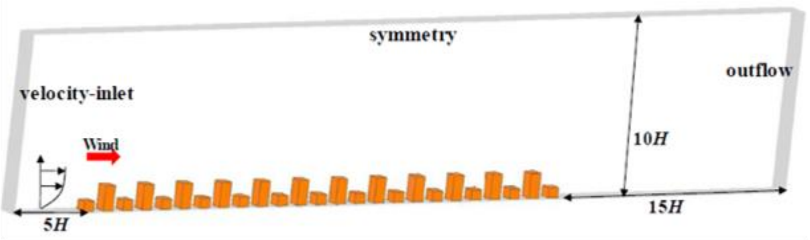

Array of buildings with height variation

d)

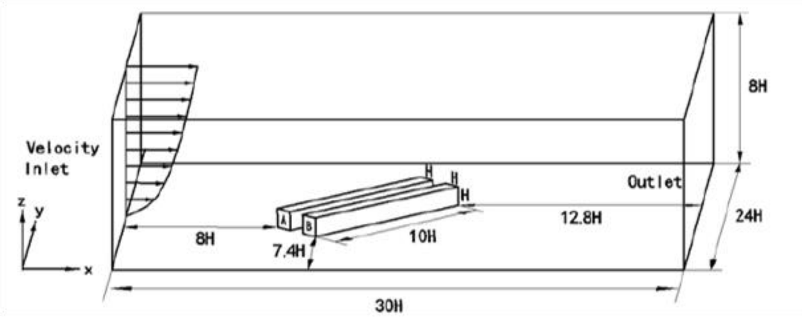

Long street canyon

Figure 2.2. Ideal urban environments: (a) Round simple city model (Hang et al., 2009a, 2009b), (b) Array of cubical buildings (Buccolieri *et al.*, 2010), (c) Array of buildings with heights variation (Chen, Hang, Sandberg, Claesson, Di Sabatino, *et al.*, 2017), (d) Long street canyon (Huang et al., 2019).

2.2.3 Urban compactness

Grimmond and Oke (1998) introduced the plan area aspect ratio λ_P (**Error! Reference source not found.Error! Reference source not found.**) to describe the aerodynamic properties of an urban area by means of its geometry characteristics. In others studies, this index is also called building packing density (Buccolieri and Sandberg, 2008; Chen, Hang, Sandberg, Claesson, and Di Sabatino, 2017) and quantifies the urban compactness of an urban area.

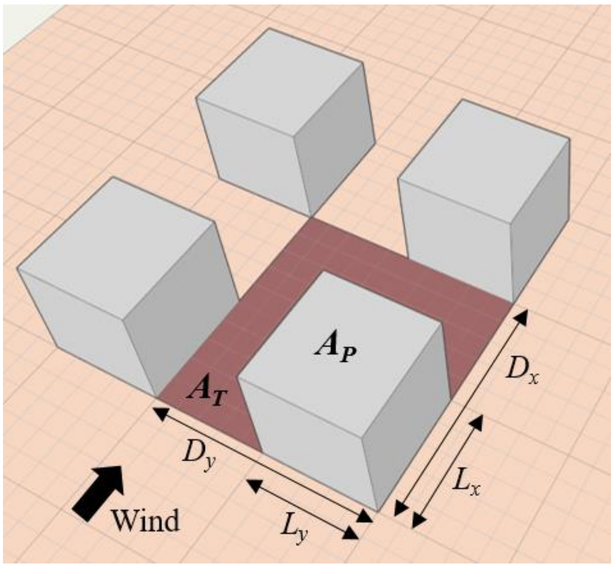

Figure 2.3. Surface dimensions used to define building packing density (Modified from Grimmond and Oke (1998).

Equation 1

$$\lambda_p = \frac{A_p}{A_T} = \frac{L_x L_y}{D_x D_y}$$

2.2.4 Urban components

The high density of inhabitants in urban areas and the type of activities they develop entails a very specific built-up infrastructure. To reduce the urban air pollution levels, special interest is focused in certain areas or components inside urban areas. In this doctoral dissertation, attention is drawn to street intersections.

2.2.4.1 Street intersections

Some studies has suggested that more scrutiny is required in street intersections (Ahmad *et al.*, 2005; Soulhac *et al.*, 2009; Yassin *et al.*, 2008) because it is a region where two or more streets connect, they are located near to emission sources, and due to the peculiar nature of the wind flow around bluff bodies. Urban street intersections change the dispersion of pollutants due to variations in wind direction (Lihua *et al.*, 2015), and shape ─regular or irregular─ (Wang and McNamara, 2007).

2.3 Urban areas modelling tools

Various tools have been employed to study the urban environment (Vardoulakis *et al.*, 2003): field observations (De Paul and Sheih, 1986; Edussuriya *et al.*, 2011; Y. Qin and Kot, 1993; Vardoulakis *et al.*, 2002), wind tunnel measurements (Ahmad *et al.*, 2005; Antoniou *et al.*, 2017; Cui *et al.*, 2016), water tunnel experiments (Ai and Mak, 2017), and several semi-empirical models including the Atmospheric Dispersion Modeling System (ADMS)-Urban dispersion model (Righi *et al.*, 2009), California Line source dispersion model (CALINE4) (Kenty *et al.*, 2007), and Urban Street Model (Taseiko *et al.*, 2009).

The methodology utilized for this study is computational fluid dynamics (CFD) modeling because it helps to reduce the time required to optimize a physical model and is less expensive in comparison with wind tunnels. Moreover, the simulation of dispersion and boundary conditions with CFD are better studied (Leitl and Meroney, 1997).

Recent advances in computer technology make CFD a powerful tool for air pollution modeling (Baik *et al.*, 2003; Kim and Baik, 1999); using CFD, the description of air flow patterns at the city-block scale with high spatial-resolution can be achieved (Solazzo *et al.*, 2011), and important simulations such as the influence of building geometry on wind flow and heat convection can be carried out (Dayang *et al.*, 2012; Vollaro *et al.*, 2015).

2.3.1 Computational fluids dynamics

Computational fluids dynamics is the combination of fluids dynamics, numerical mathematics and computer science. Some of the advantages is that offers information about the entire domain, generating more data, also it allows easier modification of the study case in order to investigate different physical behaviors. To model the urban environment the main equations in fluids dynamics are describe as followed.

Conservation of mass

The conservation of mass (Equation 2) implies that the quantity of mass in a system remains unchanged. Despite the chemical reactions, no mass is lost or gained, and no atomic species are transformed, so mass is conserved. In the context of CFD, atomic species are preserved, though chemical species can react (Rodriquez, 2019).

Equation 2

$$\nabla \cdot u = 0$$

For an incompressible fluid, this term in Equation 2 represents the overall rate of mass addition per unit volume due to convection.

Conservation of momentum

The conservation of momentum (Equation 3) is based on the idea that momentum it is neither destroyed nor created but rather it is transformed from one type of momentum onto another. That is, the fluid experiences various body and surface forces that inevitably generate motion. Body forces refers to those forces that act directly upon the entire mass enclosed by the volume (system) in question, such as gravity and electromagnetic forces. Surface forces refer to those forces that act on the surface of the volume. Surface forces include two categories: pressure as a result of the action from the surrounding fluid and the viscous shear/normal stresses caused by frictional forces (Rodriquez, 2019).

Equation 3
$$\rho \frac{\partial u}{\partial t} + \rho u \cdot \nabla u = -\nabla \cdot \tau - \nabla P + \rho g$$

The first term represents the rate of momentum accumulation per unit volume, when there is no net change with respect to time, the system is said to be at steady state. The second term is the rate of momentum change due to convection per unit volume, the third term is rate of momentum change per unit volume due to viscous forces, the fourth term is rate of momentum change per unit volume based on pressure gradients. The last term, is the momentum rate of change based on gravity, per unit volume, and it is important during buoyant flows.

Further considerations are need it to solve the conservation of momentum equation for fluids, especially the third term in Equation 3. So, depending on the type of fluid, they can be modelled as Newtonian or non-Newtonian fluid. In this study the air is modeled as a Newtonian fluid, so the stress is linearly proportional to the velocity gradients, the fluid shear (Equation 5 and Equation 5):

Equation 4
$$\tau_{ij} = 2\mu s_{ij} - \frac{2}{3}(\nabla \cdot u)\delta_{ij}$$

Equation 5
$$s_{ij} = \frac{1}{2}\left(\frac{\partial u_i}{\partial x_j} + \frac{\partial u_j}{\partial x_i}\right)$$

Conservation of energy

Another equation important to consider in the study of the urban environment if considerations about temperature are need it is the conservation of energy or heat transfer (Comsol, 2020). Equation 6 is the equation for conservation of total internal energy:

Equation 6
$$\rho \frac{\partial}{\partial t}\left[\left(e+\frac{1}{2}u^2\right)\right]+\nabla\cdot\left[\rho u\left(e+\frac{1}{2}u^2\right)\right]=$$
$$-\nabla\cdot q+\nabla\cdot(\sigma\cdot u)+\rho u\cdot F$$

The first term represents the rate of increase of energy per unit volume, the second term is the convection of energy into a point by flow, the third term is the net heat flux, the fourth term is the work surface forces and the fifth is the work of body forces.

Scalar transport equation

The scalar transport equation, also known in some cases as convection (advection)-diffusion equation (Socolofsky and Jirka, 2004).

Equation 7
$$\frac{\partial c}{\partial t}+\nabla\cdot(uc)=D\nabla^2 c+R$$

The first term represents the rate of increase of the scalar in the fluid element, the second term is the net rate of flow of the scalar out of the fluid element, the third term represents the increase of the scalar due to diffusion and the last term represents the rate of increase of the scalar due to a source.

The urban environment modeling of airflow mainly obeys a highly turbulent flow, because of the typical urban built-up infrastructure —bluff bodies—, so the airflow suffers irregular fluctuations. Turbulent flows are inherently three-dimensional, time dependent and the motion of eddies can be very intense, resulting in vigorous mixing and effective turbulent stresses.
A methodology to solve these instabilities is a set of time-averaged equations called the RANS equations. They consist in model the turbulence over a long period of time, allowing the behavior to be time-averaged (Figure 2.4). Then, Osborne Reynolds proposed the decompositions of instantaneous flow into an average quantity and its associated fluctuating quantity (Equation 8) (Rodriquez, 2019).

Equation 8
$$u=\bar{u}+u'$$

The last term is intended to quantify the eddy fluctuations. The majority of the engineering applications are satisfied with time-averaged properties of the flow (mean velocities, mean pressures, mean stresses, etc.). Even when RANS based turbulence models do not perform better that other turbulence models such as Large Eddy Simulation (LES) or Direct Numerical Simulation (DNS) (Tominaga *et al.*, 2008; Tominaga and Stathopoulos, 2010, 2012, 2013) some authors have preferred RANS for engineering practices (Ben Ramoul *et al.*, 2018; Toparlar *et al.*, 2017).

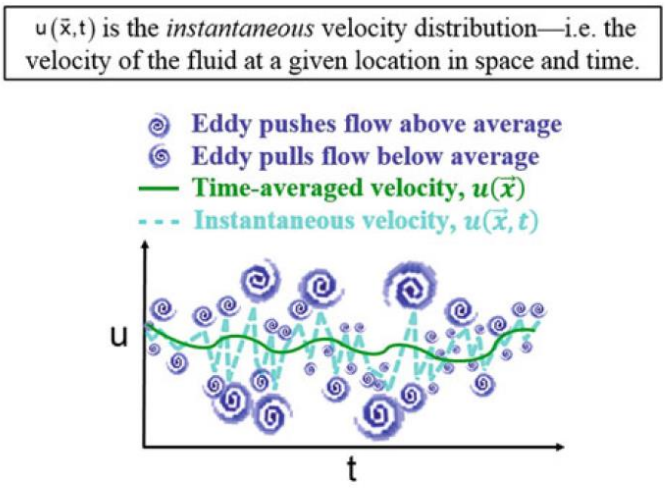

$u(\bar{x},t)$ is the *instantaneous* velocity distribution—i.e. the velocity of the fluid at a given location in space and time.

Figure 2.4. The relationship between eddies, instantaneous velocity distribution, and the time-averaged distribution (taken from Rodriquez (2019)).

With the Reynolds decomposition some terms appear when the time is average due to the interactions between various turbulent fluctuations. These extra terms are modelled with RANS turbulence models, that are usually classified on the basis of the number of additional transport equations that need to be solved. There are zero-equation models, one-equation models, two equation models, and seven equation models.

In this study, the RANS-turbulence models employed belong to two-equation model category. Many studies have considered and compared the advantages of one model in comparison with the other, four turbulence models will be address in this section: the standard *k*-epsilon (*k*-*ε*), the Realizable *k*-*ε*, the Renormalization group *k*-*ε* (RNG), and the *k*-omega (*k*-*ω*).

- **The standard *k*-epsilon (*k*-*ε*) turbulence model**

The standard *k*–*ε* model (Launder and Spalding, 1973) has two model equations, one for the turbulent kinetic energy *k* and one for turbulent dissipation rate *ε*. The standard *k*-*ε* uses the following transport equations (Ben Ramoul *et al.*, 2018):

Turbulent kinetic energy (*k*) equation:

Equation 9
$$\frac{\partial}{\partial t}(\rho k)+\frac{\partial}{\partial x_i}(\rho k u_i)=\frac{\partial}{\partial x_j}\left[\left(\mu+\frac{\mu_t}{\sigma_k}\right)\frac{\partial k}{\partial x_j}\right]+G_k+G_b-\rho\varepsilon-Y_M+S_k$$

Turbulent dissipation rate (ε) equation:

Equation 10
$$\frac{\partial}{\partial t}(\rho\varepsilon)+\frac{\partial}{\partial x_i}(\rho\varepsilon u_i)=\frac{\partial}{\partial x_j}\left[\left(\mu+\frac{\mu_t}{\sigma_\varepsilon}\right)\frac{\partial \varepsilon}{\partial x_j}\right]+C_{1\varepsilon}\frac{\varepsilon}{k}(G_k+C_{3\varepsilon}G_b)$$
$$-C_{2\varepsilon}\rho\frac{\varepsilon^2}{k}+S_\varepsilon$$

The typical values of the closure coefficients can be found in Versteeg and Malalasekera (2007).

- **The realizable *k*-epsilon (*k*-*ε*) turbulence model**

The realizable *k*-*ε* turbulence model contains a new formulation for the turbulent viscosity and a new transport equation for the dissipation rate *ε* that is derived from an exact solution for the transport of the mean-square vorticity fluctuation (Shih *et al.*, 1995). The turbulent dissipation rate equation is written as:

Equation 11
$$\frac{\partial}{\partial t}(\rho\varepsilon)+\frac{\partial}{\partial x_i}(\rho\varepsilon u_i)=\frac{\partial}{\partial x_j}\left[\left(\mu+\frac{\mu_t}{\sigma_\varepsilon}\right)\frac{\partial \varepsilon}{\partial x_j}\right]+\rho C_1 S_\varepsilon-C_2\rho\frac{\varepsilon^2}{k+\sqrt{\nu\varepsilon}}$$
$$+C_{1\varepsilon}\frac{\varepsilon}{k}C_{3\varepsilon}G_b+S_\varepsilon$$

The typical values of the closure coefficients can be found in Ben Ramoul *et al.* (2018).

- **The Re-Normalization Group *k*-epsilon (*k*-*ε*) turbulence model**

The Re-Normalization Group (RNG) *k*-*ε* turbulence model (Yakhot and Orszag, 1986) employs a technique called renormalization group theory to derive the instantaneous Navier-Stokes equations. Consequently, it represents some differences with the traditional method by adding a term in the turbulent dissipation rate equation, also provides analytical formula for turbulent Prandtl numbers, while the standard *k*–*ε* model uses constant values.

Equation 12
$$\frac{\partial}{\partial t}(\rho\varepsilon)+\frac{\partial}{\partial x_i}(\rho\varepsilon u_i)=\frac{\partial}{\partial x_j}\left[\alpha_\varepsilon\mu_{eff}\frac{\partial \varepsilon}{\partial x_j}\right]+C_{1\varepsilon}\frac{\varepsilon}{k}(G_k+C_{3\varepsilon}G_b)$$
$$-C_{2\varepsilon}\rho\frac{\varepsilon^2}{k}-R_\varepsilon+S_\varepsilon$$

In addition, the RNG theory uses a scale elimination procedure that defines the effective viscosity. The typical values of the closure coefficients can be found in Ben Ramoul *et al.* (2018).

- **The Wilcox k-omega (*k*- *ω*) turbulence model**

The *k*-*ω* turbulence model is also a two-equation turbulence model; instead of calculating the turbulent dissipation rate *ε*, the specific rate of dissipation *ω* is calculated (Wilcox, 2008).

Turbulent kinetic energy (k) equation:

Equation 13
$$\frac{\partial}{\partial t}(\rho k)+\frac{\partial}{\partial x_j}\left(\rho u_j k\right)=\rho\tau_{ij}\frac{\partial u_i}{\partial x_j}-\beta^*\rho k\omega+\frac{\partial}{\partial x_j}\left[\left(\mu+\sigma^*\frac{\rho k}{\omega}\right)\frac{\partial k}{\partial x_j}\right]$$

The specific rate of dissipation (ω) equation:

Equation 14
$$\frac{\partial}{\partial t}(\rho\omega)+\frac{\partial}{\partial x_j}\left(\rho u_j\omega\right)=\alpha\frac{\omega}{k}\rho\tau_{ij}\frac{\partial u_i}{\partial x_j}-\beta\rho\omega^2+\sigma_d\frac{\rho}{\omega}\frac{\partial k}{\partial x_j}\frac{\partial\omega}{\partial x_j}+\frac{\partial}{\partial x_j}\left[\left(\mu+\sigma\frac{\rho k}{\omega}\right)\frac{\partial\omega}{\partial x_j}\right]$$

The typical values of closure coefficients can be found in Wilcox (2008).

2.4 Urban ventilation

The air pollution levels can be reduced in urban areas if the natural outdoor ventilation is harnessed. The term ventilation is defined as the process of supplying air to or removing air from a space for the purpose of controlling air contaminant levels, humidity, or temperature within the space (ASHRAE, 2007). This definition is mainly referring to indoor environments (Figure 2.5), but it can be ample for urban areas (Figure 2.6). The idea is that cool sea or rural breeze intentionally induced into the polluted urban area, through proper urban planning, could reduce air pollution inside urban environments in a natural way.

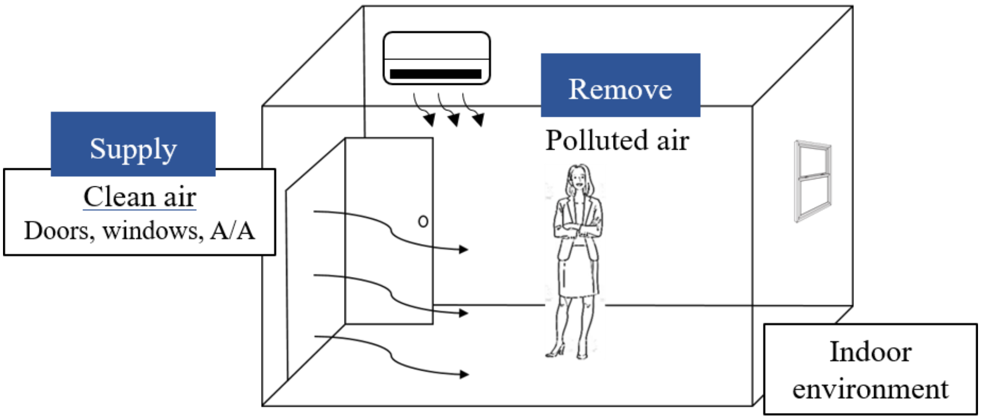

Figure 2.5. Representation of ventilation for indoor environments.

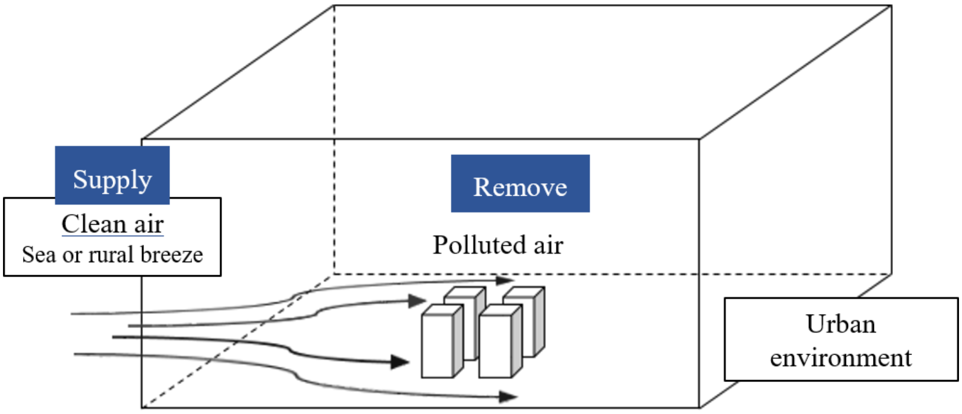

Figure 2.6. Representation of ventilation for urban environments.

In the past, authors have extended the used of indoor ventilation concepts for outdoor applications (Bady *et al.*, 2008; Peng *et al.*, 2020) to better evaluate ventilation performance. Some recent studies have relied in the use of ventilation efficiency indices to describe the characteristics of the urban environment such as the air delay (Antoniou *et al.*, 2017), net escape velocity (Hang *et al.*, 2015; Peng *et al.*, 2019; You *et al.*, 2017), purging flow rate (Bady *et al.*, 2008; Hang *et al.*, 2013; Lin *et al.*, 2014; Mei *et al.*, 2017; Peng *et al.*, 2019), air exchange rate (Hang and Li, 2011; Lin *et al.*, 2014; Mei *et al.*, 2019; Mei *et al.*, 2017; Nazarian and Kleissl, 2016), and age of air (Antoniou *et al.*, 2017; Buccolieri *et al.*, 2010; Gonzalez-Olivardia *et al.*, 2017; Gonzalez-Olivardia *et al.*, 2019; Hang and Li, 2011; Hang *et al.*, 2013; F. Liu *et al.*, 2017; Peng *et al.*, 2019; H. Qin *et al.*, 2020; Ramponi *et al.*, 2015).

Local mean age of air

The local age of air ($\bar{\tau}_p$) is defined as the time taken by fresh air to replace old air after it enters to a given zone. The term was introduced for first time by Etheridge and Sandberg (1996) for practical applications. Equation 15 represents the local age of air for a homogenous emission:

Equation 15
$$\bar{\tau}_p = \frac{c}{\dot{m}}$$

The local age of air indicates that the younger the air, the better is its dilution capability of that specific area, so if the spatial distribution of the local mean age of air is predicted, the spatial variation of ventilation effectiveness in an environment can be known.

Purging flow rate

The purging flow rate (U_p) is the effective airflow rate required to remove or purge pollutants from a domain (Bady *et al.*, 2008). In other words, the purging flow rate can be considered as the net rate by which the pollutants are flushed out of the domain (Equation 16)(Etheridge and Sandberg, 1996).

Equation 16
$$U_p = \frac{\dot{m}_p}{c_p}$$

Low purging flow rate reflects the presence of recirculation, meaning higher concentrations.

Air Exchange Efficiency

The air exchange efficiency (ε_a) (Equation 17) denotes the efficiency in providing rural air into the urban canopy (Etheridge and Sandberg, 1996).

Equation 17
$$\varepsilon_a = \frac{\tau_n}{\tau_{exc}} \times 100 = \frac{\tau_n}{2\langle\bar{\tau}\rangle} \times 100$$

Depending on the efficiency of the system, the air exchange efficiency can be classified as indicated in Table 1.

Table 1. Air exchange efficiency for different flow conditions

Flow pattern	**Air-exchange efficiency $\boldsymbol{\varepsilon_a}$**
Ideal piston-flow	100 %
Ventilation by displacement	$50 \leq \varepsilon_a <100$ %
Complete and instantaneous mixing	$\varepsilon_a = 50$ %
Short-circuiting	$\varepsilon_a <50$ %

Modified from Etheridge and Sandberg (1996)

2.5 Chemical reaction models

Air pollution in urban areas need to be improved to protect pedestrians, cyclists and drivers from exposure to contaminants such as particulate matter (PM), volatile organic compounds (VOCs), carbon monoxide (CO), nitrogen oxides (NO_x), and sulfur dioxide (SO_2) that are primarily emitted from motor vehicles. Among these contaminants, NO_x and VOCs represent the most significant concern for air pollution in street canyons because they are released at very short distances from the receptors and under the presence of sunlight, fast reactions occur between them leading to the formation of particulate matter and tropospheric ozone (O_3).

A new urban and regional photochemistry model called Carbon Bond Mechanism IV (CBM-IV) was derived to predict the formation of ozone and other oxidants that result from complex chemical interaction of oxides of nitrogen (NO_x) and organic species in the presence of solar radiation (Gery *et al.*, 1989) (Equation 18):

Equation 18
$$\frac{\partial c}{\partial t} + \nabla \cdot (uc) = D\nabla^2 c + R + S_{chem}$$

Equation 18 is similar to Equation 7, but adding the last term at right hand that represents the net chemical production rate of the species calculated by the CBM-IV model.

CHAPTER 3. STUDY OF THE RELATIONSHIP OF THE VENTILATION EFFICIENCY AND URBAN ENVIRONMENT

3.1 Introduction

This chapter addresses the use of ventilation efficiency indices to describe the ventilation performance inside urban areas. Appropriate ventilation efficiency indices are able to describe the capability of the air from outside the urban areas to refresh the city environment and improve air quality levels. Nevertheless, difficulties arise to establish the suitability of the ventilation efficiency indices to capture the airflow characteristics and relate them to specific urban environments.

In this chapter, the local age of air, the purging flow rate, and the air exchange efficiency are employed to evaluate the ventilation efficiency of various urban parameters in an ideal urban environment and describe the behavior of the wind within a real urban environment.

3.2 Methodology

Two computational domains were evaluated to assess the ventilation efficiency indices: a computational domain representing an ideal urban environment and a computational domain representing an actual urban environment.

3.2.1 Ideal urban environment

A systematic analysis of an ideal urban environment is conducted to clarify the influence of urban parameters on ventilation efficiency. The cases have the same building packing density (**Error! Reference source not found.**), building height but different building width and street width. The three ideal urban environments studied were called Case A, Case B, and Case C (Figure 3.1).

Table 2. Urban parameters for the ideal urban environment

	Case A	**Case B**	**Case C**
λ_p	0.5625		
Building height (m)	30		
Building width (m)	72	48	36
Street width (m)	24	16	12

The computational domains were drawn in FlowDesigner, a commercial CFD software developed by Advanced Knowledge Laboratory, Inc (AKL, 2018). The computational domain was 984 m in x-coordinate, 984 m in y-coordinate, and 330 m in z-coordinate for all the cases. For the ideal urban environment, the size of the city domain was x: 384 m and y: 384 m, and the size of the analysis domain was x: 192 m and y: 192 m.

The horizontal mesh in the city domain was 2.0 m in x-direction and y-direction, and then the grid resolution has an increase of about 10%. In z-direction, the grid resolution measured 1 m up to 13 m; then, it was increased at about 10% rate until 330 m. Approximately 3.3 million (250 × 250 × 53) hexahedral meshes were generated.

3.2.2 Actual urban environment

Two cities with different building packing density and building height —Hiranomachi (34.69N, 135.50E) and Maishima (34.66N, 135.40E)— located in Osaka City, Osaka Prefecture Japan were selected. **Error! Reference source not found.**From Figure 3.2 to Figure 3.5, the Google Earth view and the computational domain in FlowDesigner is shown for Hiranomachi and Maishima, respectably. The information about length, width, and the number of floors of every building was obtained from the survey on land use conducted by Osaka City in 2005.

The size of the calculation domain for both cases was 1000 m in x-coordinate, 1000 m in y-coordinate, and 180 m in z-coordinate. For both locations, the city domain was defined as x:355 m and y: 365 m and the analysis domain were x: 177 m and y: 183 m (Figure 3.6).

The grid resolution in the city domain was 2.5 m in x- and y-direction; outside this area, the grid resolution had an increase of about 10%. In z-direction, the grid resolution was 0.5 m to 20 m; from 20 m to 180 m, an increase of about 10% was used. For this computational domain, 3.4 million (195 ×198 × 89) hexahedral cells were generated (Figure 3.6).

Table 3. Urban parameters for the real urban environment

	Hiranomachi	**Maishima**
λ_p	0.66	0.37
Building height (m)	4-57	4-20

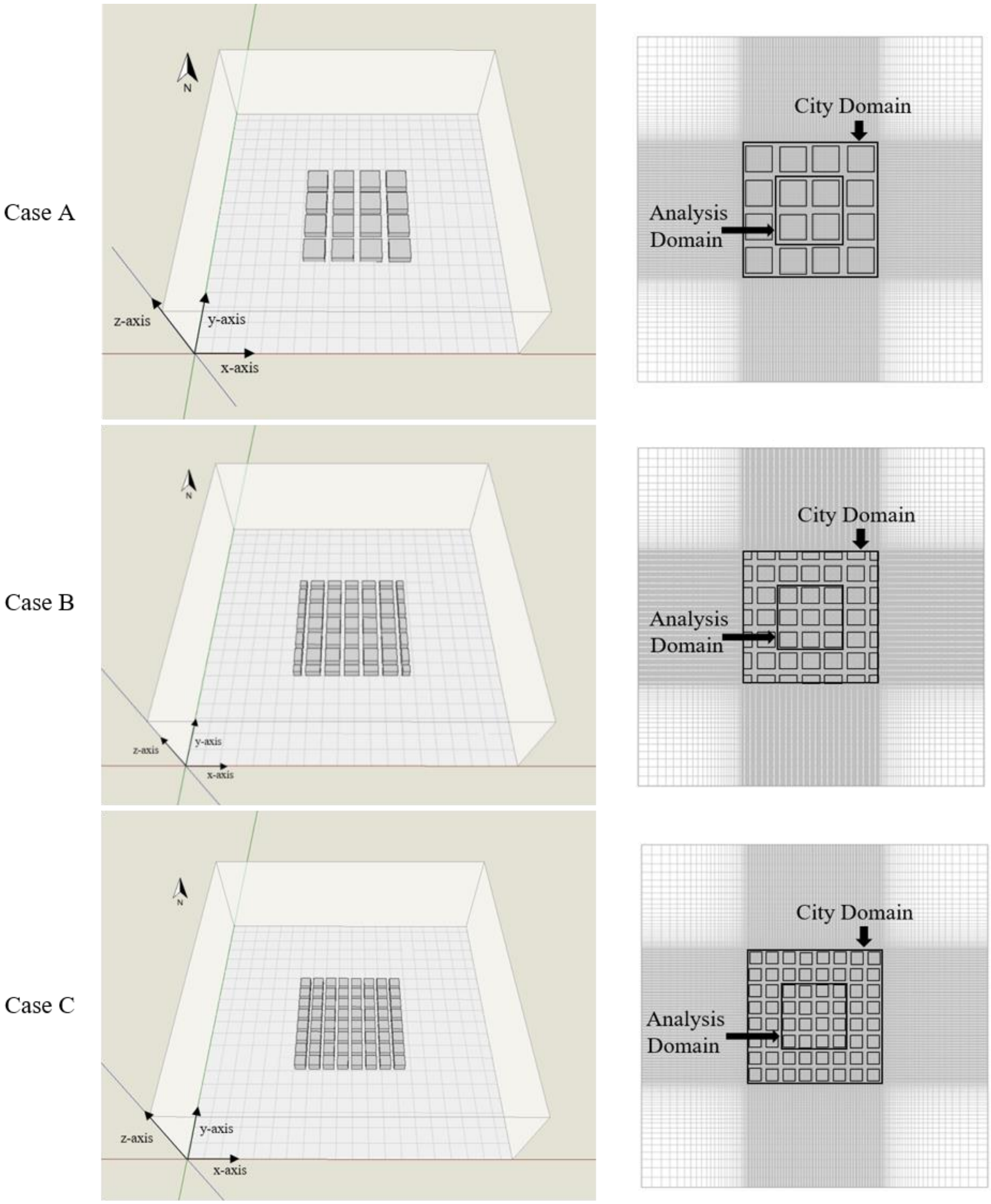

(a) (b)

Figure 3.1. (a) Computational domain in FlowDesigner for Case A, Case B, and Case C (b) City domain and analysis domain mesh view for Case A, Case B, and Case C.

Figure 3.2 Google Earth view Hiranomachi, Osaka Japan (34.69N, 135.50E)

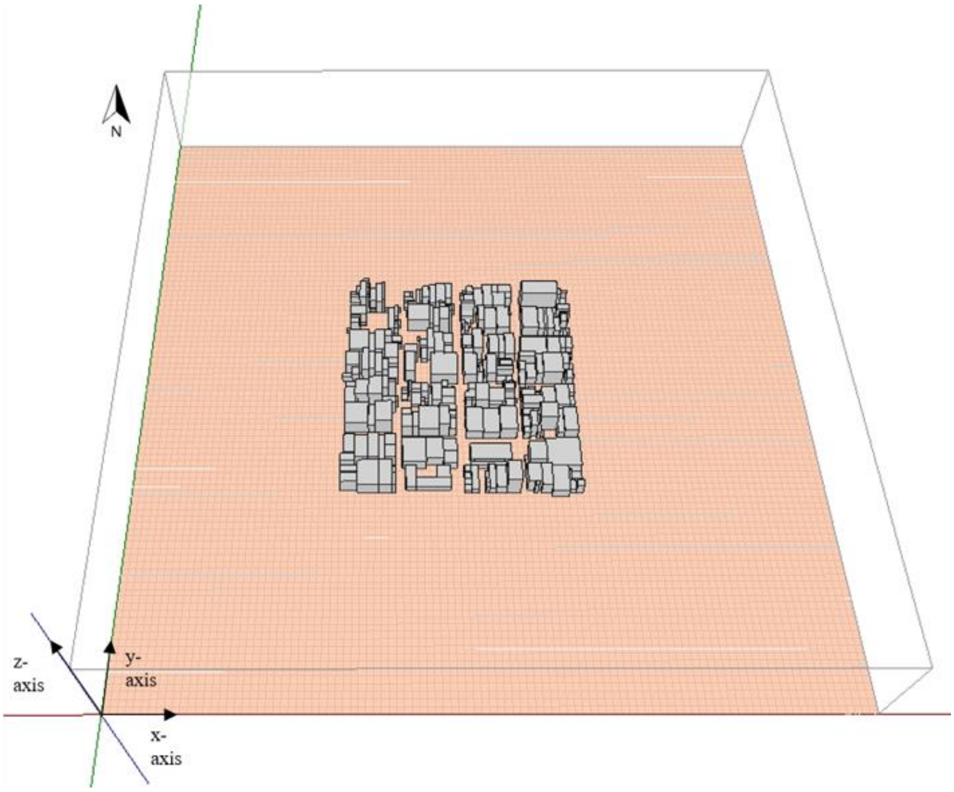

Figure 3.3. Hiranomachi area computational domain.

Figure 3.4 Google Earth view Maishima, Osaka Japan (34.66N, 135.40E)

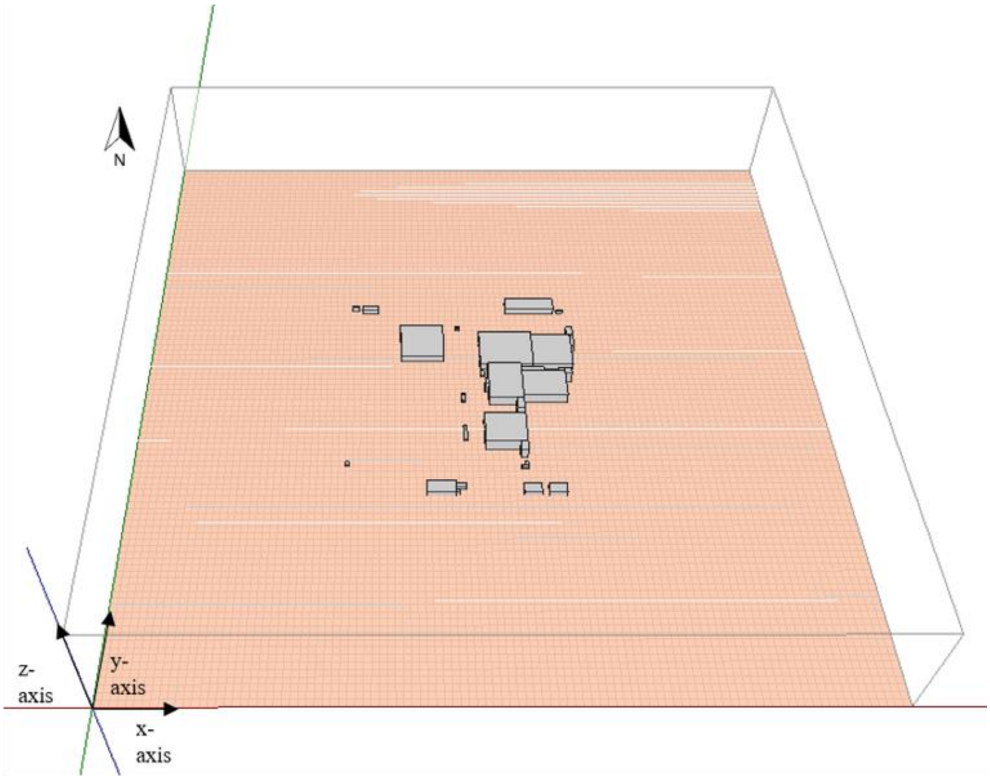

Figure 3.5. Maishima area computational domain[1]

---

[1] The north of the computational domain is rotated 6 degrees counterclockwise in comparison to the Earth North

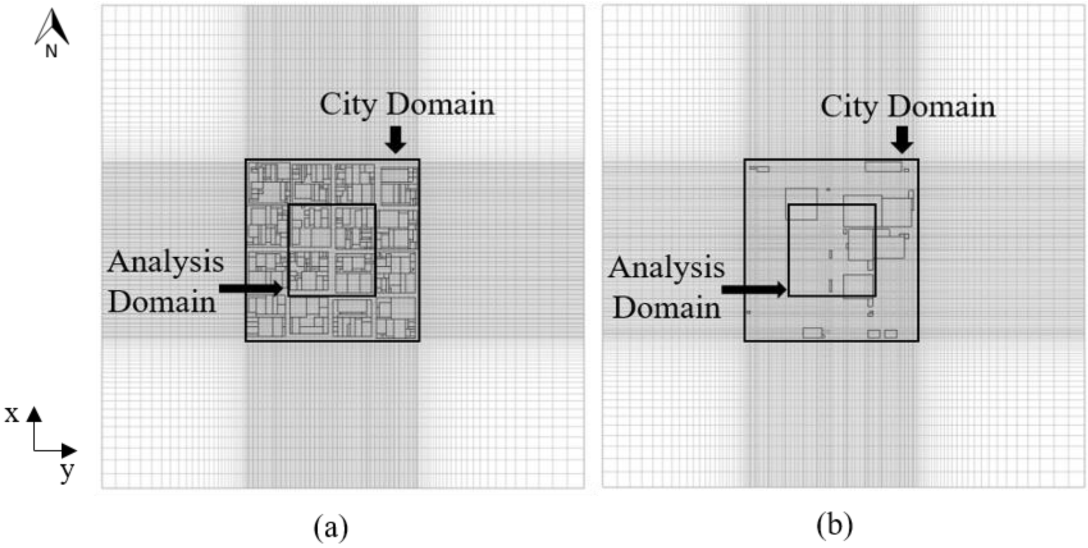

Figure 3.6. City domain and analysis domain mesh view (a) Hiranomachi (b) Maishima.

3.2.3 Boundary conditions

The two urban computational domains considered —actual and ideal (Figure 3.7) — have the same boundaries conditions. The power law boundary condition was used to define the inlet wind velocity U_{in} at height Z(m) and given in Equation 19.

Equation 19
$$U_{in} = U_{ref}\left(\frac{Z}{Z_{ref}}\right)^{n}$$

In this study, 3.0 m/s from the west, 10 m and 0.25 were used as U_{ref}, Z_{ref} and n, respectively. For all the solid surfaces the no-slip boundary condition was used, for the top, north and south boundaries of the calculation domain, symmetry boundary condition and for the east (outlet) boundary, the zero gradient boundary condition was employed. For pressure, a zero gradient boundary condition for the inlet and all solid surfaces, constant value for outlet, and symmetry boundary condition for the top, south and north was indicated.

For this study, the standard k-ε turbulence model was employed. The inlet boundary conditions of the turbulent kinetic energy k, and the dissipation rate ε were decided according to Equation 20 and Equation 21 (OpenCFD, 2020), where I is 0.15 and l is 1.0 m.

Equation 20
$$k = \frac{3}{2}\left(I \cdot \left|U_{ref}\right|\right)^{2}$$

Equation 21
$$\varepsilon = C_{\mu}^{0.75} \cdot \frac{k^{1.5}}{l}$$

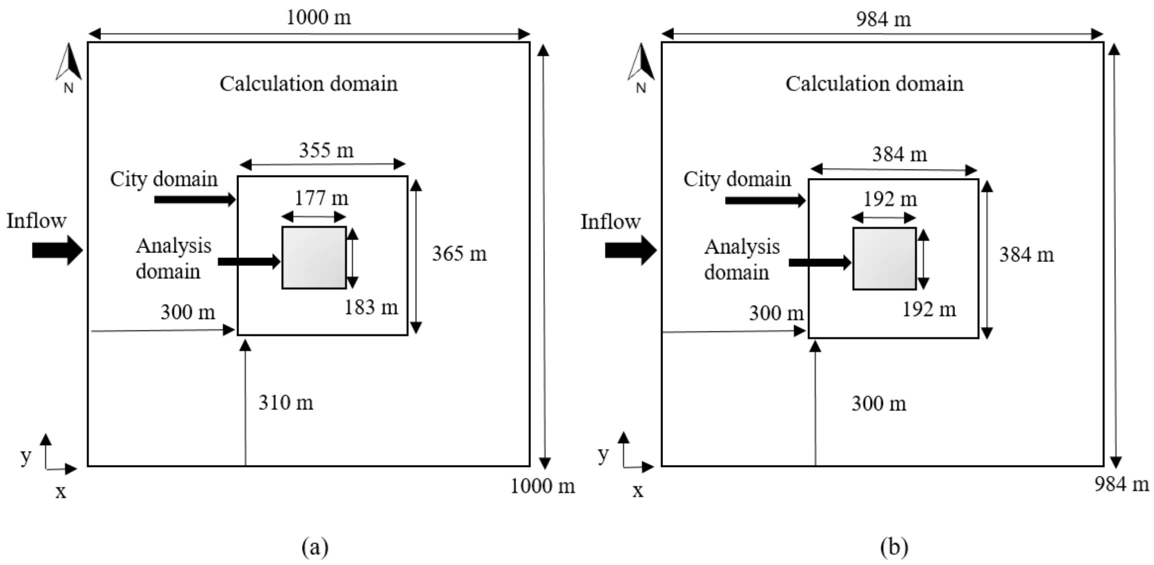

Figure 3.7. Size of the calculation domain, city domain, analysis domain and direction of the inflow wind velocity: (a) actual urban environment, (b) ideal urban environment.

3.2.4 Homogenous emission setting

As part of the scalar transport equation (Equation 7) and the ventilation efficiency indices formulation (Equation 15, Equation 16, and Equation 17), a source of homogenous emission of tracer gas 1 mg/m^3/s in the area of the analysis domain (Figure 3.7) from z: 0 m to z: 4 m was set. The concentration boundary conditions were zero for the inlet, gradient for all solid surfaces and outlet, symmetry for top, north and south.

3.2.5 Normalized velocity

The results of the wind velocity U_n (-) were normalized as indicated in Equation 22.

Equation 22
$$U_n = \frac{U}{U_{ref}}$$

3.3 Results and discussion

3.3.1 Ideal urban environment

Figure 3.8 shows the wind flow results for Case A, Case B, and Case C top view at z: 1 m and lateral view y: 492.5 m. The inflow wind from the west is predominant in the buildings array. However, air is observed to enter laterally and reach the analysis domain. Since, in this study, all the cases have the same building packing density, the variation of the street widths can be understood better.

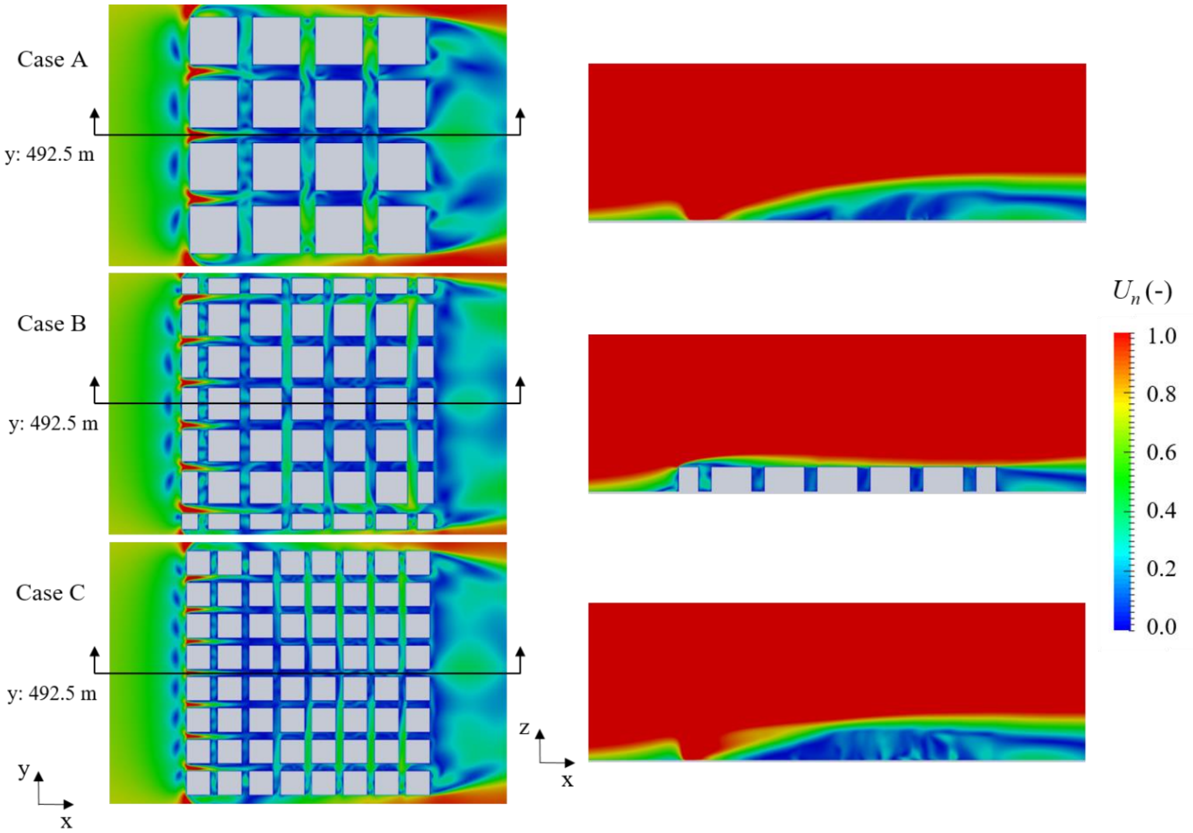

(a) (b)

Figure 3.8. City domain wind profile U_n (-) at z:1 m for Case A, Case B, and Case C (a) top view at z: 1 m (b) Lateral view at y: 492.5 m.

Figure 3.9 shows the spatially-averaged concentration field in the city domain at steady-state for Case A, Case B, and Case C. The spatially-averaged concentration is higher in the city domain as the width of the streets decrease. High levels of contaminant are mainly retained on the leeward of the buildings. Although, the concentration decreases mainly streamwise, and it is influenced by the wind coming from the lateral side (north and south boundaries) of the arrays.

About the influence of building packing density, Buccolieri and Sandberg (2008) mentioned that the pollutant spread decreases with the increasing of packing density, without mentioning further urban characteristics. We could add that for scenarios with a same building packing density of 0.56, the dispersion of contaminants is influenced by the spanwise wind flow.

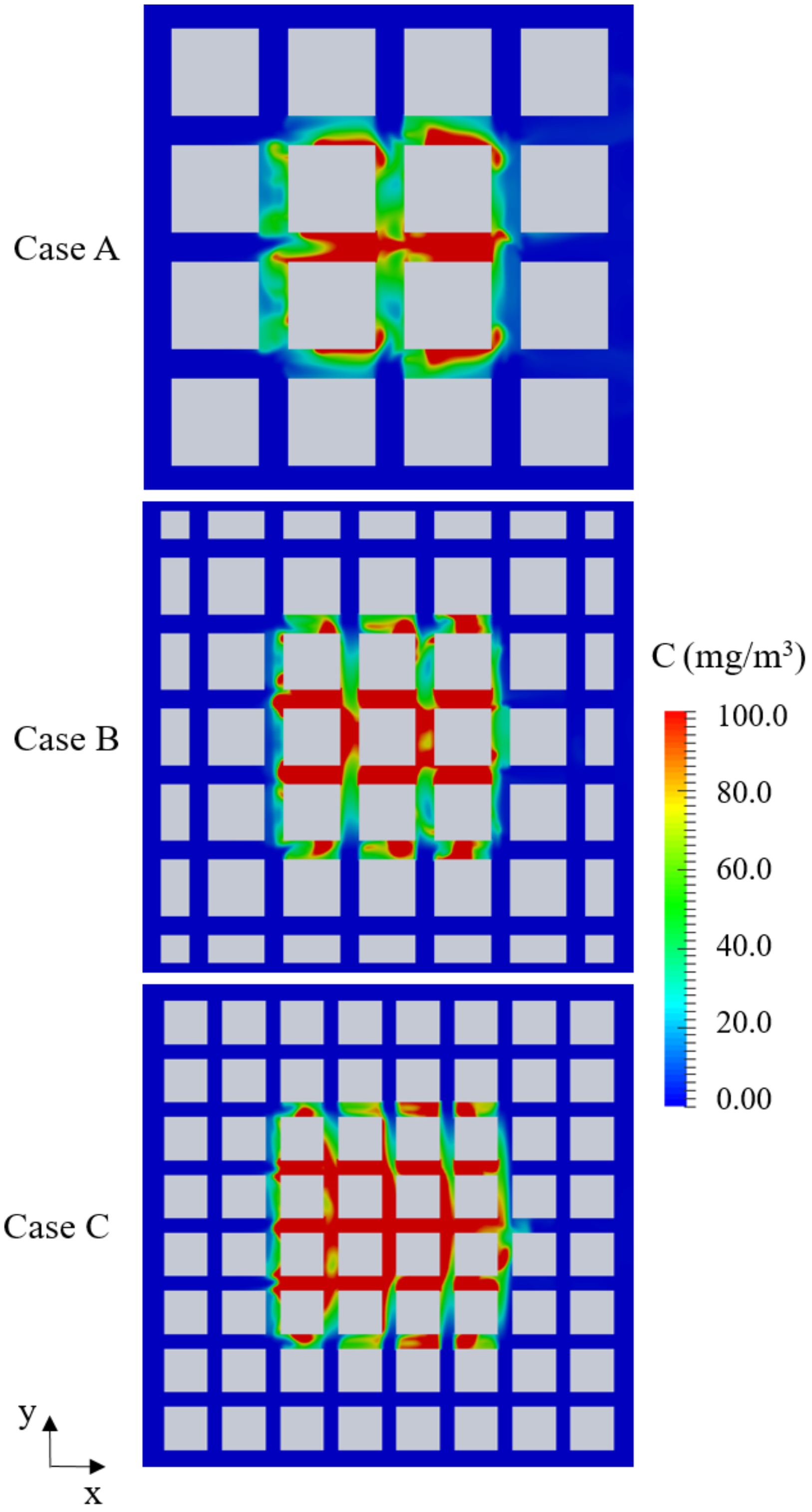

Figure 3.9. City domain view of the spatially-averaged concentration field at steady state for the ideal urban environment: Case A, Case B, and Case C.

3.3.2 Actual urban environment

Figure 3.10 shows the wind flow results for Hiranomachi and Maishima top view at z: 1 m and lateral view y: 492.5 m. In Hiranomachi, low mean flows are seen through the entire city domain, especially downstream. In secondary streets — streets perpendicular to main inflow velocity— the normalized velocity U_n values range from 0.0 to 0.4.

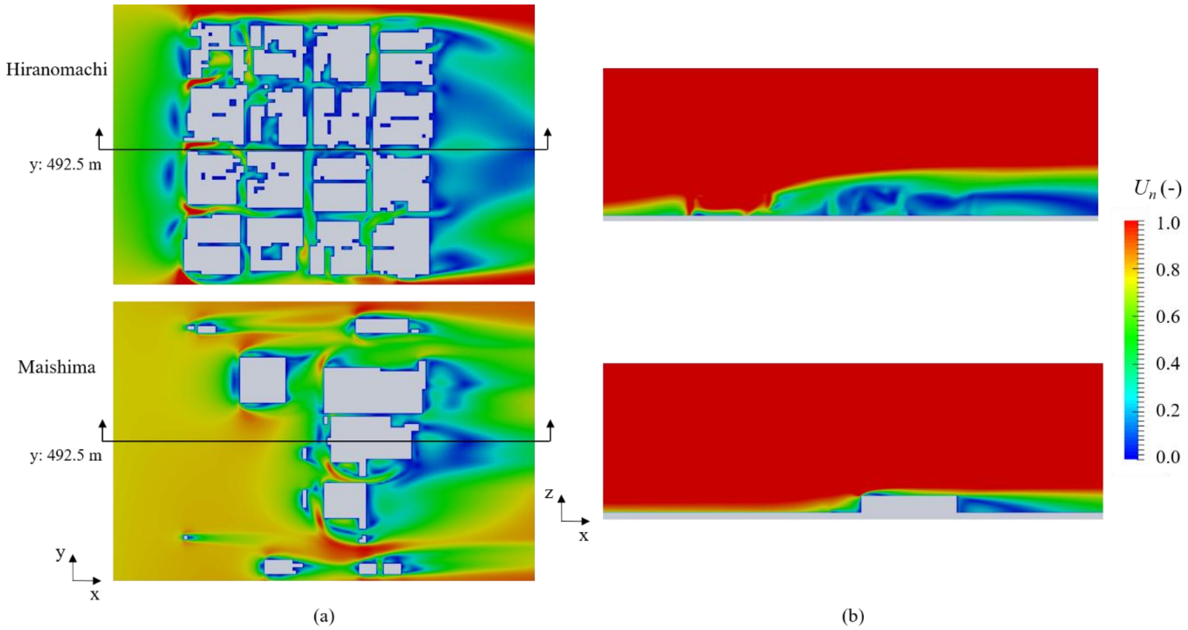

Figure 3.10. City domain wind profile U_n (-) at z:1 m for Hiranomachi and Maishima (a) top view at z: 1 m (b) Lateral view at y: 492.5 m

For Maishima, we can see that the wind flow velocities are almost two times higher when we compare with the Hiranomachi analysis domain. The lateral view shows that the boundary layer in Hiranomachi is extended further than Maishima. This remarkable difference between Hiranomachi and Maishima results from the morphology because the height of buildings ranges from 4 m to 52 m in Hiranomachi and from 4 m to 20 m in Maishima.

Figure 3.11 shows the spatially-average concentration distribution once steady state is reached, in Hiranomachi and Maishima analysis domain. The results indicated that a large portion tracer gas is mainly located in the leeward side of the buildings. Moreover, some of the tracer gas are kept in enclosed areas at Hiranomachi, the main reason may be the low wind speed and the complicated building shapes, as we can confirm from Figure 3.10. So, these results show that complex geometry causes lower ventilation efficiency by lower wind speed and many drifts.

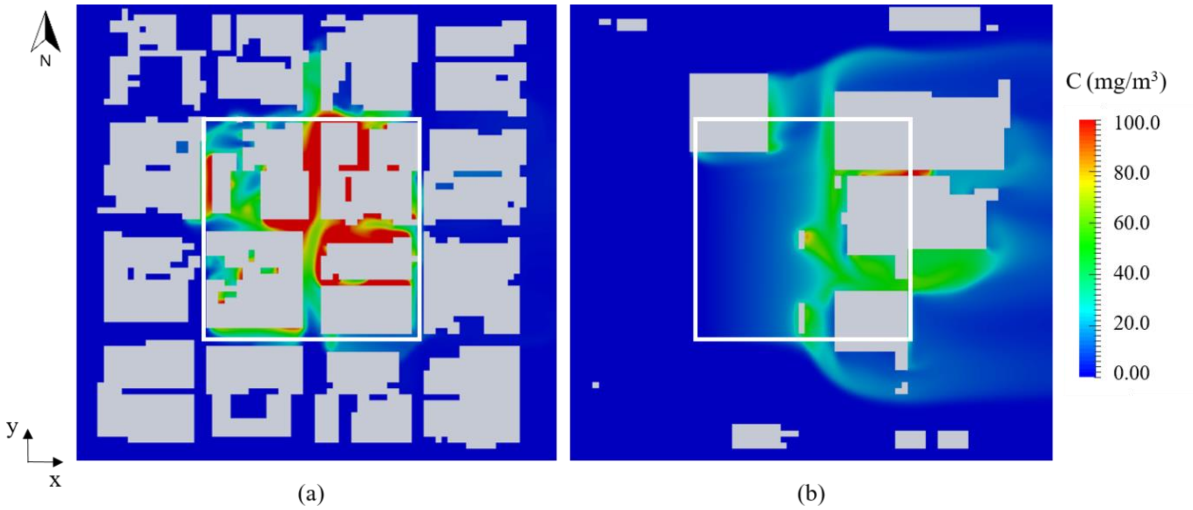

(a)

(b)

Figure 3.11. City domain view of the spatially-averaged concentration field at steady state for the actual urban environment (a) Hiranomachi (b) Maishima.

3.3.3 Ventilation efficiency indices and urban parameters

Local age of air

As mentioned before, the local age of air is the time required by clean air to reach a specific area in the city. The local age of air analysis is based on the idea that the air outside the analysis domain is clean air, meaning that the concentration was equal to zero.

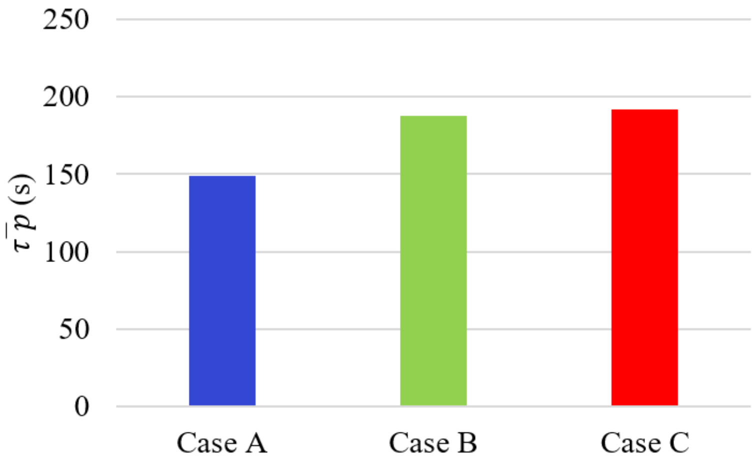

Figure 3.12. Local age of air for Case A, Case B, and Case C.

For the ideal urban environment —Case A, Case B, and Case C (Figure 3.12)— the relationship between the street width is directly related with the local age of air, so when the street is narrower the time required to refresh the same space takes 192 seconds as it is in Case C. When the streets widener, the local age of air decreases to 188 seconds for Case B and 149 seconds for Case A.

The results for the local age of air in Figure 3.13 show that the time required for Hiranomachi (128 seconds) is more than four times the required to clean the air in Maishima (30 seconds). The results show the influence of the number of building and building height on the capacity of the wind to refresh the urban environment.

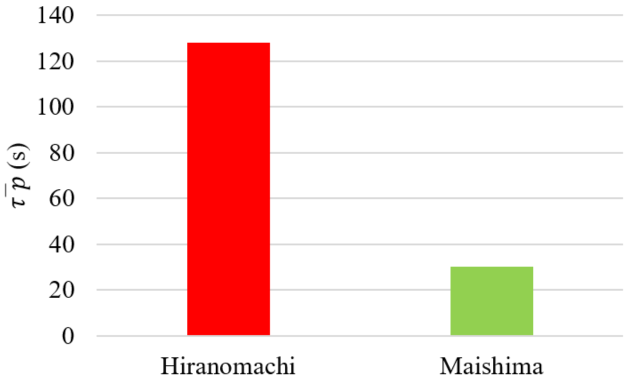

Figure 3.13. Local age of air for Hiranomachi and Maishima.

Purging flow rate

The purging flow rate represents the ability at which the wind can remove pollutants from the domain. For the ideal urban environment (Figure 3.14), the purging flow rate for Case A is 3252 m^3/s, Case B is 2577 m^3/s, and Case C 2521 m^3/s.

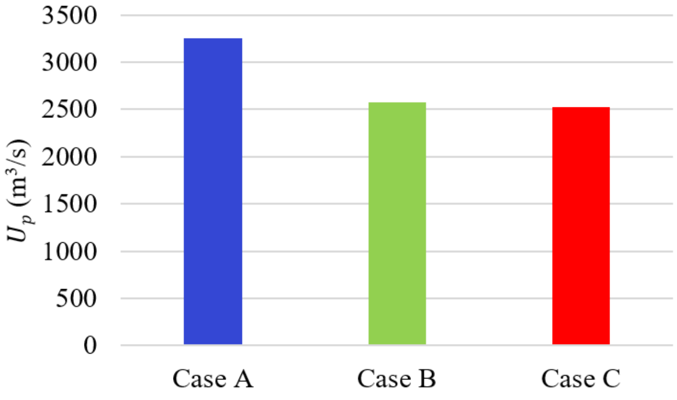

Figure 3.14. Purging flow rate for Case A, Case B, and Case C.

Figure 3.15 shows that contaminants are removed or purge at a higher rate from Maishima analysis domain 32377 m^3/s because the concentration of tracer gas is lower than 5220 m^3/s in Hiranomachi, where a higher concentration is seen. The pollutants are flush away from the domain at a higher rate when the street width is larger and the number of buildings is smaller, the purging flow rate indicates the presence of recirculation.

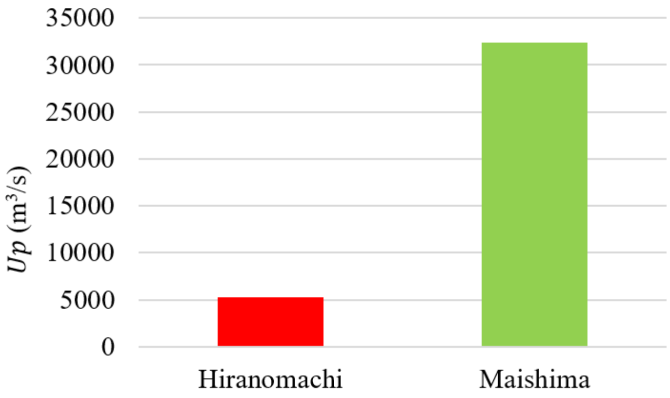

Figure 3.15. Purging flow rate for Hiranomachi and Maishima.

Air Exchange Efficiency

The air exchange efficiency is an indicator of how efficiently the air is replaced from an area by new air.

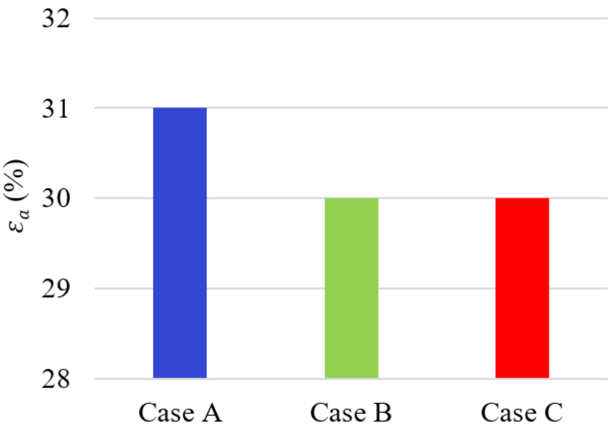

Figure 3.16. Air exchange for ideal urban environment.

The air exchange efficiency for the ideal urban environment (Figure 3.16) is 31 % for Case A, 30 % for Case B, and 30 % for Case C. The actual urban environment air exchange efficiency is 35 % and 77 % for Hiranomachi and Maishima, respectively (Figure 3.17). The air exchange efficiency results indicate that all the cases studied (actual and ideal urban environment, excluding the Maishima) area have a low air exchange efficiency, which is characteristic of short-circuiting flow patterns (Table 1).

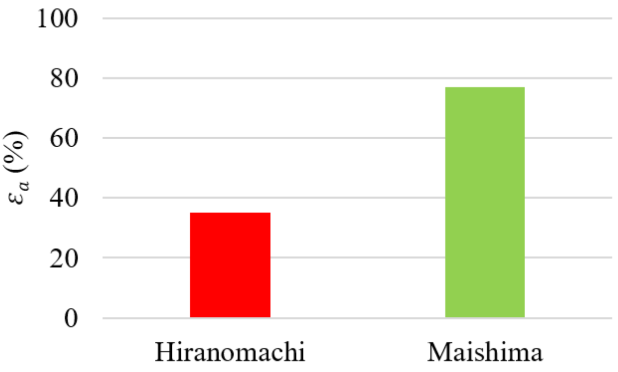

Figure 3.17. Air exchange for actual urban environment

The short-circuiting flow pattern indicated that the supplied air resided a short time without passing the occupied space. In practice for indoor applications, short-circuiting may occur when both the supply and extract points are located above the occupied space (Etheridge and Sandberg, 1996). As mentioned before, because of the wind was entering laterally, and the air exchange efficiency is not quite suitable to consider the vertical wind flow and mass rate interchange at the top of the analysis domain area where the homogenous emission was set (z: 4 m), low efficiencies are observed.

The results of the local age of air for the ideal urban environment —Case A, Case B, and Case C— show that there is a 26 % reduction of the time require to refresh the urban environment if we compare the configuration of Case A and Case B. However, Case B and Case C only have a 2% reduction. If we compared the configuration in Case A and Case C, 28.8 % less time is required to refresh the urban environment. Similarly, for the purging flow rate 26% more volume of air is required in Case B in comparison with Case A, and Case C requires 2 % more volume of air than Case B. Case C requires 29 % more volume of air than Case A. The local age of air and the purging low rate have quite the same percentages of increments between the three configurations.

Alternatively, the street width of Case A is 50 % bigger than Case B, and Case B is 33 % bigger than case C. Similarly, Case A is 100 % wider than Case C, however there is not a straight forward relationship with the local age of air and purging flow rate.

Some authors may suggest that there is a packing density which the sensitivity of the spread of pollutant diminishes. This could explain the similarity among Case B and Case C.

3.4 Conclusions

The conclusions about the relationship between urban environment parameters and ventilation efficiency indices are mentioned bellow:

- The local age of air, the purging flow rate, and the air exchange efficiency are ventilation efficiency indices that can help describe the different characteristics of urban environments. However, the air exchange efficiency requires further considerations.
- The results indicated that similarly when the spread of contaminants is diminished for certain packing densities, same occurs to street widths.
- This study has helped analyze the urban form parameters such as building packing density, buildings height, street width, building width, and meteorological parameters such as wind direction and wind velocity.
- Ventilation efficiency indices in the outdoor application are of practical importance since they can evaluate the effect of specific geometrical characteristics of urban domains and represent an important tool to assess the ventilation performance in urban areas.

CHAPTER 4. ASSESSMENT OF THE INFLUENCE OF URBAN INTERSECTIONS ON VENTILATION EFFICIENCY

4.1 Introduction

This chapter evaluates the dispersion of pollutants in street intersections and nearby connecting streets using the local age of air to measure ventilation efficiency. The urban environment is represented as idealized building blocks of packing density ($\lambda_p = 0.25$) (Grimmond and Oke, 1998) with a four-way intersection of two perpendicular (90°) streets. In this chapter, the first objective is to qualitatively evaluate the effect of different wind conditions on the flow patterns in street intersections and connecting streets; the second is to quantify pedestrian ventilation efficiency in urban intersections using the local age of air. Lastly is to assess how the wind entering the street intersection contributes to the dispersion of pollutants in the urban environment.

4.2 Methodology

4.2.1 Validation of the CFD simulations

The CFD simulations were validated against wind tunnel experiment data (Nonomura *et al.*, 2003). The test case consisted of simple building blocks of three rows and three columns (3 × 3). The building width (B), street width (W), and building height (H) were each equal to 0.2 m, and the building packing density (λ_p) was 0.25 (H/W = 1) (Figure 4.1).

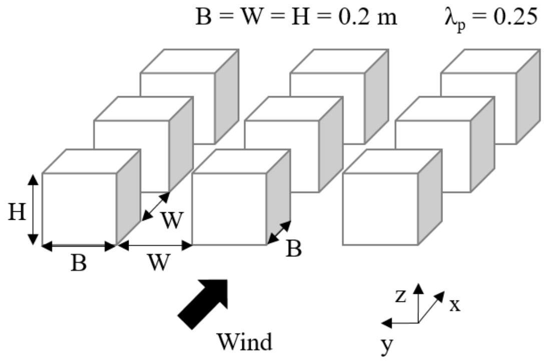

Figure 4.1. Building blocks used in the wind tunnel experiments and CFD simulations ($\lambda p = 0.25$, B = W = H = 0.2 m)

For this chapter, the software OpenFOAM 4.0 (OpenCFD, 2020) was employed to simulate the dispersion of pollutants in urban intersections. The size of the computational domain (Figure 4.2) in stream-wise (x), span-wise (y), and vertical (z) directions was 25B, 15B, and 6B, respectively. For the boundary conditions of velocity at the top and sides, the symmetry boundary condition was set, and for the outlet, the zero normal gradient was indicated. For the ground and building blocks, a no-slip boundary condition was used (Figure 4.2). The inlet boundary condition for the turbulence intensity was defined as 0.15 (Equation 20), and the eddy length scale was 1 (Equation 21). The boundary condition for the wind speed in the inlet was fixed following the wind tunnel experiment shown in Figure 4.4. (see Table A 1 in Appendix A)

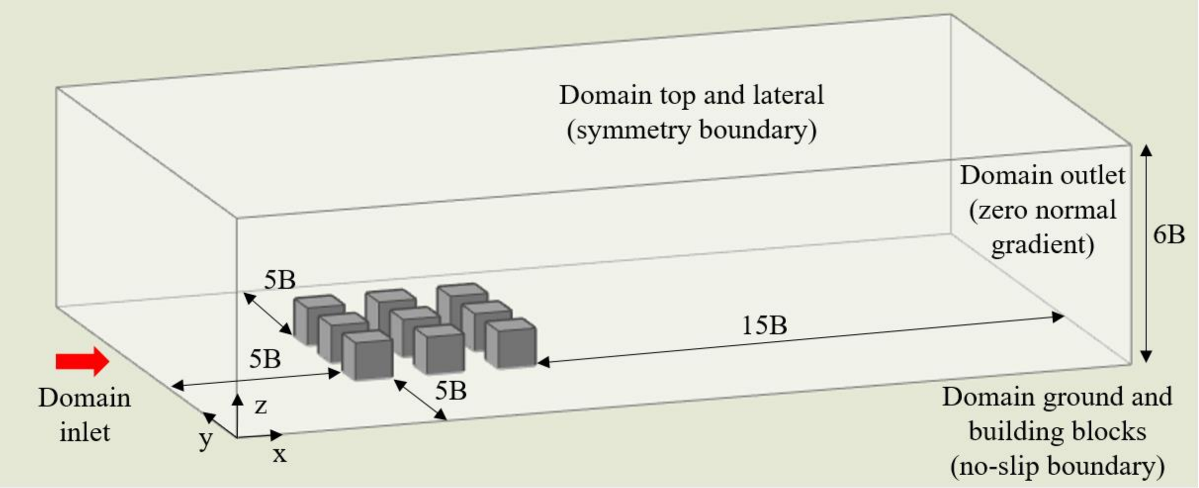

Figure 4.2. Calculation domain size and boundary conditions.

The accuracy of four OpenFOAM-RANS turbulence models was evaluated. The turbulence models were: the standard k-ε (Equation 9 and Equation 10), the Realizable k-ε (Equation 9 and Equation 11), the Renormalization group k-ε (Equation 9 and Equation 12) and the k-ω (Equation 13 and Equation 14).

The results of the wind velocity simulations were normalized by the inflow velocity at z = 0.1B (2.434 m/s) and compared to the results of the wind tunnel experiments in 120 locations (Figure A1). Besides, a grid independency study for three mesh sizes—coarse, medium, and fine—was conducted (Figure 4.3). The wind tunnel experiment results (Table A 2 in Appendix A), the four RANS turbulence models, and the three different grid sizes were statistically evaluated.

Different metrics, such as the fractional bias (FB) (Equation 23), and the fraction of predictions within a factor of two observations (FAC2) (Chang and Hanna, 2004) and the mean of the wind speed, was conducted.

Equation 23
$$FB = \frac{(\overline{C_o} - \overline{C_p})}{0.5\,(\overline{C_o} + \overline{C_p})}$$

Equation 24 $$FAC2 = fraction\ of\ data\ that\ satisfy\ 0.5 \le \frac{C_p}{C_o} \le 2.0$$

	Grid size	**Hexahedral cells**	**Smallest grid size** **x, y, z**
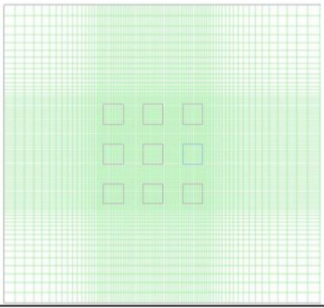	Coarse	272 800	0.10 B, 0.10 B, 0.10 H
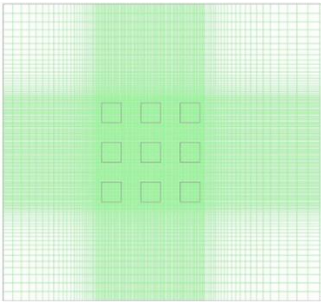	Medium	1 285 172	0.05 B, 0.05 B, 0.05 H
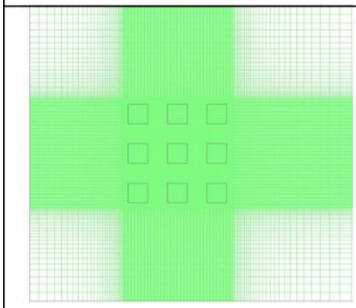	Fine	6 377 280	0.025 B, 0.025 B, 0.025 H

Figure 4.3. Top view of the three grid sizes (coarse, medium, and fine), the number of cells, and size of the smallest grid used in the grid resolution independency study of the CFD calculation domain

Table 4 shows that the fractional bias of the Realizable k-ε turbulence model with a fine grid was the closest to 0 with a value of 0.021, and the FAC2 was the closest to 1 with a value of 0.979. Similarly, the mean of the wind speed for the wind tunnel experiment was 0.657 m/s, and 0.641 m/s for the Realizable *k-ε* with a fine grid. The statistical analysis indicated that the Realizable *k-ε* turbulence model with a fine grid resolution had the best performance in comparison with the wind tunnel experiment. Consequently, the Realizable *k-ε* turbulence model with a fine grid resolution was used for the remainder of this chapter.

Table 4. Flow statistical analysis

	Grid size	FB Perfect model FB = 0	FAC2 Perfect Model FAC2= 1	Mean of the wind speed (m/s)
Wind tunnel experiment	-	-	-	0.657
Standard *k*-*ε*	Coarse	0.274	0.759	0.496
	Medium	0.129	0.879	0.575
	Fine	0.039	0.962	0.629
Realizable *k*-*ε*	Coarse	0.315	0.728	0.476
	Medium	0.122	0.885	0.579
	Fine	0.021	0.979	0.641
RNG *k*-*ε*	Coarse	0.360	0.695	0.455
	Medium	0.247	0.780	0.510
	Fine	0.253	0.775	0.507
k*-*ω	Coarse	0.385	0.677	0.443
	Medium	0.262	0.768	0.503
	Fine	0.296	0.742	0.485

For all of the simulations conducted, the air was modelled as incompressible, isothermal conditions, steady-state, and no external forces. The equation of passive scalar transport was presented in a transient state. The conservation equation of mass and momentum, and the scalar transport equation, were discretized by the finite volume method. The second-order upwind scheme was used as the discretization scheme of the convection terms, and the second-order central difference scheme was used as the discretization scheme of the diffusion terms in the governing equations. The first-order Euler method was utilized as the time discretization scheme for the scalar transport equation. The semi-implicit method for the pressure-linked equations (SIMPLE) algorithm was employed as the pressure–velocity coupling algorithm.

4.2.2 Simulation cases

The dispersion of contaminants in urban intersections was evaluated under three wind speed conditions (Figure 4.4). The reference height for the power-law used to calculate the wind conditions was z: 5H. Three velocities of 3.5 m/s, 5.5 m/s, and 7.5 m/s at z: 5H—labeled low, medium, and high, respectively—were studied.

The urban layouts evaluated under the three wind speed conditions were divided into two groups (Figure 4.5). Figure 4.5 (a) shows the first group, which quantifies the ventilation efficiency in urban intersections. Figure 4.5 (b) shows the second group, which clarifies the relationship between various approaching wind conditions and the distribution of contaminants in street intersections and the connecting streets.

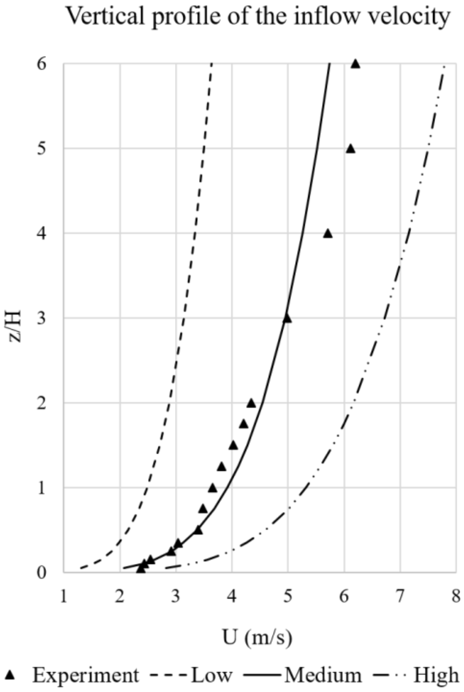

Figure 4.4. Vertical profile of the experiment, and the low, medium, and high inflow velocities, evaluated in this study

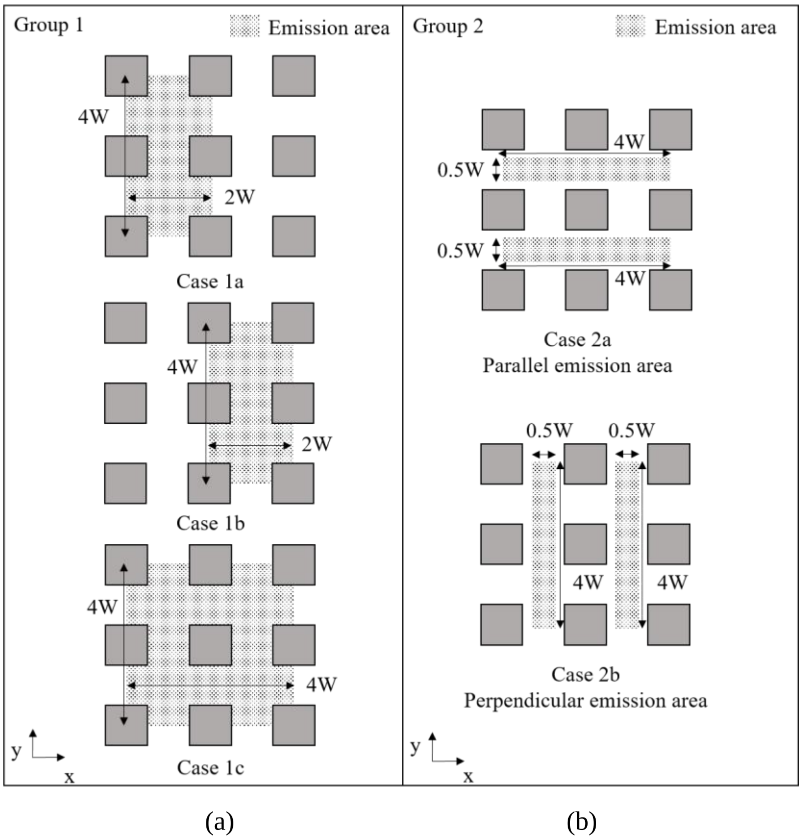

Figure 4.5. Array used in the CFD simulations (a) group 1 (Case 1a, Case 1b, and Case 1c), (b) group 2 (Case 2a, parallel emission area and Case 2b, perpendicular emission area). The areas filled with dotted patterns indicate the emission area for each group.

The concentration was held constant at zero for the inlet. The homogeneous emission was set to 1 mg/m^3/s from the ground to 0.25H in the areas filled with dots indicated in Figure 4.5. The size of the emission area in group 1, Case 1a, and Case 1b was 2W × 4W, and for Case 1c was 4W × 4W; for group 2, the size was 0.5W × 4W for the parallel emission area, and 4W × 0.5W for the perpendicular emission area.

Four urban intersections of two perpendicular (90°) streets were considered (Figure 4.6). The intersections were named clockwise using capital letters (A, B, C, D). The size of each intersection was 2B × 2B.

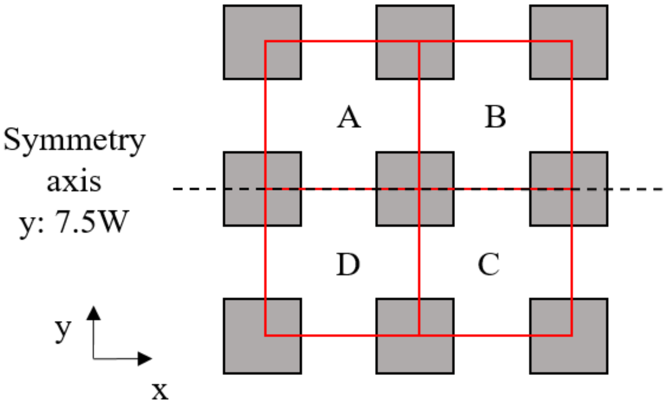

Figure 4.6. Top view of the four urban street intersections (A, B, C, D) evaluated in this chapter and the location of the symmetry axis at y: 7.5W.

4.2.3 Ventilation efficiency index and normalized concentration

In this chapter, the local age of air (Equation 15) was employed to evaluate the ventilation efficiency in urban intersection. The air outside the analysis area is considered clean, so the initial concentration is equal to zero. The local age of air was only calculated for group 1 because the ventilation efficiency index methodology requires a uniform tracer gas assumption in the area of study. The local age of air must be calculated for the same area where the pollutants are being emitted. Furthermore, the spatial average concentration in urban intersections for group 1 was normalized, as indicated in Equation 25.

Equation 25
$$C_n = \frac{C \times Vol}{EI \times E_{vol} \times \bar{\tau}_{p,ref}}$$

The reference local age of air is the local age of air obtained for Case 1c for each corresponding wind speed condition.

4.3 Results and discussion

The contribution of various wind conditions (low velocity, medium velocity, and high velocity) in the dispersion of pollutants inside urban intersections was determined for groups 1 and 2.

The airflow of the arrays of buildings plotted at z: 0.25H under the three wind speed conditions (low, medium, and high, shown in Figure 4.4) is presented in Figure 4.7. The wind simulations indicate that the street intersections A and D, and street intersections B and C, have symmetrical behaviour in the y: 7.5W axis. Figure 4.7 (a) shows that the direction of the inflow velocity (positive stream-wise direction) is predominant through the entire domain, from the west to the east. This predominant westerly wind reaches farther in the urban streets depending on the magnitude of the inlet wind condition. In the scenario with the lower wind speed, the wind reaches the second column of buildings (between intersection A and intersection B); however, it reaches further for the high velocity condition (downstream in intersection B). This is because the friction of buildings and the ground inhibit the approaching wind flow to a greater extent in the domain, and creates helical vortices at the corners of the buildings. Figure 4.7 (b) shows the streamlines at the cross-section y: 7.5W indicated in Figure 4.7 (a) for low, medium, and high velocity. Figure 4.7 (b) shows that the flow decelerates in front of the buildings before it enters intersection A. Consequently, there is a separation of the flow, both in the span-wise and vertical directions. As the flow separates after it passes the edges of the buildings, a channelling effect is created in intersection A for the streets parallel to the direction of the inlet velocity. The top and lateral views of Figure 4.7 (b) show clockwise vortices behind buildings in the z-direction, indicating that the vertical exchange predominates. The top and lateral views of Figure 4.7 (b) show the three-dimensional nature of the vortices. Small-scale vortices are created in the x- and y-directions and propitiate the exchange between the intersecting streets, but they are mainly observed at lower heights (from ground to 0.25H). The vortices observed behind buildings in intersection B appear to be weakened and are located on the leeward side of the street canyon. By comparison, the vortices behind buildings in intersection A are located on the windward side of the street canyon.

The local age of air was calculated for Case 1a–intersection A, Case 1b–intersection B, Case 1c–intersection A and intersection B under low, medium, and high wind conditions (Figure 4.8). The local age of air was not calculated in intersections C and D, and only information about intersection A and B is presented because, as mentioned before, the behavior is symmetrical.

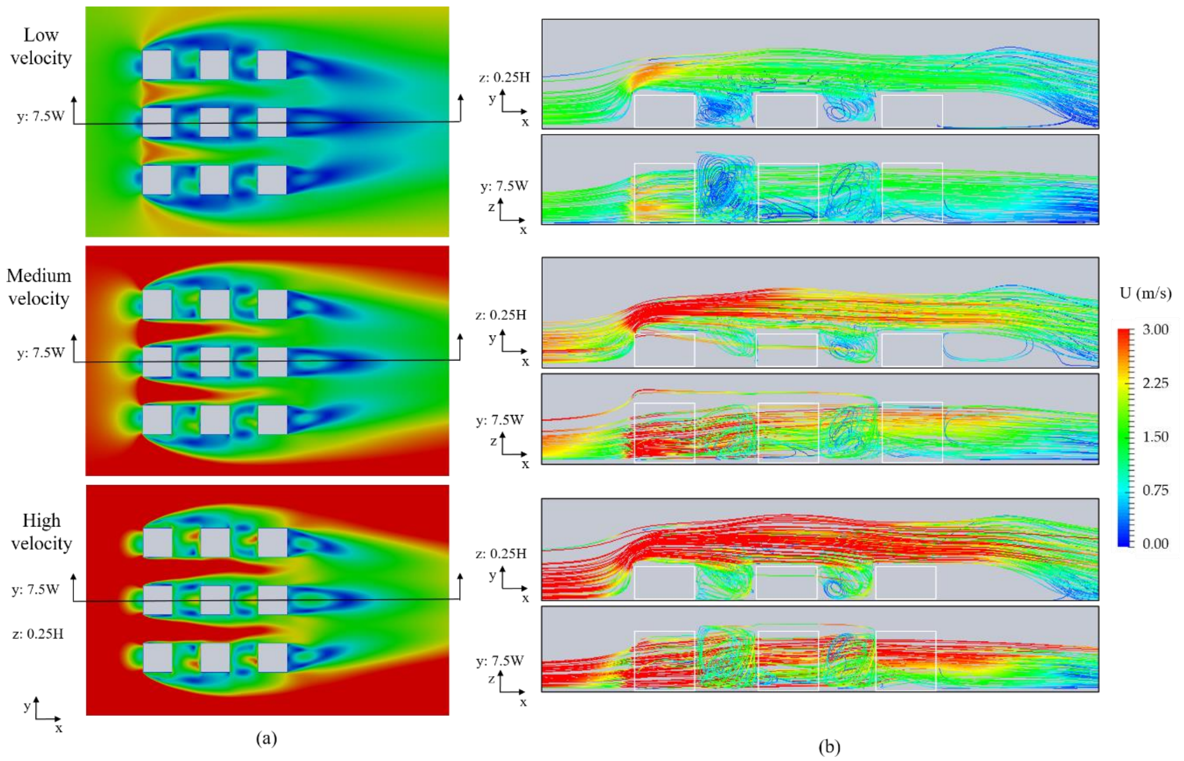

Figure 4.7. (a) Airflow pattern top view at z: 0.25H for low velocity, medium velocity, and high velocity. (b) Streamlines at the cross-section y: 7.5W top view (z: 0.25H) and lateral view (y:7.5W) for low velocity, medium velocity, and high velocity.

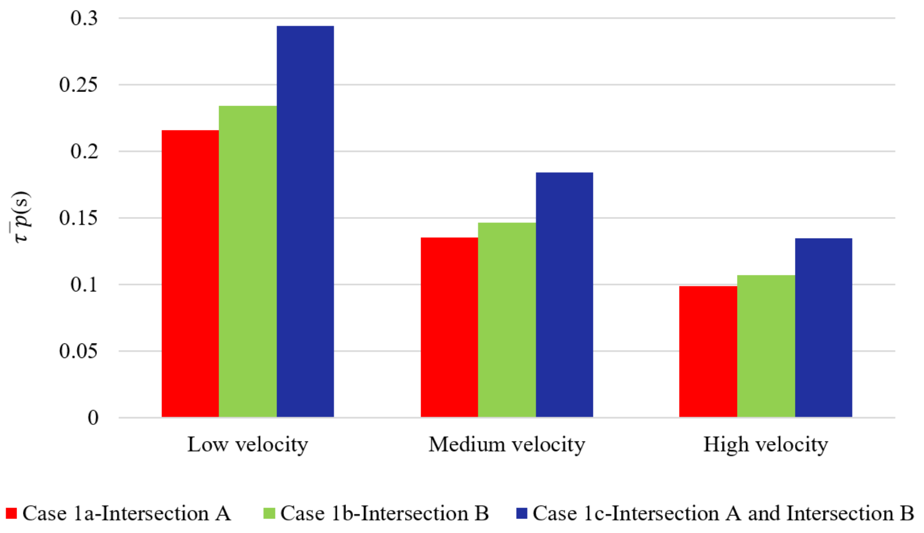

Figure 4.8. Results of the local age of air for Case 1a–intersection A, Case 1b–intersection B, and Case 1c–intersection A and intersection B.

These results indicate that the intersection with the best ventilation was Case 1a–intersection A for the three wind conditions because the young air needed less time to refresh this urban intersection. Additionally, the results indicate that intersection A in Case 1a, intersection B in

Case 1b, and intersection A and intersection B in Case 1c improved their pedestrian ventilation proportionally with the wind velocity increment.

Figure 4.9 shows the results of the normalized concentration for Case 1a, Case 1b, and Case 1c under the three different velocities (low, medium, and high) at z: 0.25H.

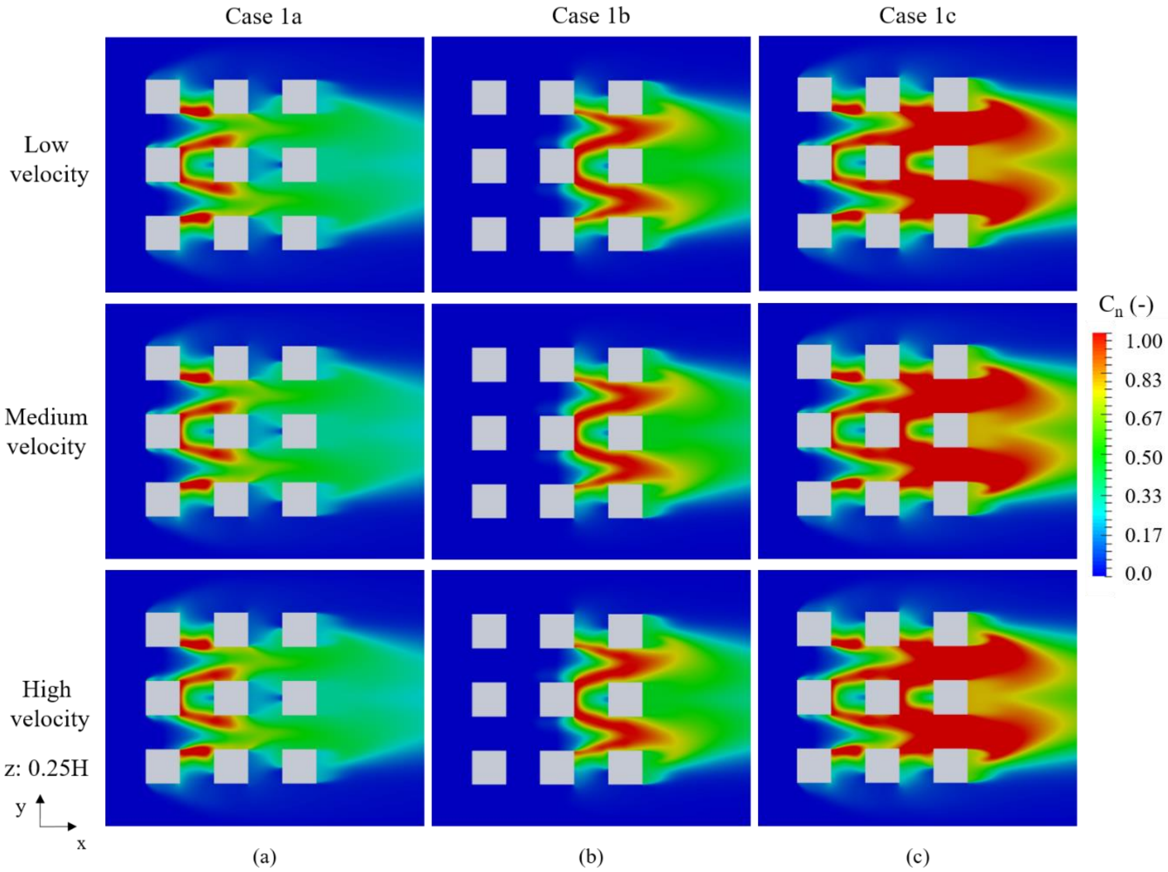

Figure 4.9. Normalized concentration field (low velocity, medium velocity, and high velocity) for (a) Case 1a, (b) Case 1b, and (c) Case 1c at z: 0.25H.

The normalized concentrations of the three wind conditions show little difference (almost negligible) because the wind speed and the concentration have an inverse proportional relationship and the emission intensity is the same for all cases. This normalized concentration shows the inverse relationship between the local age of air and the concentration. These results indicate that the concentration level linearly depends on the local age of air and the emission intensity. However, the pattern of concentration distribution is independent of this and depends on the source locations.

To better appreciate the influence of the wind conditions, the difference in the normalized concentration is presented in Figure 4.10. The normalized concentration at low velocity is subtracted from the normalized concentration at medium velocity, and normalized concentration at medium velocity is subtracted from the high velocity. The results of the subtraction indicate that, in areas where the concentration is in red (behind buildings in intersection A and intersection B), higher velocity propitiates a higher concentration of pollutant. On the contrary, the blue areas indicate that lower inlet wind speeds contribute to a higher concentration of contaminants in the leeward side of intersection A, and the street normal to the inflow velocity in intersection B. However, these differences are very low, so are almost neglectable.

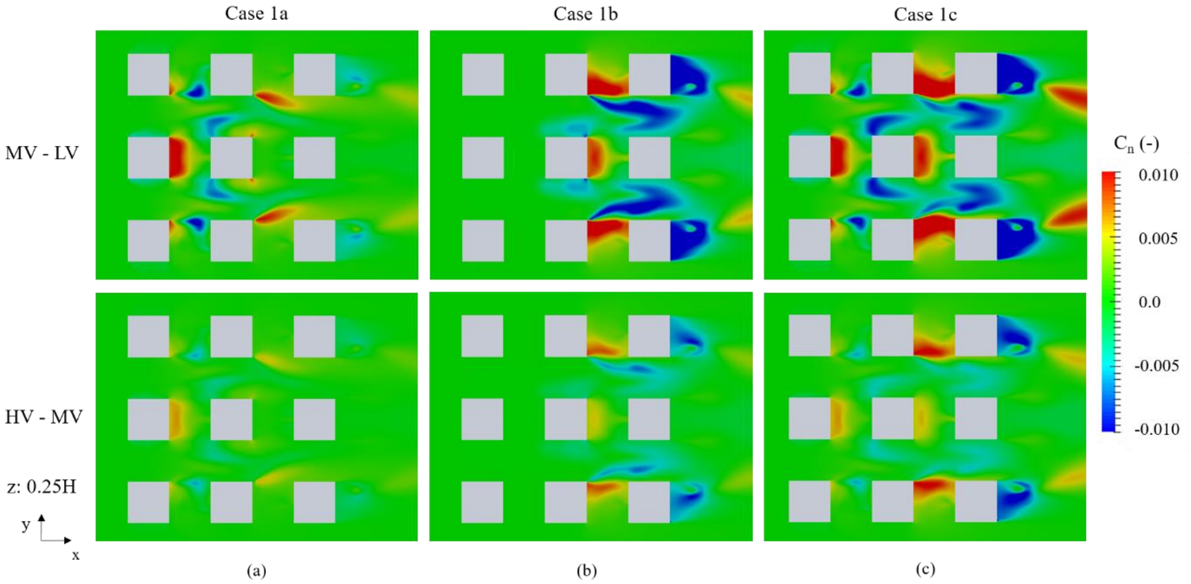

Figure 4.10. Difference of the normalized concentration field (medium velocity, MV, minus low velocity, LV, and high velocity, HV, minus medium velocity, MV) for (a) Case 1a, (b) Case 1b, and (c) Case 1c at z: 0.25H.

In Figure 4.11, the results of the concentration field for the analyzed wind conditions (low velocity, medium velocity, and high velocity) for group 2 (Case 2a parallel and Case 2b perpendicular emission area) are presented. In the Case 2a parallel emission location, intersection B has a higher concentration at every wind speed. However, the area most affected by the high levels of contaminants is the street located downstream in intersection B. For Case 2b perpendicular emission area, intersection A and intersection B are both affected, however, intersection B is more severely so. The contaminants remain trapped behind buildings in intersections A and B due to the eddy formation highlighted in Figure 4.7. Hence, we can conclude that contaminants are displaced from one intersection to another for Case 2a, but the wind does not promote the entrance of contaminants to the streets located perpendicular to the inlet velocity. By comparison, in Case 2b the contaminants are mainly concentrated in a specific area in the urban intersection. High concentration regions around the source extend farther in the direction of the mean flow. The concentration decreases with the distance from the source and the spatial distribution of the normalized concentration is substantially influenced by the location.

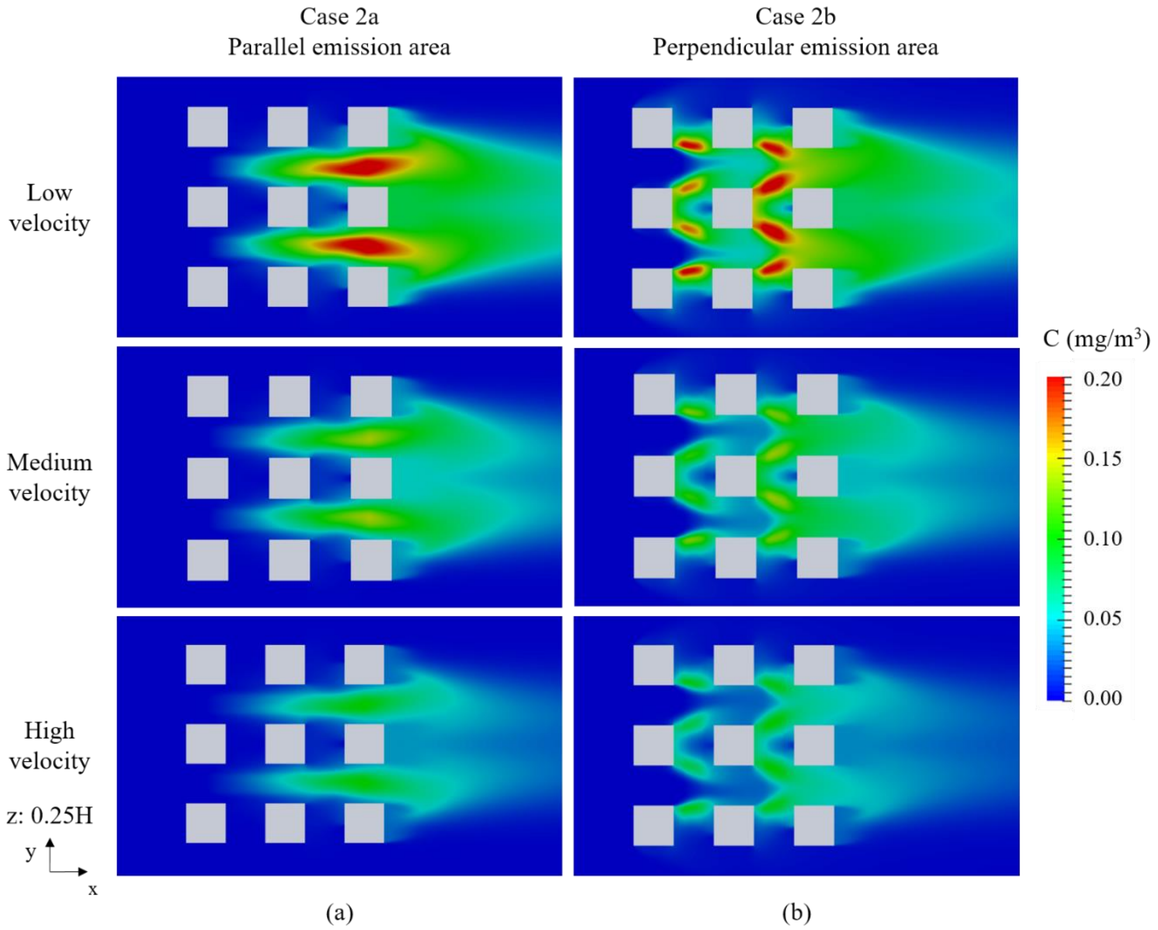

Figure 4.11. Concentration field for the analyzed inlet wind conditions (low velocity, medium velocity, and high velocity) for group 2: (a) Case 2a, parallel emission area; and (b) Case 2b, perpendicular emission area.

4.4 Conclusions

The conclusions about the influence of urban intersection on the ventilation efficiency are indicate as follow:

- The variation of the inlet wind velocity —meteorological variable— has little influence on the contaminant’s displacement to secondary streets.
- The variation of the inlet wind velocity —meteorological variable— reduce the levels of pollutants but does not alter the distribution of contaminants in the intersections.

- The distribution of pollutants inside urban areas depends significantly on the location of the source.
- This research outcome contributes to the better planning of urban areas depending on primary or secondary street sources of pollution. Furthermore, if the typical wind conditions are known, the exposure to contaminants could be controlled by planning pedestrian sidewalks or pedestrian traffic lights in urban intersections with lower levels of air pollution.

CHAPTER 5. ASSESSMENT OF A REAL URBAN ENVIRONMENT USING COUPLED CFD AND CHEMICAL REACTION MODELING

5.1 Introduction

In microscale environments, many factors such as vehicle emissions, street canyon configuration, surface heating, and chemical reactions are dynamically involved in the dispersion of pollutants. A number of studies have tried to model these factors using CFD. To evaluate surface heating, Kim and Baik (2001) systematically characterized two-dimensional flow regimes with the presence of street bottom heating, although failed to take heating of buildings into account. Xie *et al.* (2005) considered the impact of heating of three idealized sunlit wall configurations on pollutant dispersion in a two-dimensional computational domain perpendicular to the street canyon wind direction; later, Kim and Baik (2010) extended this work by examining the effects of street-bottom and building-roof heating on flow fields in a three-dimensional ideal urban canyon setting. This work highlighted the importance of including street-bottom and building roof heating in three-dimensional flow models. Bottillo *et al.* (2014) remarked on the effect of solar radiation in an urban street canyon with three-dimensional flow field under different ambient wind conditions, confirming the impact of the velocity on the heat transfer process.

Meanwhile, studies about the dispersion of reactive pollutants inside street canyon were conducted by Baker *et al.* (2004) using a simple $NO–NO_2–O_3$ photochemistry model to evaluate the isothermal dispersal and chemistry in and above street canyons with an aspect ratio of one. Baik *et al.* (2007) extended this work by showing, with a simple street canyon model and an aspect ratio of one, the importance of the building surface radiation effects on the wind flow pattern in urban areas when modeling reactive pollutant dispersion. In the following years, Kwak and Baik (2012) calculated the photochemical reaction of pollutants in and above an idealized street canyon using a two-dimensional CFD model coupled for the first time with a Carbon Bond Mechanism IV (CBM-IV) (Gery *et al.*, 1989). Similarly, Kwak and Baik (2014) used an idealistic two-dimensional model with urban surface, radiation and chemical processes to focus on the diurnal variation of NO_x and O_3 exchange. In the chapter a CFD model coupled with a CBM-IV chemical model to represent reactive pollutants inside street canyons is employed.

Despite significant effort, there is still a lack of research in non-idealized three-dimensional environments which restricts the ability to simulate pollutant concentrations at street level in complex urban areas. One of the main reasons for this is the specification of boundary conditions for realistic urban areas. Some authors have overcome this drawback by coupling mesoscale models with CFD simulations, for example, Baik *et al.* (2009) used a CFD model coupled to a mesoscale meteorological model to examine urban flow and pollutant dispersion in a densely built-up area of Seoul. Tewari *et al.* (2010) reported the benefits of coupling a microscale transport and dispersion model with a mesoscale numerical weather prediction model; significant improvements were observed when wind fields were produced by downscaling a meteorological model output as the initial and boundary CFD conditions. Recently, Kwak *et al.* (2015) developed an integrated three-dimensional model that coupled CFD with mesoscale meteorological and chemistry-transport models to simulate the air pollution from 09:00 to 18:00 local time in Seoul. In this work, the Weather Research and Forecasting model (WRF) (Skamarock and Klemp, 2008) and the Community Multiscale Air Quality model (CMAQ) (Byun and Schere, 2006) are employed as mesoscale meteorological and air quality models to obtain boundary conditions for CFD.

This section of the doctoral dissertation attempts to model in a broader way the interaction of the emission source, the urban form and the meteorological variables and their influence on the dispersion of pollutants. In this chapter, an evaluation of the concentration of reactive pollutants in a realistic urban street canyon domain over 24 hours by integrating a CFD model coupled with a chemical reaction model (CBM-IV), a radiation model, and boundary conditions from WRF-CMAQ is conducted. The first objective will be to couple CFD with the chemical reaction model (CBM-IV) to describe urban dynamics with high resolution. The second is to validate the CFD coupled chemical reaction model by comparing the numerical simulation results of a realistic urban street canyon against the observed data collected from monitoring stations situated near the roadside. The final objective is to assess the roadside pollutant dispersion in realistic city blocks with the CFD coupled chemical reaction model.

5.2 Methodology

5.2.1 CFD settings

For this chapter, the standard k-ε turbulence model (Equation 9 and Equation 10) was employed and the scalar transport equation was coupled with the CBM-IV chemical model as indicated in Equation 18. Air was modeled as an incompressible viscous flow, and the buoyancy forces were treated with the Boussinesq approximation. Moreover, the energy equation (Equation 6) was used to evaluate the influence of the radiation on the flow pattern and dispersion of pollutants. Considerations about the influence of shortwave radiation (direct solar radiation) and longwave radiation (diffuse solar radiation) were considered by a surface energy budget model of the ground (Ikejima *et al.*, 2011) shown as follows:

Equation 26 $$(1-\alpha_g)S\downarrow -\sigma T_i^4 + f_{i,sky}R\downarrow +\sigma\sum f_{i,j}T_j^4 - H = Q_G$$

In Equation 26, the emissivity for longwave radiation was omitted because it was assumed to be 1 for all surfaces. Similarly, a slightly modified building envelope model (Cortes *et al.*, 2015) accounted for the radiation received in the air from the walls and roof surfaces of buildings (Equation 27).

Equation 27 $$(1-\alpha_{bs})S\downarrow -\sigma T_{bso}^4 + f_{i,sky}R\downarrow +\sigma\sum f_{bso,j}T_j^4 +\rho_0 C_p C_H u(T_{bso}-T_{ao}) = Q_w$$

The finite volume method was used to discretize all the equations. The first order Euler method was utilized as the time discretization scheme and the power law scheme as the discretization scheme of the convection and diffusion terms in the governing equations. Moreover, the Semi-Implicit Method for Pressure-Linked Equations (SIMPLE) algorithm was employed as the pressure-velocity coupling algorithm (Patankar, 1980). The solar radiation and view factor were calculated following the method of Ikejima *et al.* (2011).

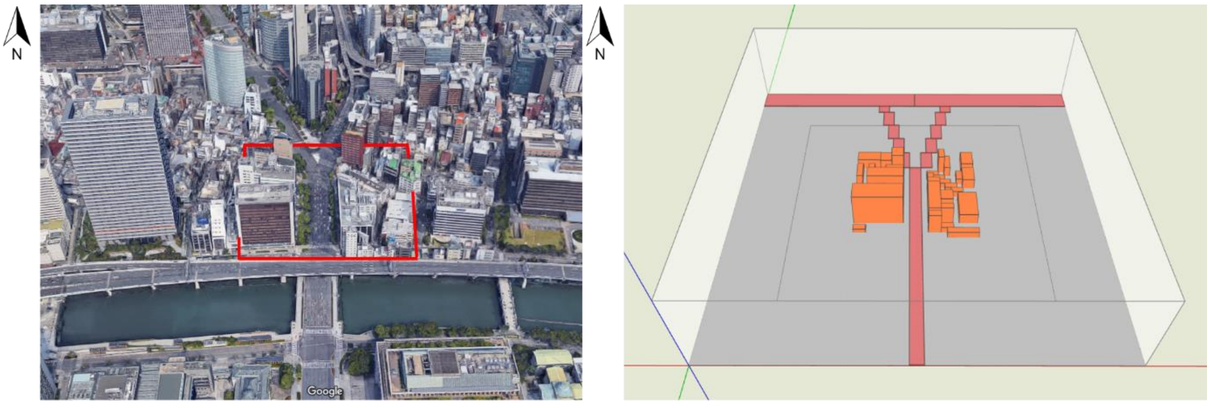

(a) (b)

Figure 5.1. (a) Google Maps tridimensional Earth view of Umeda-Shinmichi (34.70°N, 135.50°E) (b) Computational domain

The three-dimensional CFD domain was set up in Umeda-Shinmichi (34.70°N, 135.50°E), Osaka City, Japan (Figure 5.1a), where there is a typical urban street canyon layout with five roads flanked by twenty-two buildings (Figure 5.1b). The information about the length, width, and height of every building was obtained by the results of the survey on land use conducted by Osaka City in 2005. The height of the array of buildings was from 12 to 48 meters.

The size of the calculation domain was 600 m × 600 m × 150 m, and the analysis area was defined as 200 m × 200 m × 150 m (Figure 5.2a). The hexahedral mesh was 93 × 93 × 51 in the x-, y- and z-directions, respectively (Figure 5.2), and a grid interval of 3.33 m in x- and y-direction was set.

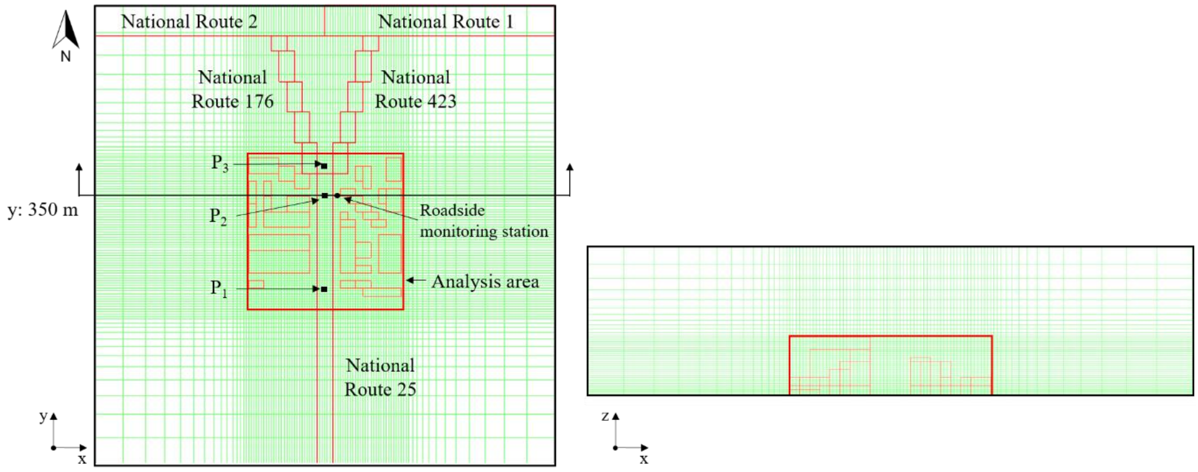

(a) (b)

Figure 5.2. Mesh view of the CFD calculation domain and analysis area. (a) the x-y view shows the reference points P_1 located at y = 230m, point P_2 located at y: 350 m, and point P_3 located at y: 390 m; (b) x-z view located at z: 1.5 m.

5.2.2 Boundary conditions

The boundary conditions of the CFD domain for temperature, wind speed and wind direction and those for air pollutant concentrations were obtained from results of meteorological simulations by WRF v3.7 (Figure B 1) and air quality simulations by CMAQ v5.1 (Figure B 2), respectively. Supplementary Material in Appendix B (Figure B 3 and Table B 1) correspondingly show modeling domains and configurations for the WRF-CMAQ simulation. The simulation was conducted over seven modeling domains from domain 1 (D1), covering East Asia with 64-km grids, to domain 7 (D7), covering Osaka Prefecture with 1-km grids, for a period from June 24 to August 31, 2010. The vertical domain consisted of 30 layers with the middle heights of the first, second and third layers being 28 m, 92 m, and 190 m, respectively. The physics parameterizations and input data for WRF and the chemical mechanisms, including the Carbon Bond mechanism developed in 2005 (CB05) (Yarwood *et al.*, 2010), the next generation model of CBM-IV, for CMAQ were the same as those used by Shimadera *et al.* (2016). Emission data for CMAQ were produced from the same datasets as those used by Uranishi *et al.* (2019), including the Japan Auto-Oil Program Emission Inventory-Data Base for vehicles (JEI-DB) developed by the Japan Petroleum Energy Center (2010). As shown in Appendix B Figure B 3, there are substantial NO_x emissions from vehicles, industrial areas and large point sources in Osaka City.

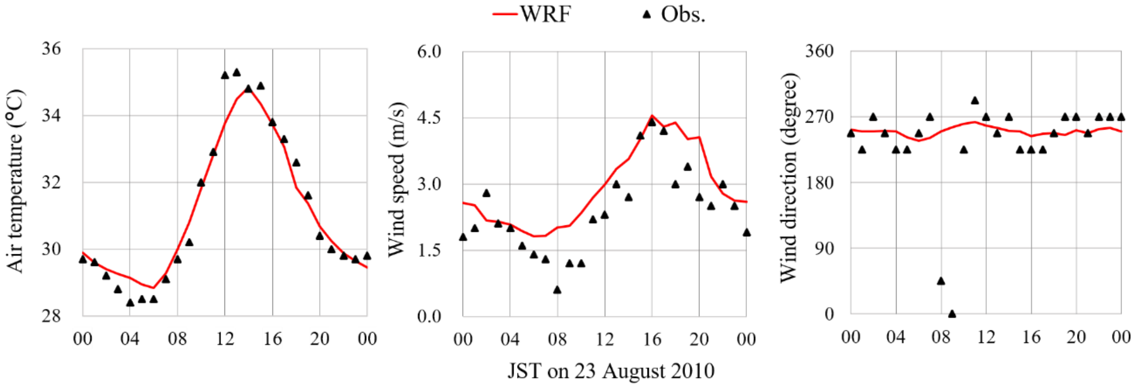

(a) (b) (c)

Figure 5.3. Diurnal variations of WRF-simulated and observed (a) air temperature; (b) wind speed; (c) wind direction at the Osaka Meteorological Observatory on August 23, 2010

August 23, 2010, was chosen as the calculation period for the 24-hour unsteady state CFD analysis because of a very clear and calm conditions so that photochemical reactions might play an essential role in air quality on the day. The WRF and CMAQ simulations in D7 on the day were compared with observed data by the Japan Meteorological Agency (JMA) at the Osaka Meteorological Observatory (34.68°N, 135.52°E) (Appendix B, Figure B 3) and by the Ministry of the Environment of Japan (MOE) at Kokusetsu-Osaka station (34.68°N, 135.54°E) (Appendix B, Figure B 3). Figure 5.3 shows diurnal variations of the observed and WRF-simulated ground-level air temperature, wind speed and direction at the Osaka Meteorological Observatory, which is located 2 km southeast of Umeda-Shinmichi, on August 23. The WRF-simulated air temperature agreed reasonably well with the observed data, showing a RMSE value of 0.48 °C. The model also approximately captured the temporal variation of wind speed with a slight overestimation, indicated with a RMSE of 0.71 m/s. Both in the observation and WRF simulation, the wind direction mainly ranged from southwest to west, except at 08:00 and 09:00 JST (UTC+9) in the observation under calm conditions. For the case of the wind direction, the RMSE was 43 degrees.

Figure 5.4 shows the diurnal variation of observed and CMAQ-simulated ambient concentrations of NO, NO_2 and O_3 at the Kokusetsu-Osaka station, which is located 4 km east-southeast of Umeda-Shinmichi. CMAQ approximately captured the variations and magnitudes of ambient concentrations of these air pollutants, except for NO_2 which was underestimated during the daytime. The RMSE of the NO, NO_2 and O_3 were 1.39 ppb, 7.03 ppb, and 11.43 ppb, respectively. These results indicate that WRF-CMAQ successfully produced meteorological and concentration fields around the study area for the CFD boundary conditions.

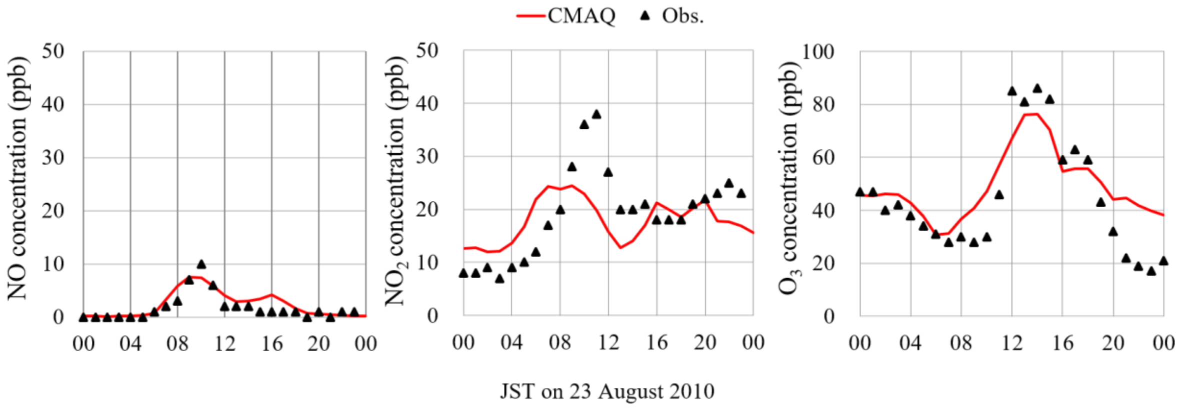

(a) (b) (c)

Figure 5.4. Diurnal variations of CMAQ-simulated and observed (a) NO, (b) NO_2 and (c) O_3 concentrations at the Kokusetsu-Osaka station for monitoring ambient air pollution on August 23, 2010.

Due to the coarser vertical resolution of the WRF-CMAQ model compared with CFD, Monin-Obukhov Similarity Theory (MOST) was employed to determine the boundary vertical distribution of air temperature and wind components. Under MOST, the WRF-CMAQ data at heights 28 m and 92 m of Umeda-Shinmichi in D7 were used with a roughness length of 0.1 m. Moreover, the concentration under 28 m was the same value as the data at 28 m, and over 28 m the values were interpolated linearly. Because CB05 used in CMAQ has more species of VOCs than CBM-IV used in CFD, VOC species in CMAQ output were lumped into those in CBM-IV. Once this data was obtained, the vertical distribution from WRF-CMAQ at every hour and the values interpolated linearly in between each hour, the boundary conditions at transient state were set for the CFD model.

The emission rate from vehicles used as CMAQ input data was derived from JEI-DB with a horizontal resolution of 1 km × 1 km. The total emission rate from automobiles in the CFD domain was estimated from the JEI-DB data by multiplying the area ratio of the CFD domain to a grid of JEI-DB (0.36). Then, the total emission was allocated into the five national routes shown in Figure 5.2 (National Route 1, National Route 2, National Route 176, National Route 423, National Route 25) by considering the traffic volume of each road provided by Japanese Ministry of Land . Figure 5.5 shows the diurnal variation of the NO_x ($NO + NO_2$) emission rate for 24 hours for every national route. The average NO_2/NO_x emission ratio for the indicated area (0.36) was 0.1799. The information about the NO_x emission rate for every national route was used as the boundary condition for the emission rate and updated every hour in the CFD coupled chemical reaction model. As discussed above, models of 24 hours are mandatory since rush hours represent the peak emission rates.

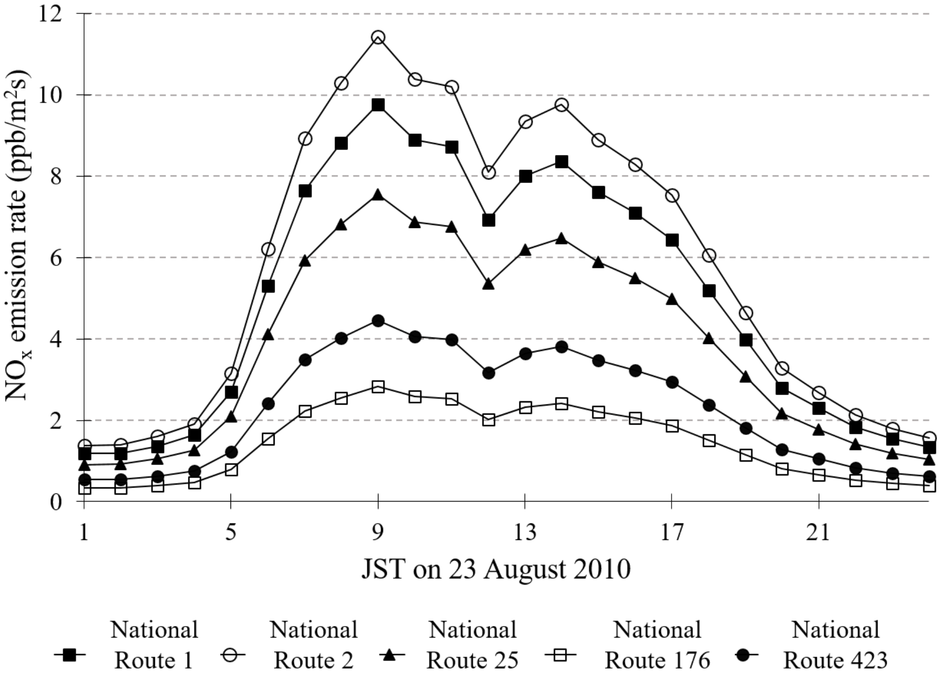

Figure 5.5. Diurnal variation of NOx (NO + NO2) emissions rates on August 23, 2010.

5.3 Results and discussion

The dispersion of pollutants inside urban street canyons is a phenomenon heavily reliant on urban form (building geometry) and emissions (traffic related). Therefore, it is quite challenging to capture the local aspects in mesoscale simulations software, such as WRF-CMAQ, because low model resolution cannot be well characterized (Martilli and Santiago, 2006). In Figure 5.6, the validation of the CFD model coupled chemical reaction model (CBM-IV) against CMAQ-simulated and the roadside monitoring station data by the Atmospheric Environmental Regional Observation System (AEROS) at Umeda-Shinmichi station (34.69°N, 135.50°E) about the diurnal variations of NO and NO_2 on August 23, 2010, is shown. For the case of O_3 in Figure 5.6c, the comparison is only made between CMAQ and CFD simulations since the roadside monitoring station did not record data for Ozone.

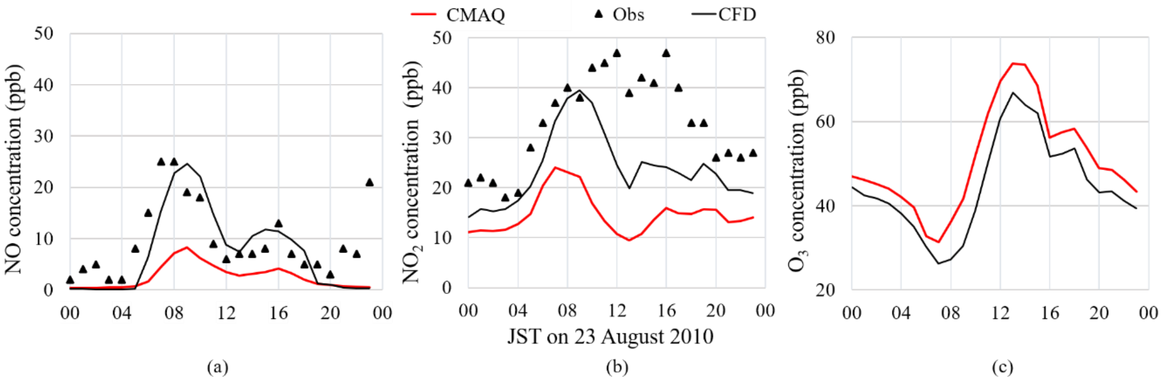

Figure 5.6. Diurnal variations in CMAQ-simulated, observed, and CFD-simulated (a) NO; (b) NO_2; (c) O_3 concentrations at the Umeda-Shinmichi station for monitoring roadside air pollution on August 23, 2010.

The RMSE in the case of the CFD-simulated results for NO and NO_2 were 6.35 ppb and 11.44 ppb, however, for the CMAQ-simulated results the values of the RMSE were 9.08 ppb and 20.35 ppb, respectively. Compared with CMAQ-simulated results, CFD coupled chemical reaction model is more accuracy describing NO and NO_2 concentrations. The NO levels from the CFD calculation behaved almost identical to the observed data. As it is shown, there are some underestimations in NO_2 concentration from 09:00 JST to 18:00 JST, most likely due to the underestimation of the daytime background concentration indicated in Figure 5.4. The O_3 concentrations output from CMAQ and CFD simulations show similar behavior, however the CFD simulations show consistently lower concentration. The results of this validation indicate how important it is to study particular emissions, the reactions in the modeling of air pollution and the actual configuration of the urban street canyon using coupled CFD and chemical reaction modeling.

The behavior of NO, NO_2, and O_3 inside the analysis area, where the main road, National Route 25, runs perpendicular to the wind inflow with a width of 20 m, and sidewalks of 10 m at both sides was investigated. The emission line source was placed in the middle of National Route 25 with a width of 20 meters and a height of 1-meter from the ground.

Figure 5.7 shows the airflow pattern in the analysis area at 08:00, 12:00, 16:00, and 20:00 JST top view at z = 1.5 m. The height of z = 1.5 m is the same height as the monitoring station at which the data was compared. The flow field in Figure 5.7 indicates a wind circulation restriction behind buildings typically present in street canyons. Throughout the day the inlet wind direction was sustained from west to east, and from afternoon (16:00 JST) until nighttime (20:00 JST) when the velocity reached maximum levels. Inside the street canyon (National Route 25), the wind flow moved mainly from south to north through the entire street canyon because of open space in the southwest part of the analysis area. Moreover, counterclockwise vortices developed in the road at 08:00, 12:00, 16:00 and 20:00 JST behind buildings in the left side of the road, as result of the wind that speeded up and went through the channels between constructions. At noon, a shift in the wind flow in the superior side of the analysis area from west to east was observed, creating more vortices between buildings located downstream. Additionally, Figure 5.7 demonstrates the importance of three-dimensional analyses since some eddies are seen at buildings corners where shear stresses are common and responsible for some turbulence in the flow.

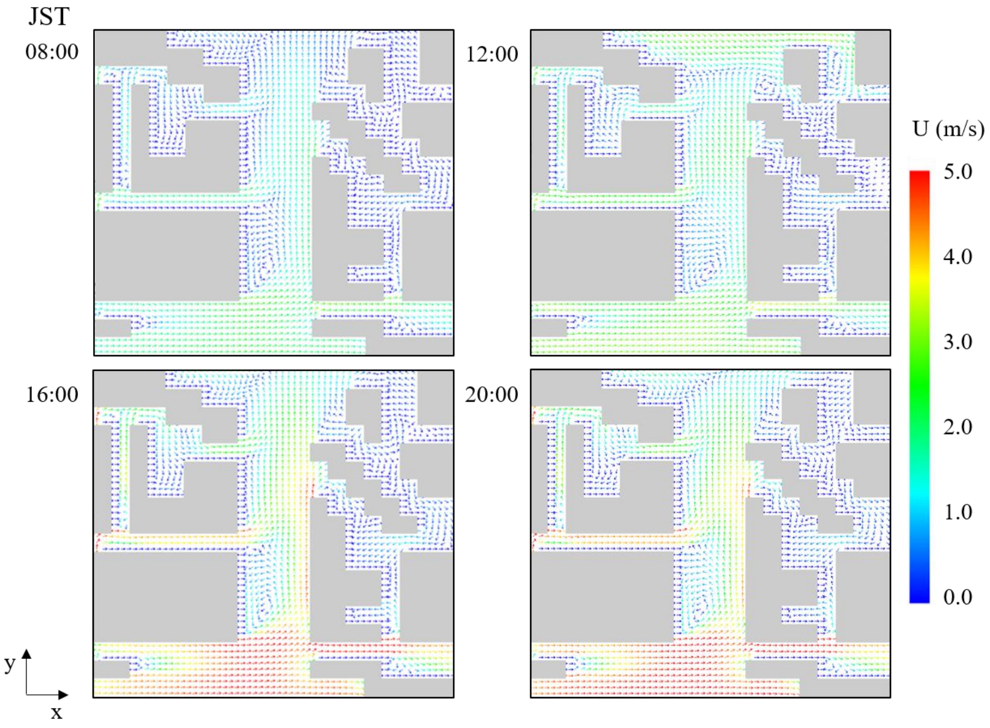

Figure 5.7. Airflow patterns at 08:00, 12:00, 16:00, and 20:00 JST, top view at z: 1.5 m

Figure 5.8 shows the spatial distribution of NO, NO_2, and O_3 concentrations at 08:00, 12:00, 16:00, and 20:00 JST top view z = 1.5 m. High levels of NO and NO_2 remained in the middle of the street canyon because building configurations do not allow their removal. During the day, the behavior of the contaminants changes depending on the emission rates and wind velocity. During the morning rush hours (07:00 – 09:00 JST), the NO_x concentration in the street canyon increase, and stay on the street from 08:00 JST until 12:00 JST, especially behind buildings where vortices are observed. At 16:00 JST, the vehicle emission rate decreases, and the wind speed is higher, so NO_2 concentrations reduced. However, at 20:00 JST, some slight concentration of NO_2 is still observed due to the titration reaction between NO and O_3 (Sillman, 1999). Throughout the day, it is observed in Figure 5.8, a different distribution between O_3 and NO_2 due to the proximity of the traffic-related emission (NO) that leads to NO_x titration. Besides, it is shown in Figure 5.8 that high levels of NO and NO_2 are located in the right superior quadrant at noon because of the shift of the wind direction observed in Figure 5.7.

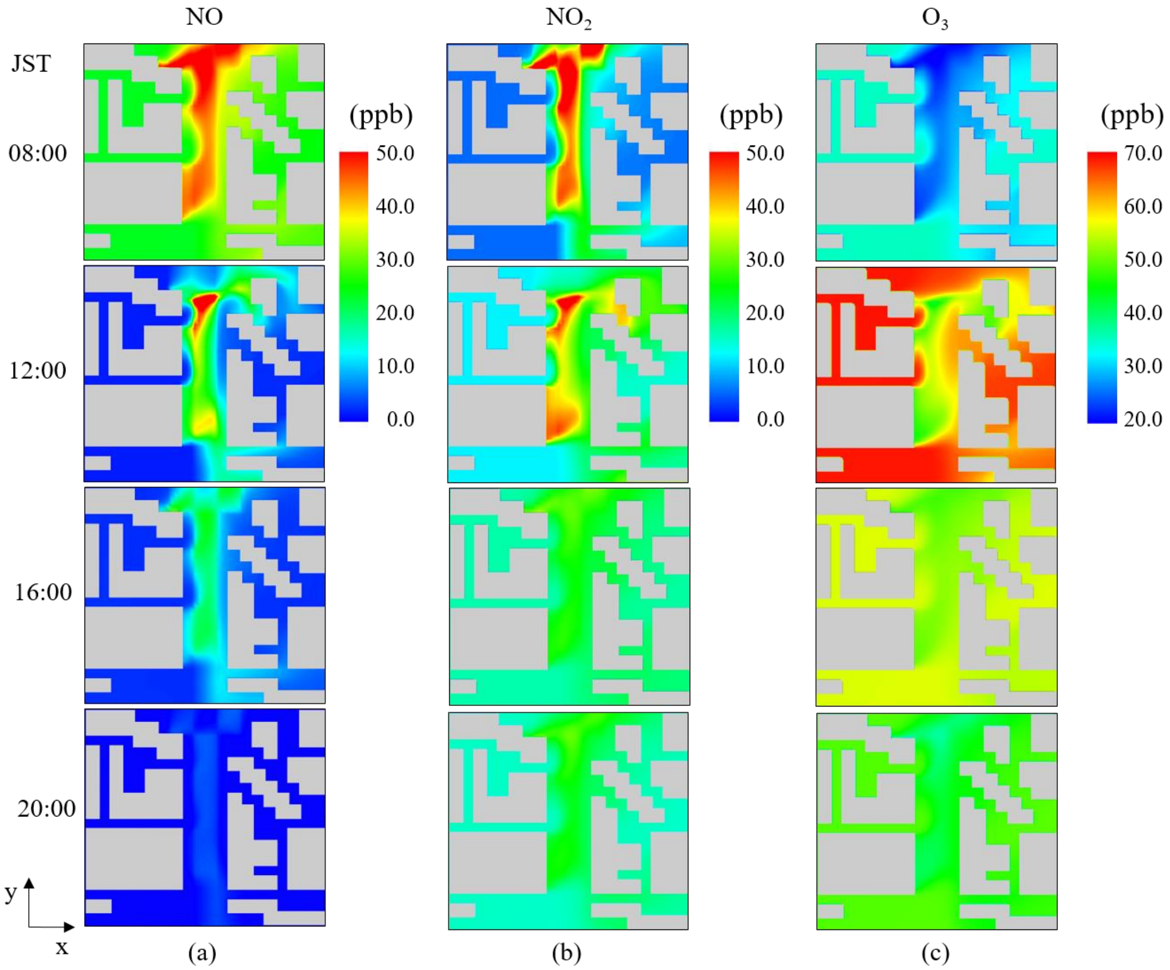

Figure 5.8. Spatial distribution of (a) NO, (b) NO_2, and (c) O_3 concentration at 08:00, 12:00, 16:00 and 20:00 JST, top view at z: 1.5 m

Figure 5.9 shows the airflow patterns at 08:00, 12:00, 16:00, and 20:00 JST at y = 350 m. Weaker wind flow is seen on the leeward side of buildings and stagnation of the flow is evident upwind which is characteristic of wind flow around buildings (Tominaga *et al.*, 2015). When the wind flow encounters buildings the flow is separated and the wind speed decreases, depending on the magnitude of the wind speed the scale of the vortices changes when moving in the positive z-direction. From the lateral view isolated roughness flow is observed, however, some perturbation is induced due to the proximity of the buildings.

As mentioned before, adequate characterization of the dispersion and reaction of pollutants inside a real street urban environment requires the modeling of the effects of buildings and ground heating. The results of the analysis of the influence of the temperature on the analysis area, in specific Point 1, Point 2, and Point 3 (Figure 5.2) are presented in the Appendix B, Figure B 6. The analysis of the temperature profiles showed no considerable difference under and above the heights of the buildings (~30 meters). Thus, the influence of air temperature on the transport of contaminants for this urban street layout was considered minimal and almost negligible in comparison with the wind flow.

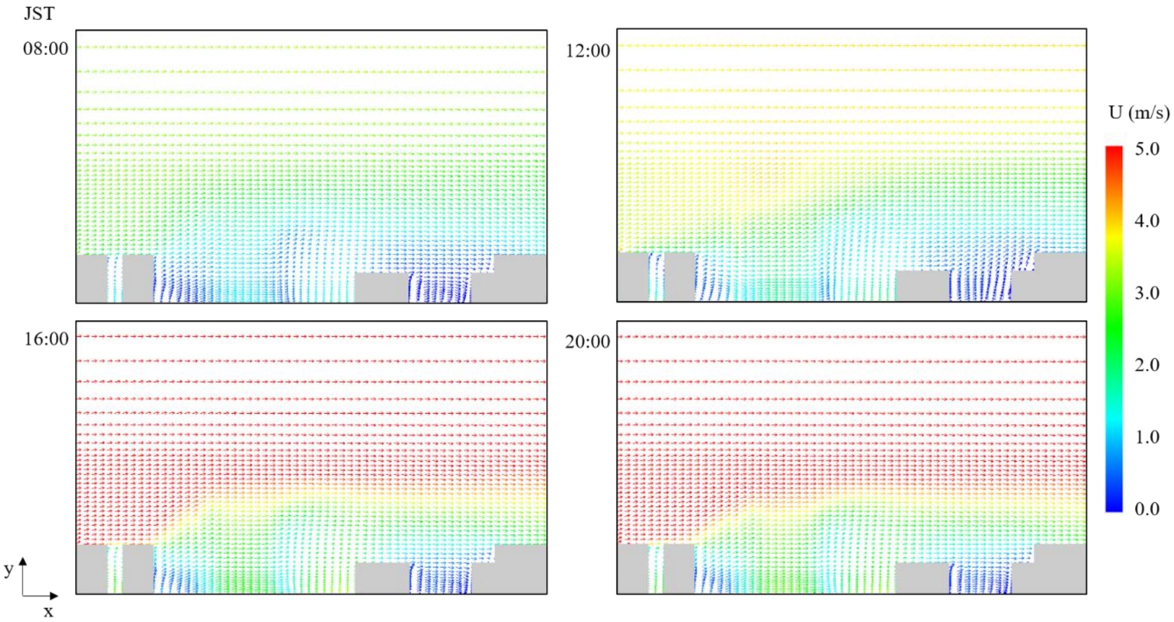

Figure 5.9. Airflow patterns at 08:00, 12:00, 16:00, and 20:00 JST, lateral view y: 350 m

Figure 5.10 shows the spatial distribution of (a) NO, (b) NO_2, and (c) O_3 concentrations at 08:00, 12:00, 16:00, and 20:00 JST at y = 350 m. Due to the vehicle exhaust located at a height of 1-meter in the middle of the analysis area, high NO and NO_2 concentrations remained near surface level, mainly from 08:00 JST to 12:00 JST. The dispersion plume of NO, NO_2, and O_3 exhibits large vertical gradient from the ground to roof level of the building. As mentioned by Melkonyan and Kuttler (2012), NO and NO_2 enhance ozone’s dissociation and production, respectively. Thus, if the NO/NO_2 ratio decreases, ozone concentrations increase. In this study, all the National Routes studied showed high emission rates with a NO/NO_2 ratio of 4:1, suggesting that the NO_x titration was the main reason for the dissociation of O_3. At 20:00 JST, even when emissions from vehicles had decreased, the NO_2 concentration in the street was still present in contrast with the concentration above roof level. The vertical exchange of air pollutants is, therefore, shown to be mainly influenced by vehicle emissions and building features.

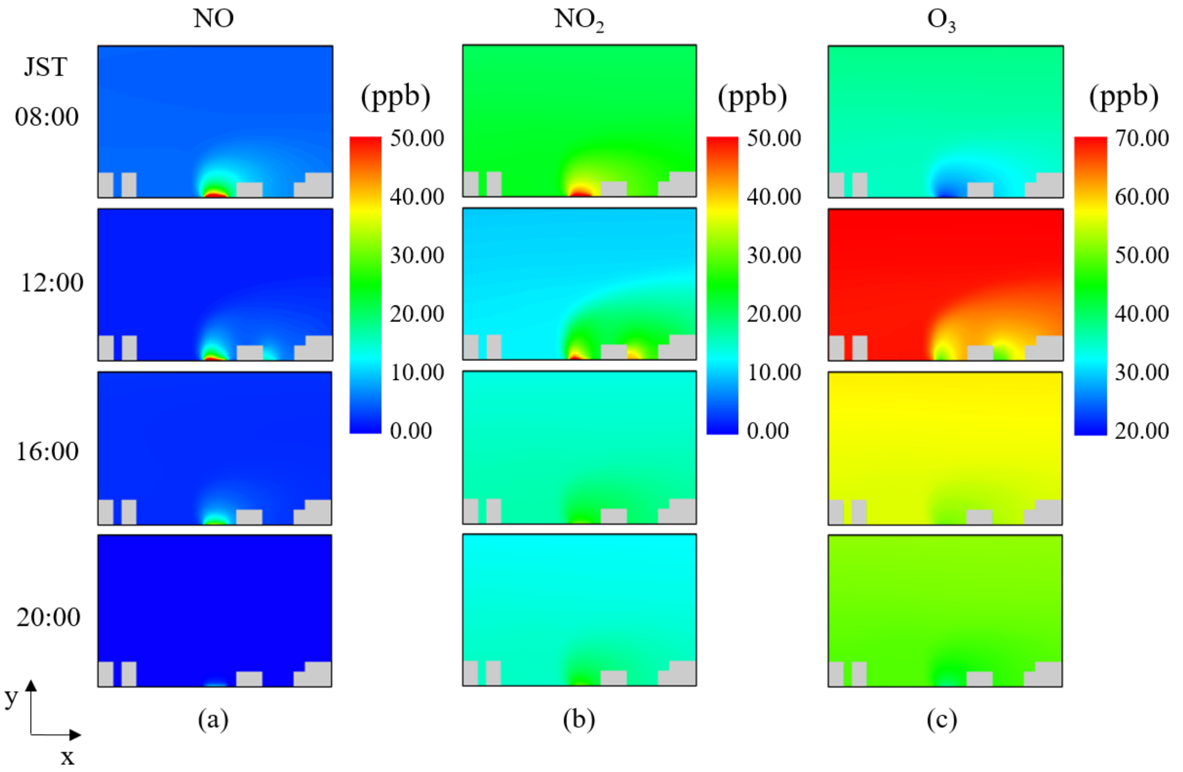

Figure 5.10. Spatial distribution of (a) NO, (b) NO_2 and (c) O_3 concentration at 08:00, 12:00, 16:00 and 20:00 JST, cross-section A-A' view (Figure 5.2a)

5.4 Conclusions

The dispersion of the contaminants was highly dependent on the reaction processes, boundary conditions and emission rates interaction in the real urban street canyon. The conclusions are summarized as follow:

- The production of NO_x or fading of O_3 were especially found in regions with low wind speed and high turbulence.
- The distribution of O_3 was directly affected by chemical reactions near the roadside, where fresh NO was being emitted (NOx titration).
- The same urban form under different meteorological variables — wind speed, wind direction— and emission rates leads to very different patterns of distribution of contaminants during the day.

- To evaluate the ventilation performance of a specific urban environment, considerations about the diurnal variations of meteorological variables and emission sources (rates and reactive pollutants) need to be assessed.
- Finally, this work is an intent to find better representations of boundary conditions and to step forward in the incorporation of radiation models and reactive models with the purpose of simulate urban-like environments, satisfactorily. Further efforts in this kind of research are necessary to reproduce the reality of urban areas and the implications that may have in people exposed during the day to these concentrations.

CHAPTER 6. GENERAL CONCLUSIONS

6.1 Summary of main findings and conclusions

The distribution of air pollutants inside urban areas is conditioned by the interaction of three main factors: the pollution sources, the urban form and components, and meteorological variables. Many studies have addressed these three factors to determine their relationship and predict air pollution dispersion.

Understanding the interaction of the pollutant sources, urban form, and components, and the meteorological variables, besides appropriate quantitively and qualitatively assessment of these interactions commonly found in urban areas, will allow better urban planning practices to reduce air pollution in cities.

This doctoral dissertation employed computational fluids dynamics to assess the ventilation efficiency of urban areas using suitable ventilation efficiency indices and to model comprehensively the urban environment processes and their influence on the dispersion of pollutants. Computational fluid dynamics was employed because it helps to reduce the time required to optimize a physical model and has some advantages in comparison with wind tunnel and operational models.

In chapters three and four, suitable ventilation efficiency indices to describe the capability of the air from outside the urban areas to refresh the city environment were investigated.

In the third chapter, the local age of air, the purging flow rate, and the air exchange efficiency were employed to describe the behavior of the wind within a real urban environment and an ideal urban environment. Some of the findings were that the number of building and building height influence on the capacity of the wind to refresh the urban environment. For an ideal urban environment, the local age of air was related to the street width and buildings height. The purging flow rate indicated that the pollutants are flush away from the domain at a higher rate when the street width is larger and the number of buildings is small. The air exchange efficiency described the type of flow pattern for the ideal urban environment: a short-circuiting flow. This means that the supplied air resided a short time without passing the occupied space (the buildings behave as a simple obstacle). We concluded that the air exchange efficiency was not quite suitable to consider the vertical wind flow and mass rate interchange at the top of the analysis domain (z: 4 m).

The fourth chapter, an evaluation about the dispersion of pollutants in street intersections and nearby connecting streets using the local age of air was conducted. The results indicate that the wind plays a vital role in determining the distribution of the contaminants. Similarly, the emission source location can enhance the distribution of contaminants inside urban intersections. These results demonstrated that the concentration level linearly depends on the local age of air and the emission intensity. However, the pattern of concentration distribution depends on the location of the source.

In chapter number five, the dispersion of reactive pollutants in a realistic urban street canyon domain over 24 hours by integrating a CFD model coupled with a chemical reaction model, a radiation model, and boundary conditions from WRF-CMAQ was evaluated. The conclusions were that the dispersion of the contaminants is highly dependent on the reaction processes, boundary conditions and emission rates. The production of NO_x or fading of O_3 were especially found in regions with low wind speed and high turbulence, and NO_x titration was noted to be of great importance. The O_3 behavior was directly affected by chemical reactions near the roadside, where fresh NO was being emitted, and was consequently controlled by the NO_x distribution. The grid resolution of WRF-CMAQ appears to have a strong influence when representing the boundary conditions, and still, due to their limitations (1 km × 1 km minimum grid size) the particularities that accompany urban areas such as street, highways, unequal height of buildings, sidewalks cannot be well represented.

6.2 Recommendations for future research

The study of the urban environment requires evaluating different characteristics that vary depending on the microscale meteorological conditions, the specific built-up infrastructure, and the respective emission settings. However, it is imperative to cohesively parametrize the urban area modeling to contribute to the urbanization process and reduce the exposition of residents to air pollutants.

Futures studies that consider the variation of the urban forms and components (introduction of urban trees, open spaces, water bodies, variation of packing density), different meteorological variables (wind directions, humidity, temperature), and other types of the ventilation efficiency indices should be considered.

This doctoral dissertation intends to advance the description of the factors influencing the dispersion of air pollutants in urban areas. However, studies to find better representations of boundary conditions, reactive models, ventilation performance, turbulence induce by cars, emission sources, the influence of traffic lights in the emission rates are necessary to simulate urban environments satisfactorily. Further efforts in this kind of research are essential to reproduce the reality of urban areas and its implications on inhabitants.

REFERENCES

Ahmad, K., Khare, M., & Chaudhry, K. K. (2005). Wind tunnel simulation studies on dispersion at urban street canyons and intersections—a review. *Journal of Wind Engineering and Industrial Aerodynamics, 93*(9), 697-717. doi:10.1016/j.jweia.2005.04.002

Ai, Z. T., & Mak, C. M. (2017). CFD simulation of flow in a long street canyon under a perpendicular wind direction: Evaluation of three computational settings. *Building and Environment, 114*, 293-306. doi:10.1016/j.buildenv.2016.12.032

Akashi, T. *Creating the 'Wind Paths' in the City to Mitigate Urban Heat Island Effects*. Retrieved from https://www.kenken.go.jp/japanese/contents/cib/w101_old/pdf/04.pdf

AKL. (2018). AKL Flow designer. Retrieved from http://www.akl.co.jp/en/

Antoniou, N., Montazeri, H., Wigo, H., Neophytou, M. K. A., Blocken, B., & Sandberg, M. (2017). CFD and wind-tunnel analysis of outdoor ventilation in a real compact heterogeneous urban area: Evaluation using "air delay". *Building and Environment, 126*, 355-372. doi:10.1016/j.buildenv.2017.10.013

ASHRAE. (2007). Ventilation for Acceptable Indoor Air Quality. In *Definitions* (pp. 48). Atlanta, Georgia: ASHRAE.

Bady, M., Kato, S., & Huang, H. (2008). Towards the application of indoor ventilation efficiency indices to evaluate the air quality of urban areas. *Building and Environment, 43*(12), 1991-2004. doi:10.1016/j.buildenv.2007.11.013

Baik, J.-J., Kang, Y.-S., & Kim, J.-J. (2007). Modeling reactive pollutant dispersion in an urban street canyon. *Atmospheric Environment, 41*(5), 934-949. doi:10.1016/j.atmosenv.2006.09.018

Baik, J.-J., Kim, J.-J., & Fernando, H. J. S. (2003). A CFD Model for Simulating Urban Flow and Dispersion. *Journal of Applied Meteorology, 42*, 1636-1648.

Baik, J.-J., Park, S.-B., & Kim, J.-J. (2009). Urban Flow and Dispersion Simulation Using a CFD Model Coupled to a Mesoscale Model. *Journal of Applied Meteorology and Climatology, 48*(8), 1667-1681. doi:10.1175/2009jamc2066.1

Baker, J., Walker, H. L., & Cai, X. (2004). A study of the dispersion and transport of reactive pollutants in and above street canyons—a large eddy simulation. *Atmospheric Environment, 38*(39), 6883-6892. doi:10.1016/j.atmosenv.2004.08.051

Ben Ramoul, L., Korichi, A., Popa, C., Zaidi, H., & Polidori, G. (2018). Numerical study of flow characteristics and pollutant dispersion using three RANS turbulence closure models. *Environmental Fluid Mechanics, 19*(2), 379-400. doi:10.1007/s10652-018-9628-2

Blocken, B. (2015). Computational Fluid Dynamics for urban physics: Importance, scales, possibilities, limitations and ten tips and tricks towards accurate and reliable simulations. *Building and Environment, 91*, 219-245. doi:10.1016/j.buildenv.2015.02.015

Bottillo, S., De Lieto Vollaro, A., Galli, G., & Vallati, A. (2014). CFD modeling of the impact of solar radiation in a tridimensional urban canyon at different wind conditions. *Solar Energy, 102*, 212-222. doi:10.1016/j.solener.2014.01.029

Brady, J., & O'Mahony, M. (2011). Travel to work in Dublin. The potential impacts of electric vehicles on climate change and urban air quality. *Transportation Research Part D: Transport and Environment, 16*(2), 188-193. doi:10.1016/j.trd.2010.09.006

Buccolieri, R., & Sandberg, M. (2008). *Study of the effects of building density and overall shape of a city on pollutant dispersion by combination of wind tunnel experiments and CFD simulations*.

Buccolieri, R., Sandberg, M., & Di Sabatino, S. (2010). City breathability and its link to pollutant concentration distribution within urban-like geometries. *Atmospheric Environment, 44*(15), 1894-1903. doi:10.1016/j.atmosenv.2010.02.022

Byun, D., & Schere, K. L. (2006). Review of the Governing Equations, Computational Algorithms, and Other Components of the Models-3 Community Multiscale Air Quality (CMAQ) Modeling System. *Applied Mechanics Reviews, 59*(2). doi:10.1115/1.2128636

Chang, J. C., & Hanna, S. R. (2004). Air quality model performance evaluation. *Meteorology and Atmospheric Physics, 87*(1-3). doi:10.1007/s00703-003-0070-7

Chen, L., Hang, J., Sandberg, M., Claesson, L., & Di Sabatino, S. (2017). The Influence of building packing densities on flow adjustment and city breathability in urban-like geometries. *Procedia Engineering, 198*, 758-769. doi:10.1016/j.proeng.2017.07.127

Chen, L., Hang, J., Sandberg, M., Claesson, L., Di Sabatino, S., & Wigo, H. (2017). The impacts of building height variations and building packing densities on flow adjustment and city breathability in idealized urban models. *Building and Environment, 118*, 344-361. doi:10.1016/j.buildenv.2017.03.042

Comsol. (2020). Heat Transfer: Conservation of Energy. Retrieved from https://www.comsol.jp/multiphysics/heat-transfer-conservation-of-energy#ref

Cortes, A., Murashita, Y., Matsuo, T., Kondo, A., Shimadera, H., & Inoue, Y. (2015). Numerical evaluation of the effect of photovoltaic cell installation on urban thermal environment. *Sustainable Cities and Society, 19*, 250-258. Retrieved from <Go to ISI>://WOS:000367398900025

Cui, P.-Y., Li, Z., & Tao, W.-Q. (2016). Wind-tunnel measurements for thermal effects on the air flow and pollutant dispersion through different scale urban areas. *Building and Environment, 97*, 137-151. doi:10.1016/j.buildenv.2015.12.010

Dauchet, L., Hulo, S., Cherot-Kornobis, N., Matran, R., Amouyel, P., Edme, J. L., & Giovannelli, J. (2018). Short-term exposure to air pollution: Associations with lung function and inflammatory markers in non-smoking, healthy adults. *Environment International, 121*(Pt 1), 610-619. doi:10.1016/j.envint.2018.09.036

Dayang, W., Yun, Z., Qingxiang, L., Xuesong, D., & Yong, Z. (2012, September 2-6). *Numerical study on wind-pressure characteristics of a high-rise building in group of buildings.* Paper presented at the The Seventh International Colloquium on Bluff Body Aerodynamics and Applications Shanghai, China.

De Paul, F. T., & Sheih, C. M. (1986). Measurements of wind velocities in a street canyon. *Atmospheric Environment, 20*, 455-459.

Di Sabatino, S., Pulvirenti, B., & Kumar, P. (2017). *Mixing and transport within real street intersections: the case of Marylebone Street, London (UK)*. Paper presented at the 18th International Conference on Harmonisation within Atmospheric Dispersion Modelling for Regulatory Purposes, Bologna, Italy.

Duan, R.-R., Hao, K., & Yang, T. (2020). Air pollution and chronic obstructive pulmonary disease. *Chronic Diseases and Translational Medicine*. doi:10.1016/j.cdtm.2020.05.004

Edussuriya, P., Chan, A., & Ye, A. (2011). Urban morphology and air quality in dense residential environments in Hong Kong. Part I: District-level analysis. *Atmospheric Environment, 45*(27), 4789-4803. doi:10.1016/j.atmosenv.2009.07.061

Etheridge, D., & Sandberg, M. (1996). *Building Ventilation: Theory and Measurement*. New York: WILEY.

Gál, T., & Unger, J. (2009). Detection of ventilation paths using high-resolution roughness parameter mapping in a large urban area. *Building and Environment, 44*(1), 198-206. doi:10.1016/j.buildenv.2008.02.008

Gao, Y., Wang, Z., Liu, C., & Peng, Z.-R. (2019). Assessing neighborhood air pollution exposure and its relationship with the urban form. *Building and Environment, 155*, 15-24. doi:10.1016/j.buildenv.2018.12.044

Gery, M. W., Whitten, G. Z., Killus, J. P., & Dodge, M. C. (1989). A photochemical kinetics mechanism for urban and regional scale computer modeling. *Journal of Geophysical Research, 94*, 12.

Gonzalez-Olivardia, Matsuo, T., Shimadera, H., & Kondo, A. (2017). Use of local age of air to study the relation between ventilaiton efficiency and building configuration. *Journal of Heat Island Institute International, 12*, 6.

Gonzalez-Olivardia, Zhang, Q., Matsuo, T., Shimadera, H., & Kondo, A. (2019). Analysis of Pollutant Dispersion in a Realistic Urban Street Canyon Using Coupled CFD and Chemical Reaction Modeling. *Atmosphere, 10*(9). Retrieved from <Go to ISI>://WOS:000489177300001

Grimmond, C. S. B., & Oke, T. R. (1998). Aerodynamic properties of urban areas derived from analysis of surface form. *Journal of Applied Meteorology, 38*, 1262.

Hang, J., & Li, Y. (2011). Age of air and air exchange efficiency in high-rise urban areas and its link to pollutant dilution. *Atmospheric Environment, 45*(31), 5572-5585. doi:10.1016/j.atmosenv.2011.04.051

Hang, J., Luo, Z., Sandberg, M., & Gong, J. (2013). Natural ventilation assessment in typical open and semi-open urban environments under various wind directions. *Building and Environment, 70*, 318-333. doi:10.1016/j.buildenv.2013.09.002

Hang, J., Sandberg, M., & Li, Y. (2009a). Age of air and air exchange efficiency in idealized city models. *Building and Environment, 44*(8), 1714-1723. doi:10.1016/j.buildenv.2008.11.013

Hang, J., Sandberg, M., & Li, Y. (2009b). Effect of urban morphology on wind condition in idealized city models. *Atmospheric Environment, 43*(4), 869-878. doi:10.1016/j.atmosenv.2008.10.040

Hang, J., Wang, Q., Chen, X., Sandberg, M., Zhu, W., Buccolieri, R., & Di Sabatino, S. (2015). City breathability in medium density urban-like geometries evaluated through the pollutant transport rate and the net escape velocity. *Building and Environment, 94*, 166-182. doi:10.1016/j.buildenv.2015.08.002

Hsieh, C.-M., & Huang, H.-C. (2016). Mitigating urban heat islands: A method to identify potential wind corridor for cooling and ventilation. *Computers, Environment and Urban Systems, 57*, 130-143. doi:10.1016/j.compenvurbsys.2016.02.005

Huang, Y.-D., Hou, R.-W., Liu, Z.-Y., Song, Y., Cui, P.-Y., & Kim, C.-N. (2019). Effects of Wind Direction on the Airflow and Pollutant Dispersion inside a Long Street Canyon. *Aerosol and Air Quality Research, 19*(5), 1152-1171. doi:10.4209/aaqr.2018.09.0344

Ikejima, K., Kondo, A., & Kaga, A. (2011). The 24-h unsteady analysis of air flow and temperature in a real city by high-speed radiation calculation method. *Building and Environment, 46*(8), 1632-1638. doi:10.1016/j.buildenv.2011.01.029

Japan Petroleum Energy Center. (2010). *Technical report of the Japan Auto-Oil Program: emission inventory of road transport in Japan* (JPEC-2011AQ-02-06). Retrieved from Japan:

Japanese Ministry of Land, I., Transport and Tourism, . National Road traffic volume census. Retrieved from http://www.mlit.go.jp/road/census/h22-1/index.html

Kenty, K. L., Poor, N. D., Kronmiller, K. G., McClenny, W., King, C., Atkeson, T., & Campbell, S. W. (2007). Application of CALINE4 to roadside NO/NO2 transformations. *Atmospheric Environment, 41*(20), 4270-4280. doi:10.1016/j.atmosenv.2006.06.066

Kim, J.-J., & Baik, J.-J. (1999). A Numerical Study of Thermal Effects on Flow and Pollutant Dispersion in Urban Street Canyons. *Journal of Applied Meteorology, 38*, 1249-1261.

Kim, J.-J., & Baik, J.-J. (2001). Urban street-canyon flows with bottom heating. *Atmospheric Environment, 35*, 3395-3404.

Kim, J.-J., & Baik, J.-J. (2010). Effects of street-bottom and building-roof heating on flow in three-dimensional street canyons. *Advances in Atmospheric Sciences, 27*(3), 513-527. doi:10.1007/s00376-009-9095-2

Kittaka, K., & Miyazaki, H. (2014). Relationship between wind direction and air temperature in the Osaka center city determined using fixed point observation. *Journal of Heat Island Institute International, 9-2*.

Kubota, T., & Ahmad, S. (2006). Wind environment evaluation of neighborhood areas in major towns of malaysia. *Journal of Asian Architecture and Building Engineering, 5*.

Kwak, K.-H., & Baik, J.-J. (2012). A CFD modeling study of the impacts of NOx and VOC emissions on reactive pollutant dispersion in and above a street canyon. *Atmospheric Environment, 46*, 71-80. doi:10.1016/j.atmosenv.2011.10.024

Kwak, K.-H., & Baik, J.-J. (2014). Diurnal variation of NOx and ozone exchange between a street canyon and the overlying air. *Atmospheric Environment, 86*, 120-128. doi:10.1016/j.atmosenv.2013.12.029

Kwak, K.-H., Baik, J.-J., Ryu, Y.-H., & Lee, S.-H. (2015). Urban air quality simulation in a high-rise building area using a CFD model coupled with mesoscale meteorological and chemistry-transport models. *Atmospheric Environment, 100*, 167-177. doi:10.1016/j.atmosenv.2014.10.059

Launder, B. E., & Spalding, D. B. (1973). The numerical computation of turbulent flows. *Computer methods in applied mechanics and engineering 3*(2), 269-289. doi:https://doi.org/10.1016/0045-7825(74)90029-2

Leitl, B. M., & Meroney, R. N. (1997). Car exhaust dispersion in a street canyon Numerical critique of a wind tunnel experiment. *Journal of Wind Engineering and Industrial Aerodynamics, 67 & 68*, 293-304.

Li, C., Wang, Z., Li, B., Peng, Z.-R., & Fu, Q. (2019). Investigating the relationship between air pollution variation and urban form. *Building and Environment, 147*, 559-568. doi:10.1016/j.buildenv.2018.06.038

Lihua, H., Yuandong, H., Wenrong, H., Liming, H., & Yixin, R. (2015). Effect of Wind Direction on Airflow and Pollutant Dispersion Inside a Street Intersection. *Nature Environment and Pollution Technology, 14*(2), 355-360.

Lin, M., Hang, J., Li, Y., Luo, Z., & Sandberg, M. (2014). Quantitative ventilation assessments of idealized urban canopy layers with various urban layouts and the same building packing density. *Building and Environment, 79*, 152-167. doi:10.1016/j.buildenv.2014.05.008

Liu, F., Qian, H., Zheng, X., Zhang, L., & Liang, W. (2017). Numerical Study on the Urban Ventilation in Regulating Microclimate and Pollutant Dispersion in Urban Street Canyon: A Case Study of Nanjing New Region, China. *Atmosphere, 8*(12). doi:10.3390/atmos8090164

Liu, Y., Wu, J., Yu, D., & Ma, Q. (2018). The relationship between urban form and air pollution depends on seasonality and city size. *Environ Sci Pollut Res Int, 25*(16), 15554-15567. doi:10.1007/s11356-018-1743-6

Martilli, A., & Santiago, J. L. (2006). CFD simulation of airflow over a regular array of cubes. Part II: analysis of spatial average properties. *Boundary-Layer Meteorology, 122*(3), 635-654. doi:10.1007/s10546-006-9124-y

Mei, S.-J., Hu, J.-T., Liu, D., Zhao, F.-Y., Li, Y., & Wang, H.-Q. (2019). Airborne pollutant dilution inside the deep street canyons subjecting to thermal buoyancy driven flows: Effects of representative urban skylines. *Building and Environment, 149*, 592-606. doi:10.1016/j.buildenv.2018.12.050

Mei, S.-J., Hu, J.-T., Liu, D., Zhao, F.-Y., Li, Y., Wang, Y., & Wang, H.-Q. (2017). Wind driven natural ventilation in the idealized building block arrays with multiple urban morphologies and unique package building density. *Energy and Buildings, 155*, 324-338. doi:10.1016/j.enbuild.2017.09.019

Melkonyan, A., & Kuttler, W. (2012). Long-term analysis of NO, NO2 and O3 concentrations in North Rhine-Westphalia, Germany. *Atmospheric Environment, 60*, 316-326. doi:10.1016/j.atmosenv.2012.06.048

Nazarian, N., & Kleissl, J. (2016). Realistic solar heating in urban areas: Air exchange and street-canyon ventilation. *Building and Environment, 95*, 75-93. doi:10.1016/j.buildenv.2015.08.021

Nonomura, Y., Kobayashi, N., Tominaga, Y., & Mochida, A. (2003). The cross comparison of CFD results for flowfield around building models (part 3): The wind tunnel test for the varification models on the flowfield around building blocks. *Japan association for wind engineering, 95*, 83-84. doi:https://doi.org/10.14887/jaweam.2003.0.41.0

OpenCFD. (2020). OpenFOAM: User Guide v2006 The open source CFD toolbox. Retrieved from https://www.openfoam.com/documentation/guides/latest/doc/guide-turbulence-ras-k-epsilon.html

Panagiotou, I., Neophytou, M. K., Hamlyn, D., & Britter, R. E. (2013). City breathability as quantified by the exchange velocity and its spatial variation in real inhomogeneous urban geometries: an example from central London urban area. *Sci Total Environ, 442*, 466-477. doi:10.1016/j.scitotenv.2012.09.001

Paraschiv, S., & Paraschiv, L.-S. (2019, 19-21 September 2018). *Analysis of traffic and industrial source contributions to ambient air pollution with nitrogen dioxide in two urban areas in Romania*. Paper presented at the Technologies and Materials for Renewable Energy, Environment and Sustainable, Athens, Greece.

Patankar, S. V. (1980). *Numerical Heat Transfer and Fluid Flow*. United States of America: Press Roamn by Hemisphere Publishing Corporation.

Peng, Y., Buccolieri, R., Gao, Z., & Ding, W. (2020). Indices employed for the assessment of “urban outdoor ventilation” - A review. *Atmospheric Environment, 223*. doi:10.1016/j.atmosenv.2019.117211

Peng, Y., Gao, Z., Buccolieri, R., & Ding, W. (2019). An Investigation of the Quantitative Correlation between Urban Morphology Parameters and Outdoor Ventilation Efficiency Indices. *Atmosphere, 10*(1). doi:10.3390/atmos10010033

Qin, H., Lin, P., Lau, S. S. Y., & Song, D. (2020). Influence of site and tower types on urban natural ventilation performance in high-rise high-density urban environment. *Building and Environment, 179*. doi:10.1016/j.buildenv.2020.106960

Qin, Y., & Kot, S. C. (1993). Dispersion of vehicular emission in street canyons, Guangzhou city South China (P.R.C) *Atmospheric Environment, 27B*, 283-291.

Rajagopalan, P., Lim, K. C., & Jamei, E. (2014). Urban heat island and wind flow characteristics of a tropical city. *Solar Energy, 107*, 159-170. doi:10.1016/j.solener.2014.05.042

Ramponi, R., Blocken, B., de Coo, L. B., & Janssen, W. D. (2015). CFD simulation of outdoor ventilation of generic urban configurations with different urban densities and equal and unequal street widths. *Building and Environment, 92*, 152-166. doi:10.1016/j.buildenv.2015.04.018

Rao, V. L. (2014). Effects of Urban Heat Island on Air pollution Concentrations. *International Journal of Current Microbiology and Applied Sciences, 3*, 388-400.

Righi, S., Lucialli, P., & Pollini, E. (2009). Statistical and diagnostic evaluation of the ADMS-Urban model compared with an urban air quality monitoring network. *Atmospheric Environment, 43*(25), 3850-3857. doi:10.1016/j.atmosenv.2009.05.016

Rodriquez, S. (2019). *Applied Computational Fluid Dynamics and Turbulence Modeling - Practical Tools, Tips and Techniques*(pp. 316). doi:https://doi.org/10.1007/978-3-030-28691-0

Santamouris, M. (2006). Special Issue of the Solar Energy Program devoted to Natural Ventilation in Urban Areas. *Solar Energy, 80*(4), 369-370. doi:10.1016/j.solener.2005.10.001

Shih, T.-H., Liou, W. W., Shabbir, A., Yang, Z., & Zhu, J. (1995). A new k-e eddy viscocity model fro high reynolds number turbulent flows. *Computers Fluids, 24*, 227-238.

Shimadera, H., Kojima, T., & Kondo, A. (2016). Evaluation of Air Quality Model Performance for Simulating Long-Range Transport and Local Pollution of PM2.5in Japan. *Advances in Meteorology, 2016*, 1-13. doi:10.1155/2016/5694251

Sillman, S. (1999). The relation between ozone, Nox and hydrocarbons in urban and polluted rural encironments. *Atmospheric Environment, 33*, 1821-1845.

Skamarock, W. C., & Klemp, J. B. (2008). A time-split nonhydrostatic atmospheric model for weather research and forecasting applications. *Journal of Computational Physics, 227*(7), 3465-3485. doi:10.1016/j.jcp.2007.01.037

Socolofsky, S. A., & Jirka, G. H. (2004). Special topics in mixing and transport processes in the environment. In *Engineering-Lectures* (5th ed.). Texas.

Solazzo, E., Vardoulakis, S., & Cai, X. (2011). A novel methodology for interpreting air quality measurements from urban streets using CFD modelling. *Atmospheric Environment, 45*(29), 5230-5239. doi:10.1016/j.atmosenv.2011.05.022

Soulhac, L., Garbero, V., Salizzoni, P., Mejean, P., & Perkins, R. J. (2009). Flow and dispersion in street intersections. *Atmospheric Environment, 43*(18), 2981-2996. doi:10.1016/j.atmosenv.2009.02.061

Taseiko, O. V., Mikhailuta, S. V., Pitt, A., Lezhenin, A. A., & Zakharov, Y. V. (2009). Air pollution dispersion within urban street canyons. *Atmospheric Environment, 43*(2), 245-252. doi:10.1016/j.atmosenv.2008.09.076

Tewari, M., Kusaka, H., Chen, F., Coirier, W. J., Kim, S., Wyszogrodzki, A. A., & Warner, T. T. (2010). Impact of coupling a microscale computational fluid dynamics model with a mesoscale model on urban scale contaminant transport and dispersion. *Atmospheric Research, 96*(4), 656-664. doi:10.1016/j.atmosres.2010.01.006

Tominaga, Y., Mochida, A., Murakami, S., & Sawaki, S. (2008). Comparison of various revised k–ε models and LES applied to flow around a high-rise building model with 1:1:2 shape placed within the surface boundary layer. *Journal of Wind Engineering and Industrial Aerodynamics, 96*(4), 389-411. doi:10.1016/j.jweia.2008.01.004

Tominaga, Y., Sato, Y., & Sadohara, S. (2015). CFD simulations of the effect of evaporative cooling from water bodies in a micro-scale urban environment: Validation and application studies. *Sustainable Cities and Society, 19*, 259-270. doi:10.1016/j.scs.2015.03.011

Tominaga, Y., & Stathopoulos, T. (2010). Numerical simulation of dispersion around an isolated cubic building: Model evaluation of RANS and LES. *Building and Environment, 45*(10), 2231-2239. doi:10.1016/j.buildenv.2010.04.004

Tominaga, Y., & Stathopoulos, T. (2012). CFD Modeling of Pollution Dispersion in Building Array: Evaluation of turbulent scalar flux modeling in RANS model using LES results. *Journal of Wind Engineering and Industrial Aerodynamics, 104-106,* 484-491. doi:10.1016/j.jweia.2012.02.004

Tominaga, Y., & Stathopoulos, T. (2013). CFD simulation of near-field pollutant dispersion in the urban environment: A review of current modeling techniques. *Atmospheric Environment, 79*, 716-730. doi:10.1016/j.atmosenv.2013.07.028

Toparlar, Y., Blocken, B., Maiheu, B., & van Heijst, G. J. F. (2017). A review on the CFD analysis of urban microclimate. *Renewable and Sustainable Energy Reviews, 80,* 1613-1640. doi:10.1016/j.rser.2017.05.248

United Nations, D. o. E. a. S. A., Population Division. (2019). World Urbanization Prospects 2018: Highlights. *(ST/ESA/SER.A/421).*

Uranishi, K., Ikemori, F., Shimadera, H., Kondo, A., & Sugata, S. (2019). Impact of field biomass burning on local pollution and long-range transport of PM2.5 in Northeast Asia. *Environmental Pollution, 244*, 414-422. doi:10.1016/j.envpol.2018.09.061

Vardoulakis, S., Fisher, B. E. A., Pericleous, K., & Gonzalez-Flesca, N. (2003). Modelling air quality in street canyons: a review. *Atmospheric Environment, 37*, 155-182.

Vardoulakis, S., Gonzalez-Flesca, N., & Fisher, B. E. A. (2002). Assessment of traffic-related air pollution in two street canyons in Paris implications for exposure studies. *Atmospheric Environment, 36*, 1025-1039.

Versteeg, H. K., & Malalasekera, W. (2007). *An Introduction to Computational fluid dynamics: The finite volume method* (Second ed.). England: Pearson Prentice Hall.

Vollaro, A., Galli, G., & Vallati, A. (2015). CFD Analysis of Convective Heat Transfer Coefficient on External Surfaces of Buildings. *Sustainability, 7*(7), 9088-9099. doi:10.3390/su7079088

Wang, X., & McNamara, K. F. (2007). Effects of street orientation on dispersion at or near urban street intersections. *Journal of Wind Engineering and Industrial Aerodynamics, 95*(9-11), 1526-1540. doi:10.1016/j.jweia.2007.02.021

Weeks, J. R. (2010). Defining Urban Areas. In *Remote Sensing of Urban and Suburban Areas* (pp. 33-45).

WHO. (2018, April 2018). Burden of disease associated with urban outdoor air pollution for 2008. *Public health, environmental and social determinants of health (PHE).* April 2018. Retrieved from https://www.who.int/phe/health_topics/outdoorair/databases/burden_disease/en/

Wilcox, D. C. (2008). Formulation of the k-w Turbulence Model Revisited. *AIAA Journal, 46*(11), 2823-2838. doi:10.2514/1.36541

Wong, K.-S. N., Edward; Yau, Raymond. (2012). Urban ventilation as a countermeasure for heat islands toward quality and sustainable city planning in Hong Kong. *Journal of Heat Island Institute International, 7-2*.

Xie, X., Huang, Z., Wang, J., & Xie, Z. (2005). The impact of solar radiation and street layout on pollutant dispersion in street canyon. *Building and Environment, 40*(2), 201-212. doi:10.1016/j.buildenv.2004.07.013

Yakhot, V., & Orszag, S. A. (1986). Renormalization Group Analysis of Turbulence. I. Basic Theory. *Journal of Scientific Computing, 1*. doi:https://doi.org/10.1007/BF01061452

Yarwood, G., Jung, J., Whitten, G. Z., Heo, G., Mellberg, J., & Estes, M. (2010). *Updates to the carbon bond mechanism for version 6 (CB6)*. Paper presented at the 9th Annual CMAS Conference, Chapel Hill, North Carolina

Yassin, M. F., Kellnerová, R., & Jaňour, Z. (2008). Impact of street intersections on air quality in an urban environment. *Atmospheric Environment, 42*(20), 4948-4963. doi:10.1016/j.atmosenv.2008.02.019

You, W., Gao, Z., Chen, Z., & Ding, W. (2017). Improving Residential Wind Environments by Understanding the Relationship between Building Arrangements and Outdoor Regional Ventilation. *Atmosphere, 8*(12). doi:10.3390/atmos8060102

Yuan, M., Huang, Y., Shen, H., & Li, T. (2018). Effects of urban form on haze pollution in China: Spatial regression analysis based on PM2.5 remote sensing data. *Applied Geography, 98*, 215-223. doi:10.1016/j.apgeog.2018.07.018

Zhang, M., Song, Y., & Cai, X. (2007). A health-based assessment of particulate air pollution in urban areas of Beijing in 2000-2004. *Sci Total Environ, 376*(1-3), 100-108. doi:10.1016/j.scitotenv.2007.01.085

APPENDIX A

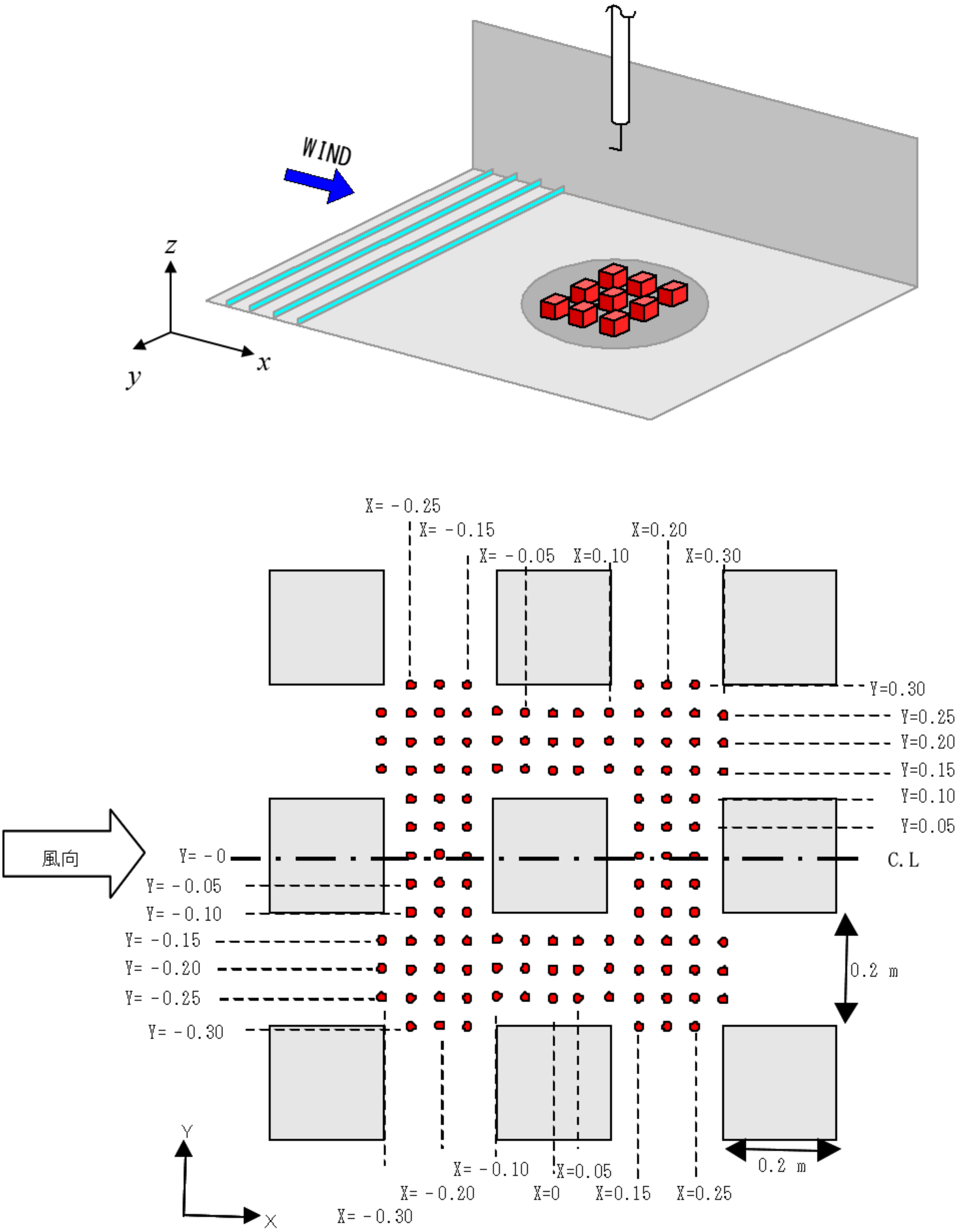

Figure A 1. Wind tunnel experiment geometry (taken from Nonomura *et al.* (2003))

Table A 1. Wind tunnel experiment inflow velocity (taken from Nonomura *et al.* (2003)

Z(mm)	Z(m)	U (m/s)	σ_u (m/s)
10	0.01	2.372	0.56
20	0.02	2.434	0.564
30	0.03	2.548	0.563
50	0.05	2.912	0.695
70	0.07	3.042	0.71
100	0.1	3.392	0.743
150	0.15	3.483	0.78
200	0.2	3.654	0.801
250	0.25	3.82	0.812
300	0.3	4.019	0.786
350	0.35	4.205	0.83
400	0.4	4.343	0.809
600	0.6	4.985	0.796
800	0.8	5.713	0.587
1000	1	6.12	0.283
1200	1.2	6.201	0.148

Vertical profile of the inflow velocity values used in Figure 4.4 for the grid sensitivity study and RANS-turbulence model sensitivity study.

Table A 2. Results for 0 degrees inflow velocity used in the grid resolution study (taken from Nonomura *et al.* (2003)

0 deg	position[m]			velocity ratio*
point	X	Y	Z	1H
63	-0.30	-0.25	0.02	1.195
54	-0.30	-0.20	0.02	1.232
45	-0.30	-0.15	0.02	0.967
31	-0.30	0.15	0.02	1.023
32	-0.30	0.20	0.02	1.175
33	-0.30	0.25	0.02	1.102
66	-0.25	-0.30	0.02	0.466
62	-0.25	-0.25	0.02	1.139
53	-0.25	-0.20	0.02	1.105
44	-0.25	-0.15	0.02	0.890
22	-0.25	-0.10	0.02	0.462
23	-0.25	-0.05	0.02	0.374
24	-0.25	0.00	0.02	0.383
25	-0.25	0.05	0.02	0.396
26	-0.25	0.10	0.02	0.522
27	-0.25	0.15	0.02	0.886
28	-0.25	0.20	0.02	1.008
29	-0.25	0.25	0.02	1.006
30	-0.25	0.30	0.02	0.553
65	-0.20	-0.30	0.02	0.572
61	-0.20	-0.25	0.02	1.023
52	-0.20	-0.20	0.02	0.972
43	-0.20	-0.15	0.02	0.787
13	-0.20	-0.10	0.02	0.512
14	-0.20	-0.05	0.02	0.493
15	-0.20	0.00	0.02	0.528
16	-0.20	0.05	0.02	0.530
17	-0.20	0.10	0.02	0.504
18	-0.20	0.15	0.02	0.810
19	-0.20	0.20	0.02	0.921
20	-0.20	0.25	0.02	0.916
21	-0.20	0.30	0.02	0.597
64	-0.15	-0.30	0.02	0.631
60	-0.15	-0.25	0.02	0.907
51	-0.15	-0.20	0.02	0.895
42	-0.15	-0.15	0.02	0.694
4	-0.15	-0.10	0.02	0.560
5	-0.15	-0.05	0.02	0.461
6	-0.15	0.00	0.02	0.554
7	-0.15	0.05	0.02	0.474
8	-0.15	0.10	0.02	0.486
9	-0.15	0.15	0.02	0.716
10	-0.15	0.20	0.02	0.854

11	-0.15	0.25	0.02	0.842
12	-0.15	0.30	0.02	0.614
59	-0.10	-0.25	0.02	0.835
50	-0.10	-0.20	0.02	0.831
41	-0.10	-0.15	0.02	0.664
103	-0.10	0.15	0.02	0.721
112	-0.10	0.20	0.02	0.817
121	-0.10	0.25	0.02	0.796
58	-0.05	-0.25	0.02	0.744
49	-0.05	-0.20	0.02	0.796
40	-0.05	-0.15	0.02	0.592
104	-0.05	0.15	0.02	0.545
113	-0.05	0.20	0.02	0.682
122	-0.05	0.25	0.02	0.710
57	0.00	-0.25	0.02	0.662
48	0.00	-0.20	0.02	0.663
39	0.00	-0.15	0.02	0.560
105	0.00	0.15	0.02	0.541
114	0.00	0.20	0.02	0.619
123	0.00	0.25	0.02	0.636
56	0.05	-0.25	0.02	0.618
47	0.05	-0.20	0.02	0.570
38	0.05	-0.15	0.02	0.514
106	0.05	0.15	0.02	0.511
115	0.05	0.20	0.02	0.648
124	0.05	0.25	0.02	0.616
69	0.10	-0.25	0.02	0.682
68	0.10	-0.20	0.02	0.614
67	0.10	-0.15	0.02	0.560
107	0.10	0.15	0.02	0.511
116	0.10	0.20	0.02	0.590
125	0.10	0.25	0.02	0.627
78	0.15	-0.30	0.02	0.479
77	0.15	-0.25	0.02	0.696
76	0.15	-0.20	0.02	0.638
75	0.15	-0.15	0.02	0.583
74	0.15	-0.10	0.02	0.362
73	0.15	-0.05	0.02	0.350
72	0.15	0.00	0.02	0.382
71	0.15	0.05	0.02	0.271
70	0.15	0.10	0.02	0.447
108	0.15	0.15	0.02	0.585
117	0.15	0.20	0.02	0.652
126	0.15	0.25	0.02	0.626
130	0.15	0.30	0.02	0.485
87	0.20	-0.30	0.02	0.513
86	0.20	-0.25	0.02	0.666
85	0.20	-0.20	0.02	0.622
84	0.20	-0.15	0.02	0.641
83	0.20	-0.10	0.02	0.454
82	0.20	-0.05	0.02	0.539

81	0.20	0.00	0.02	0.461
80	0.20	0.05	0.02	0.408
79	0.20	0.10	0.02	0.487
109	0.20	0.15	0.02	0.642
118	0.20	0.20	0.02	0.678
127	0.20	0.25	0.02	0.693
131	0.20	0.30	0.02	0.526
96	0.25	-0.30	0.02	0.509
95	0.25	-0.25	0.02	0.667
94	0.25	-0.20	0.02	0.691
93	0.25	-0.15	0.02	0.610
92	0.25	-0.10	0.02	0.528
91	0.25	-0.05	0.02	0.457
90	0.25	0.00	0.02	0.424
89	0.25	0.05	0.02	0.421
88	0.25	0.10	0.02	0.457
110	0.25	0.15	0.02	0.665
119	0.25	0.20	0.02	0.676
128	0.25	0.25	0.02	0.696
132	0.25	0.30	0.02	0.577
99	0.30	-0.25	0.02	0.646
98	0.30	-0.20	0.02	0.670
97	0.30	-0.15	0.02	0.618
111	0.30	0.15	0.02	0.664
120	0.30	0.20	0.02	0.713
129	0.30	0.25	0.02	0.694

*velocity value normalized by the inflow velocity at the same height

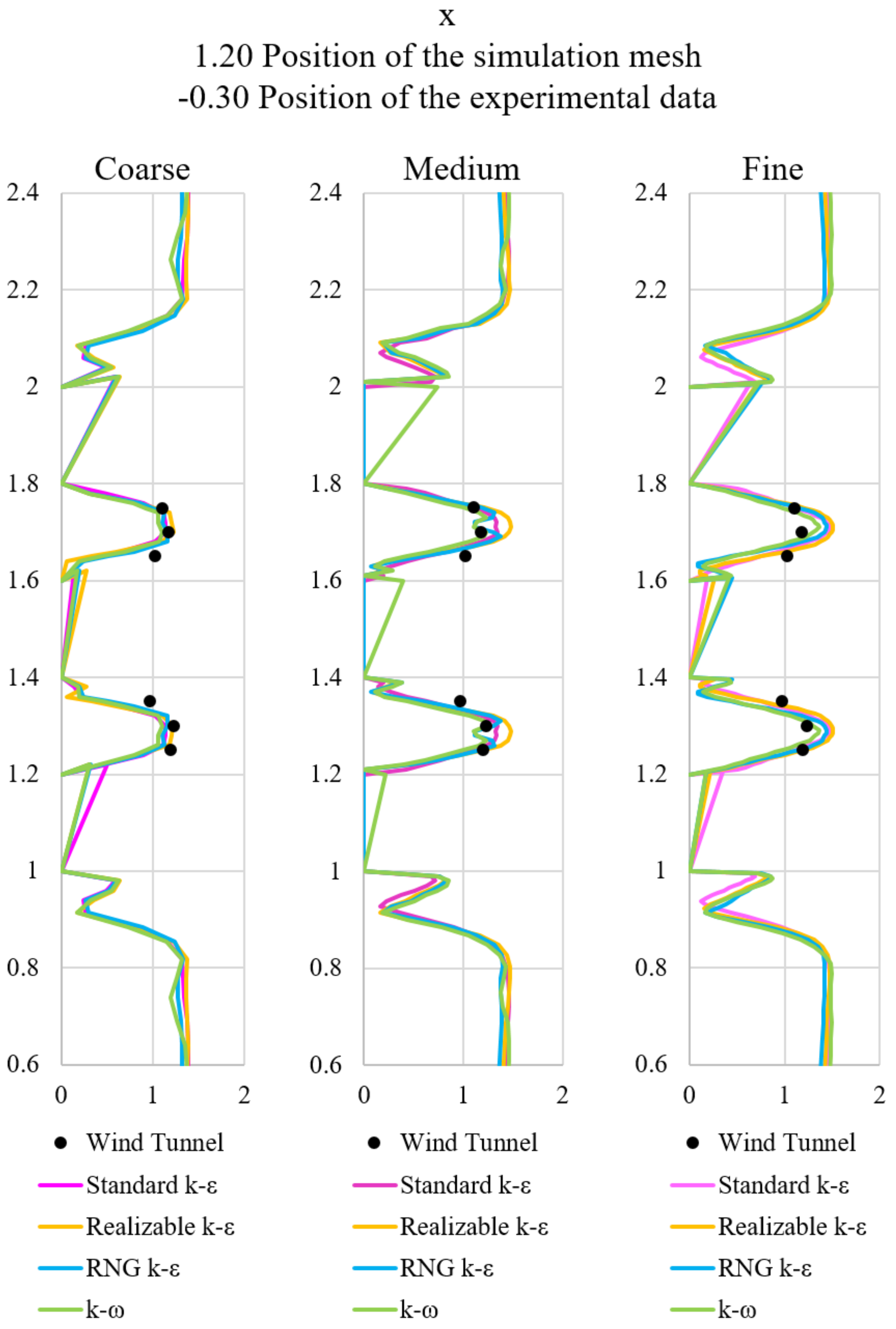

Figure A 2. Grid resolution study x = 1.20/-0.30

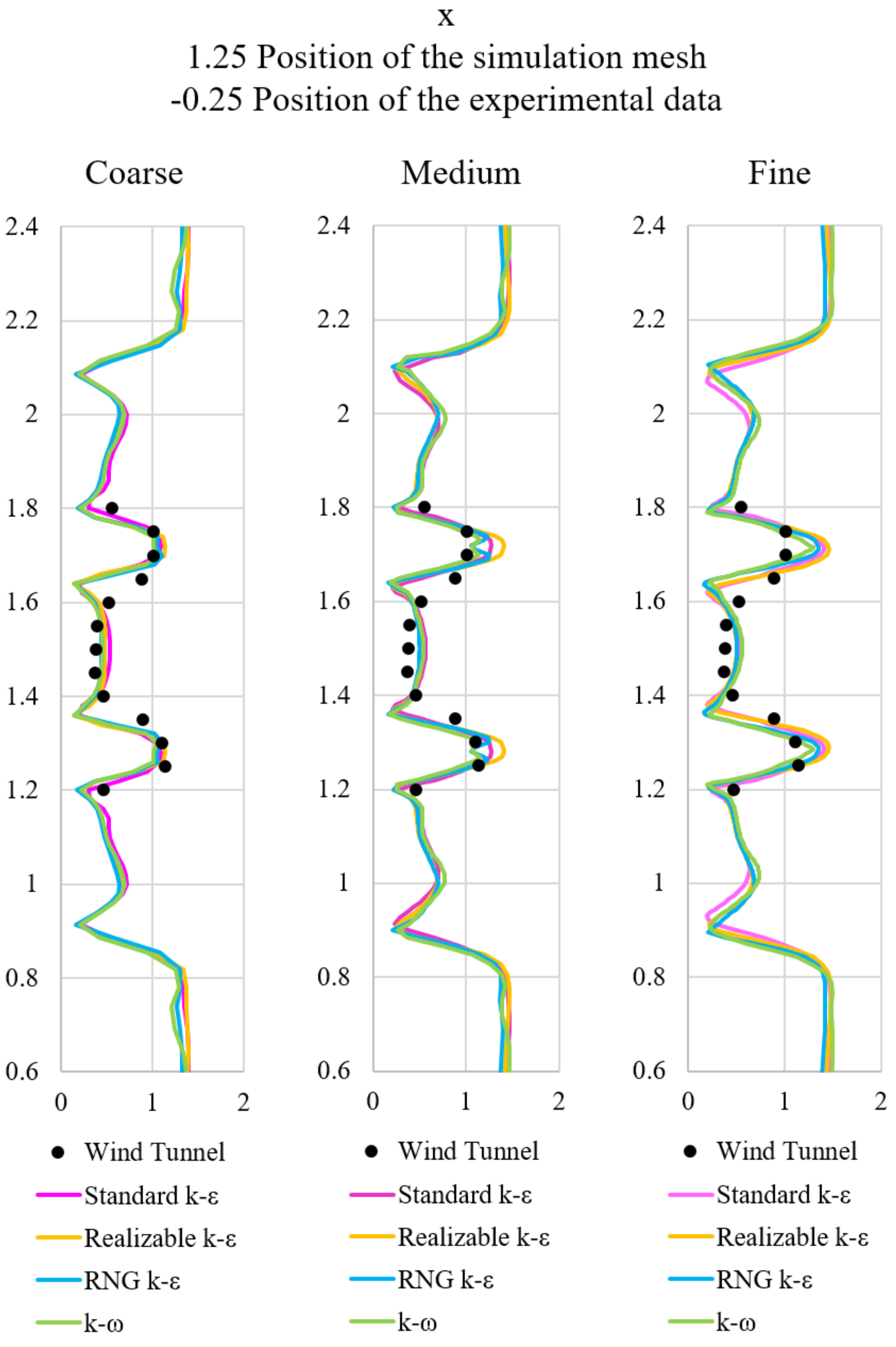

Figure A 3. Grid resolution study x = 1.25/-0.25

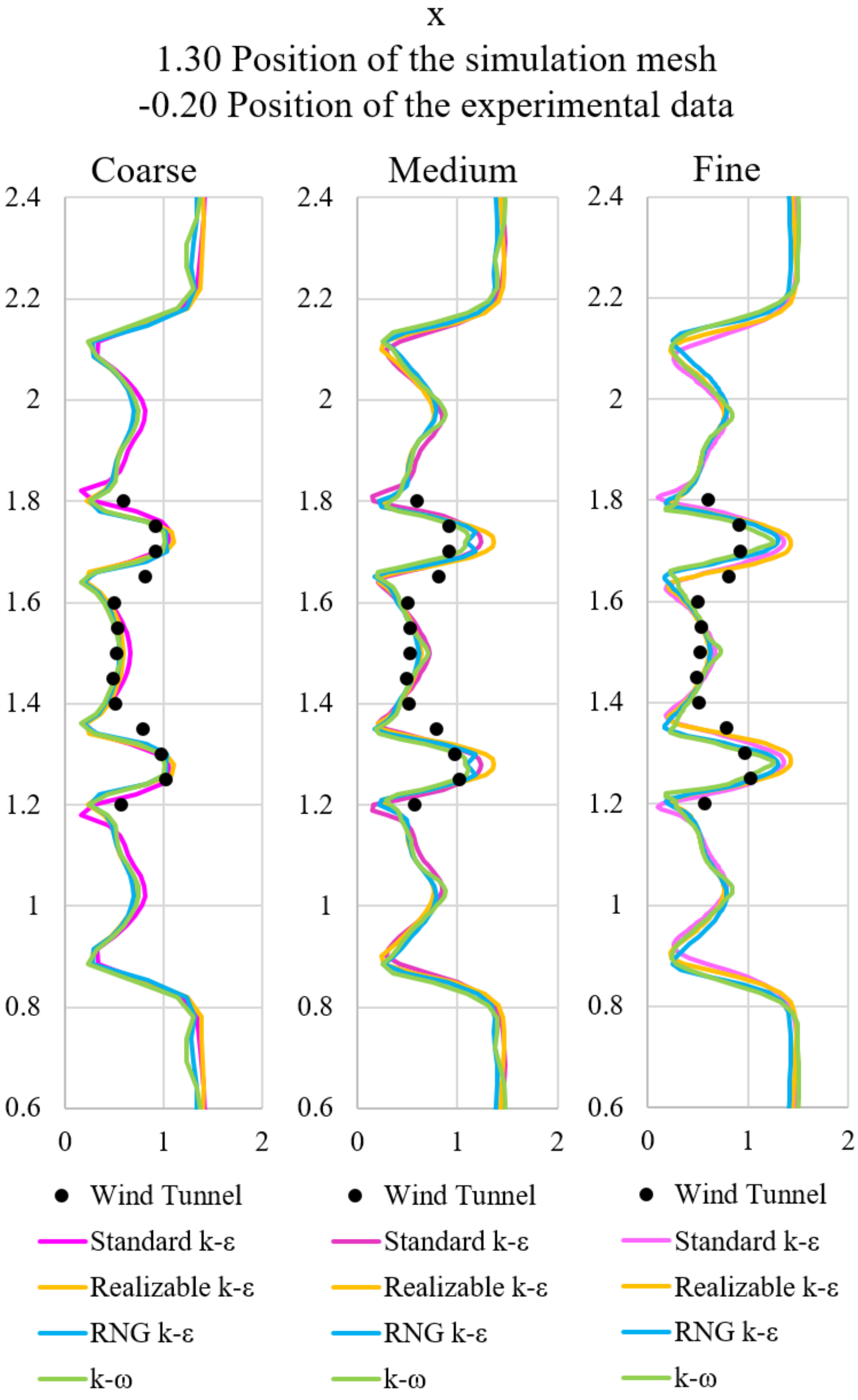

Figure A 4. Grid resolution study x = 1.30/-0.20

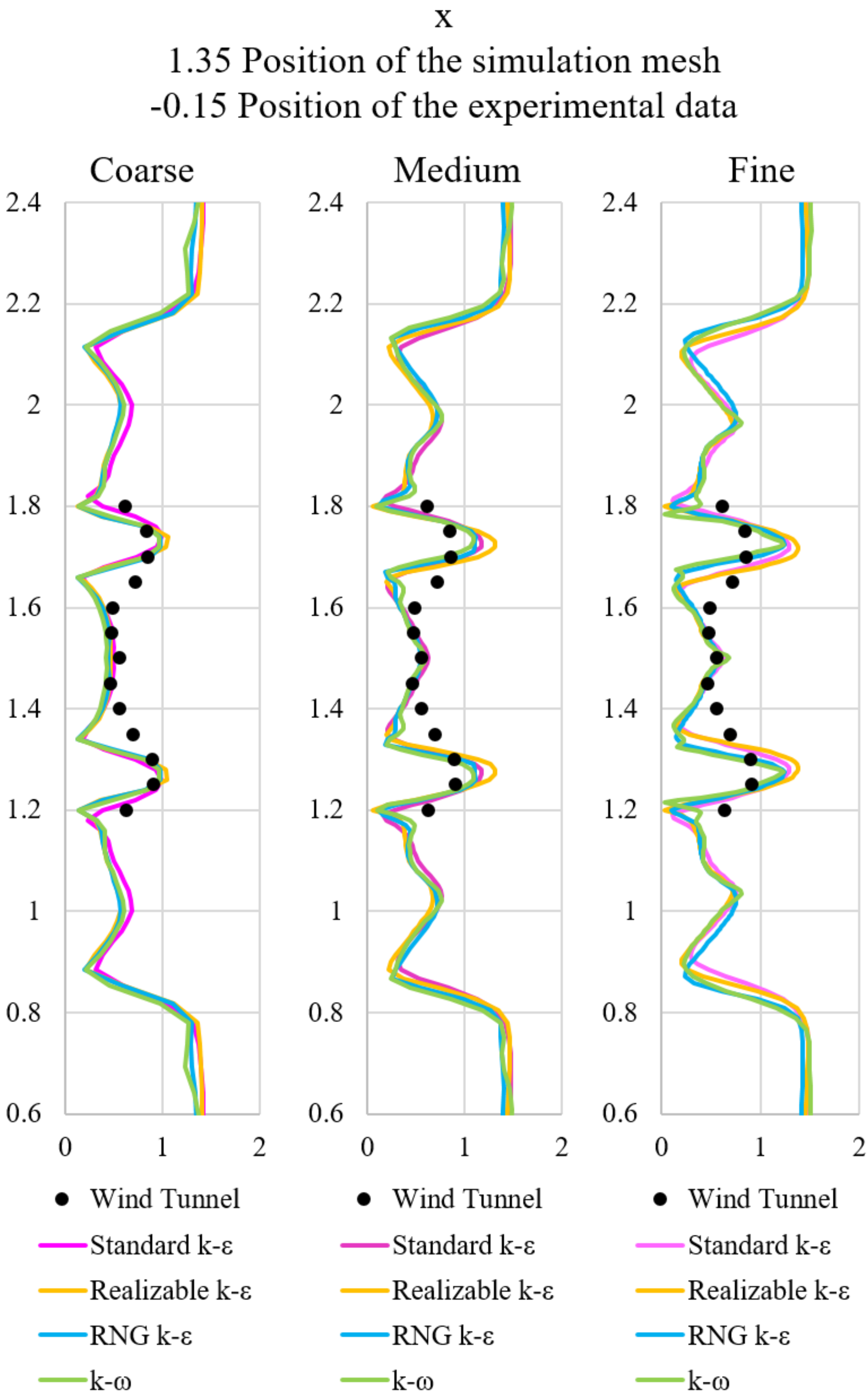

Figure A 5. Grid resolution study x = 1.35/-0.15

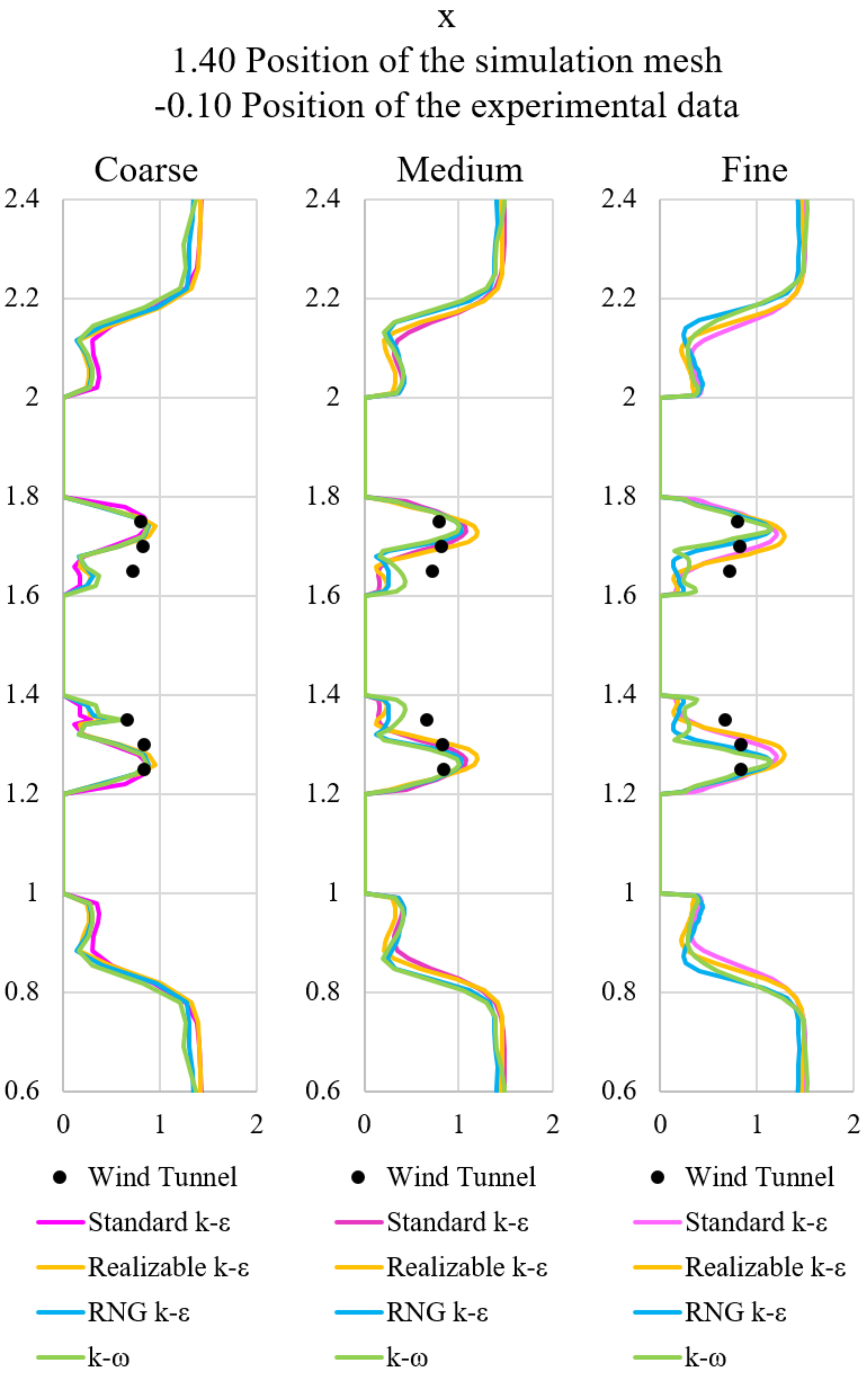

Figure A 6. Grid resolution study x = 1.40/-0.10

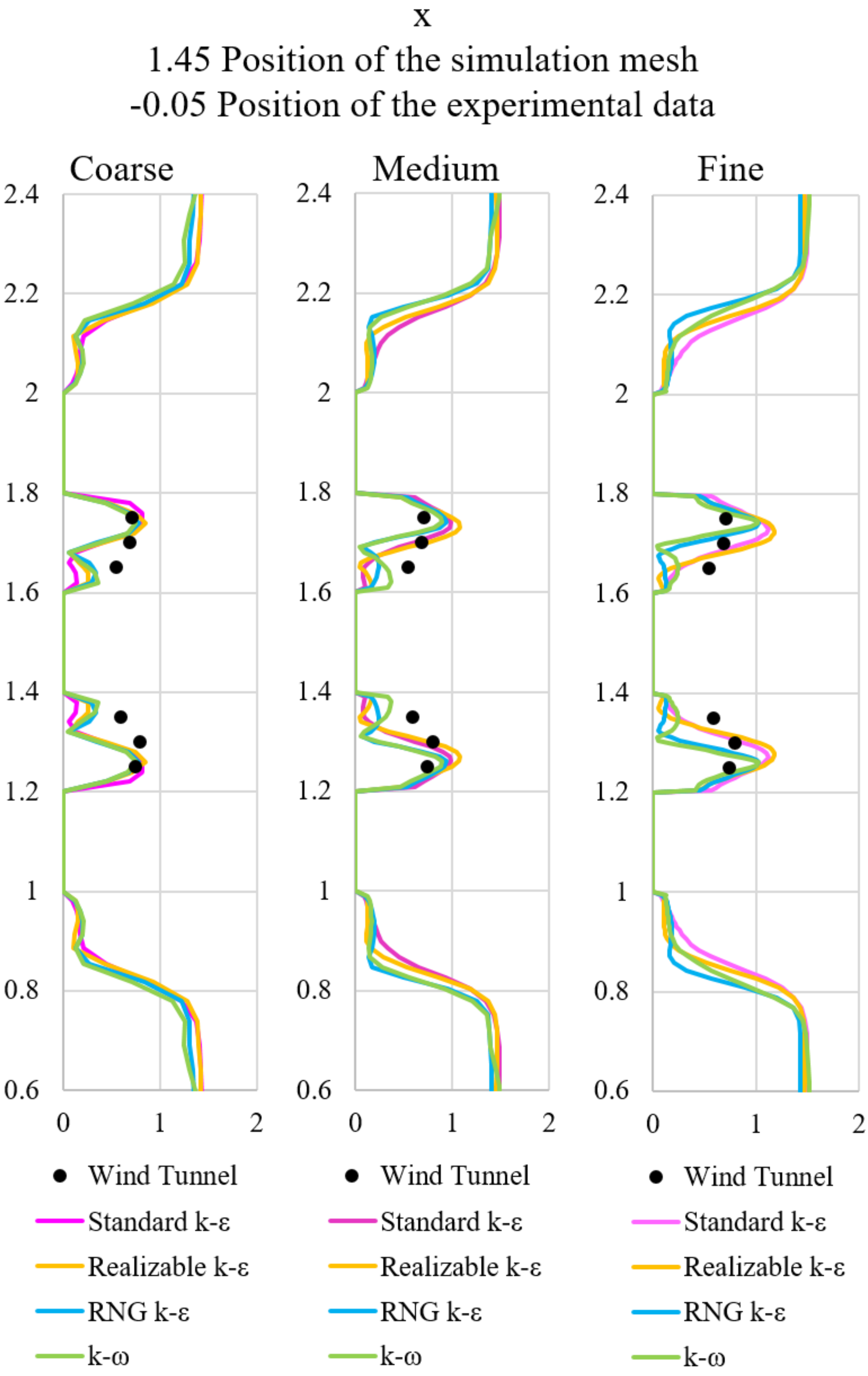

Figure A 7. Grid resolution study x = 1.45/-0.05

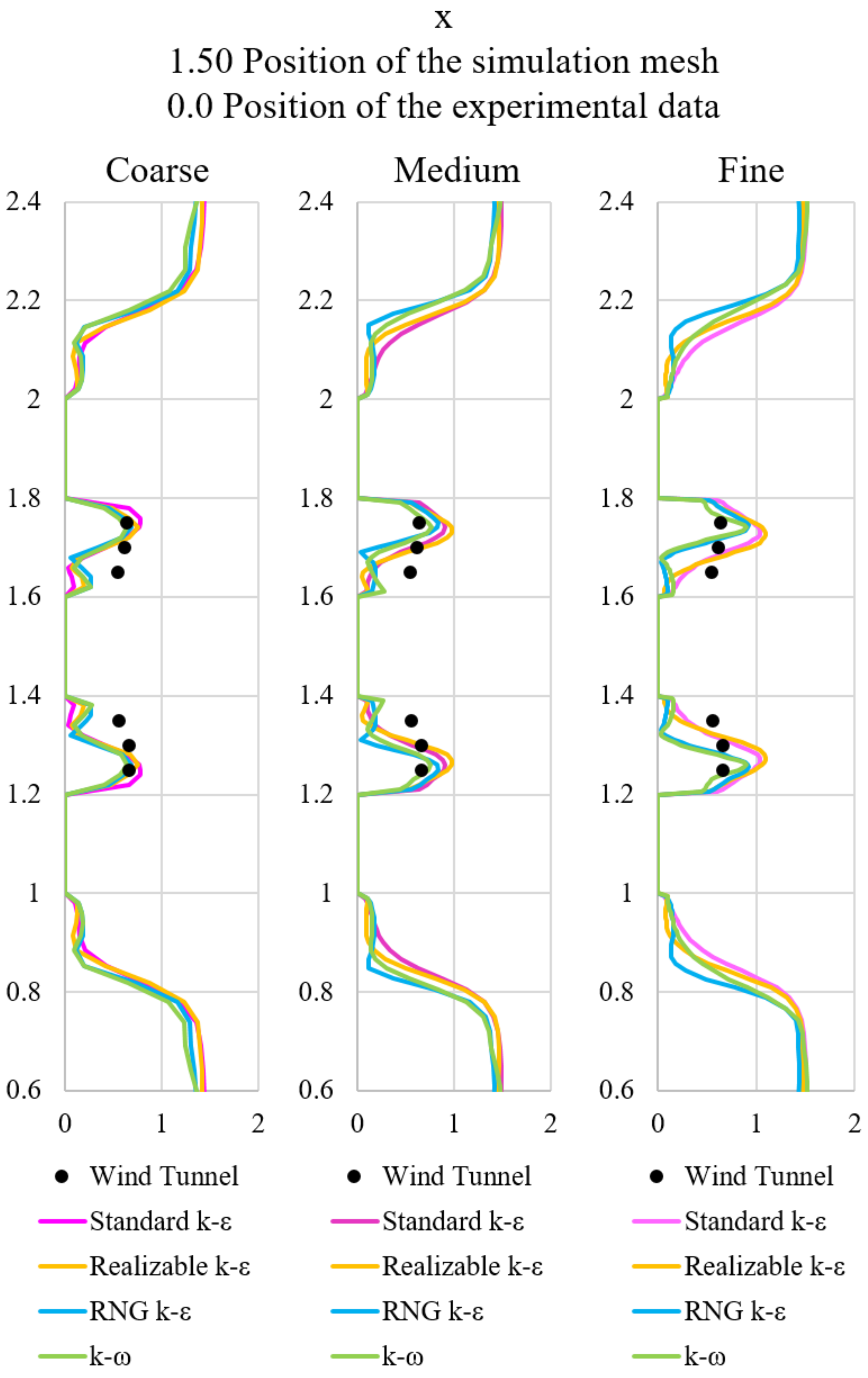

Figure A 8. Grid resolution study x = 1.50/0.0

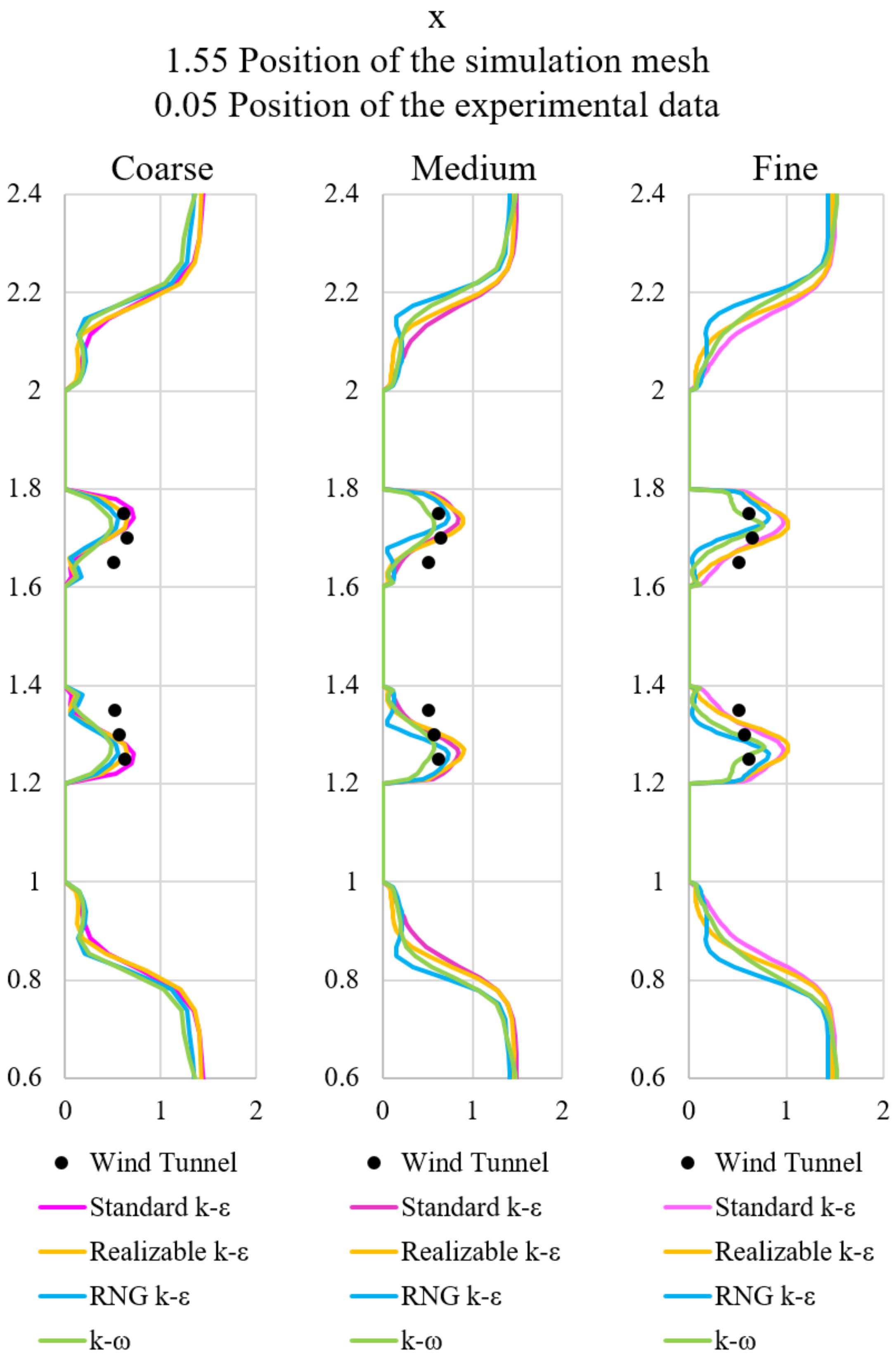

Figure A 9. Grid resolution study x = 1.55/0.05

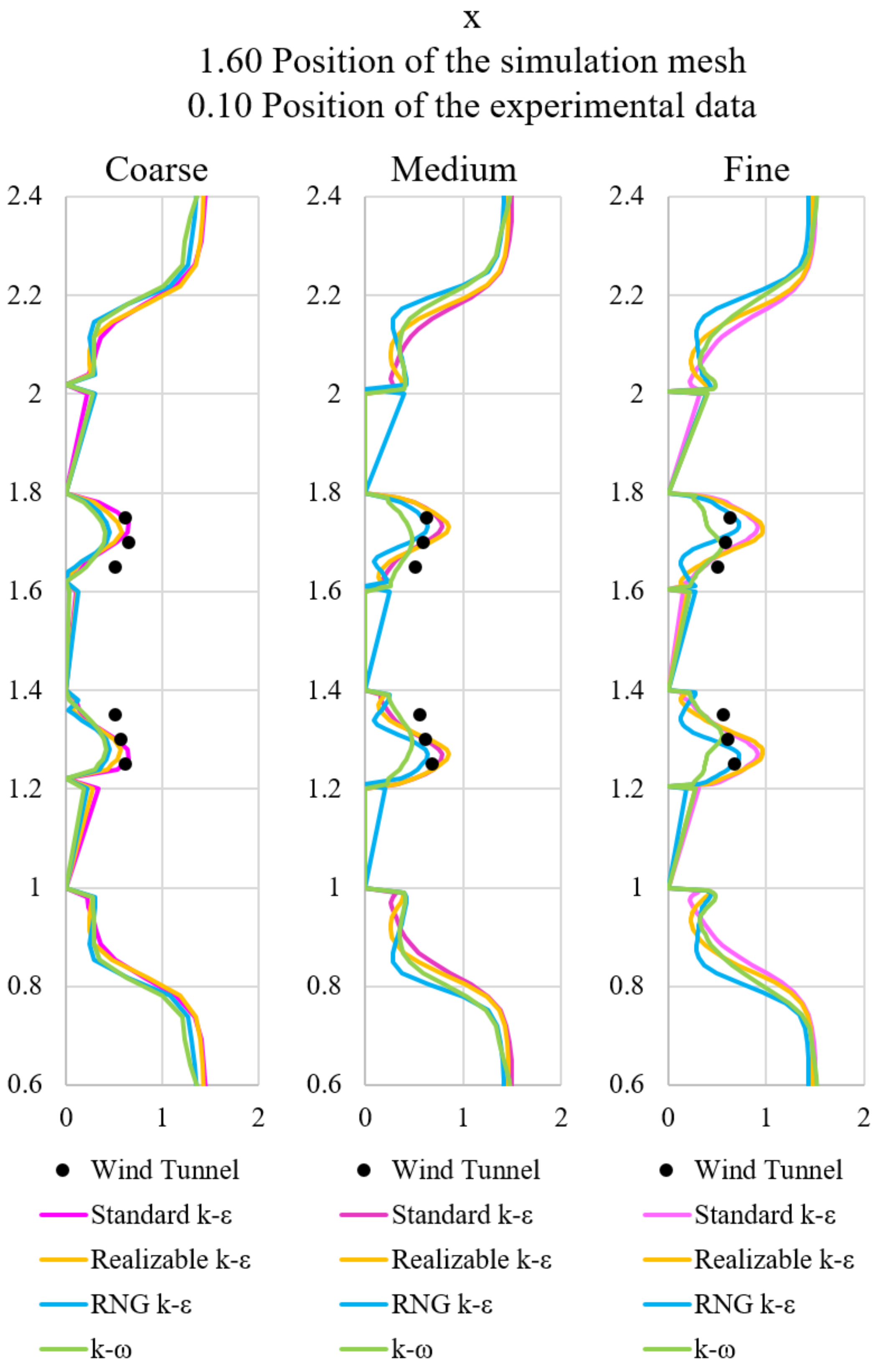

Figure A 10. Grid resolution study x = 1.60/0.10

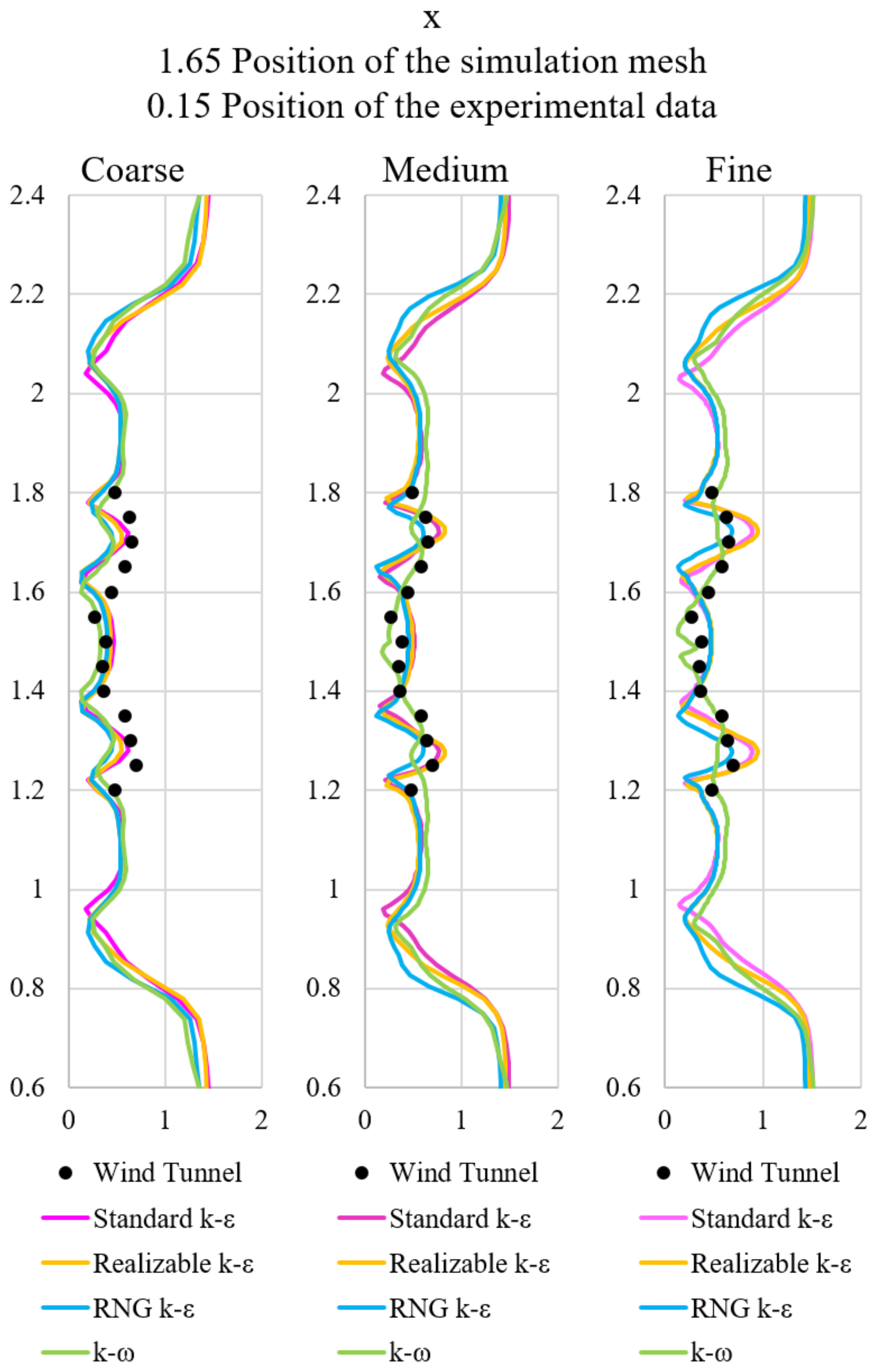

Figure A 11. Grid resolution study x = 1.65/0.15

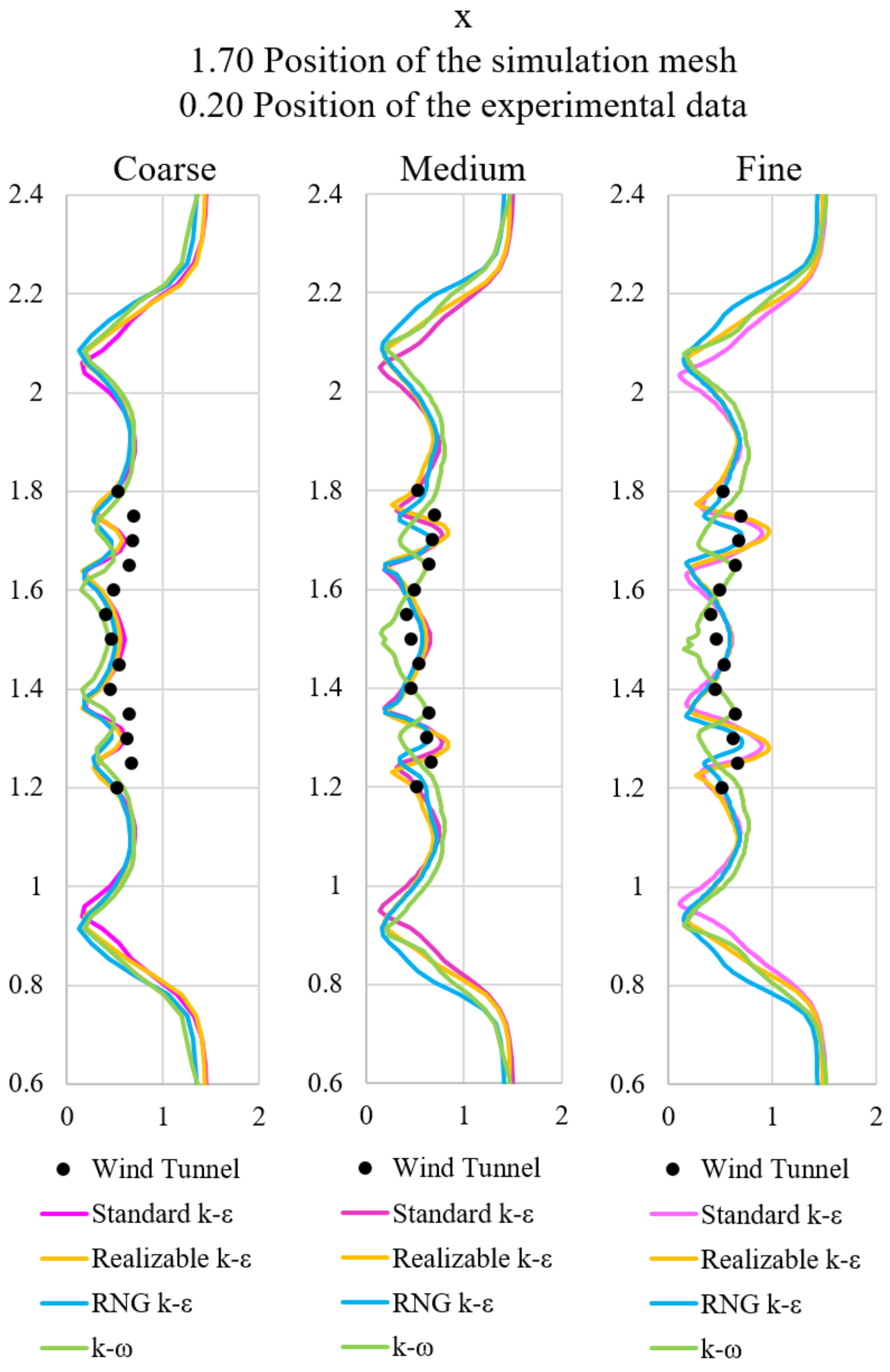

Figure A 12. Grid resolution study x = 1.70/0.20

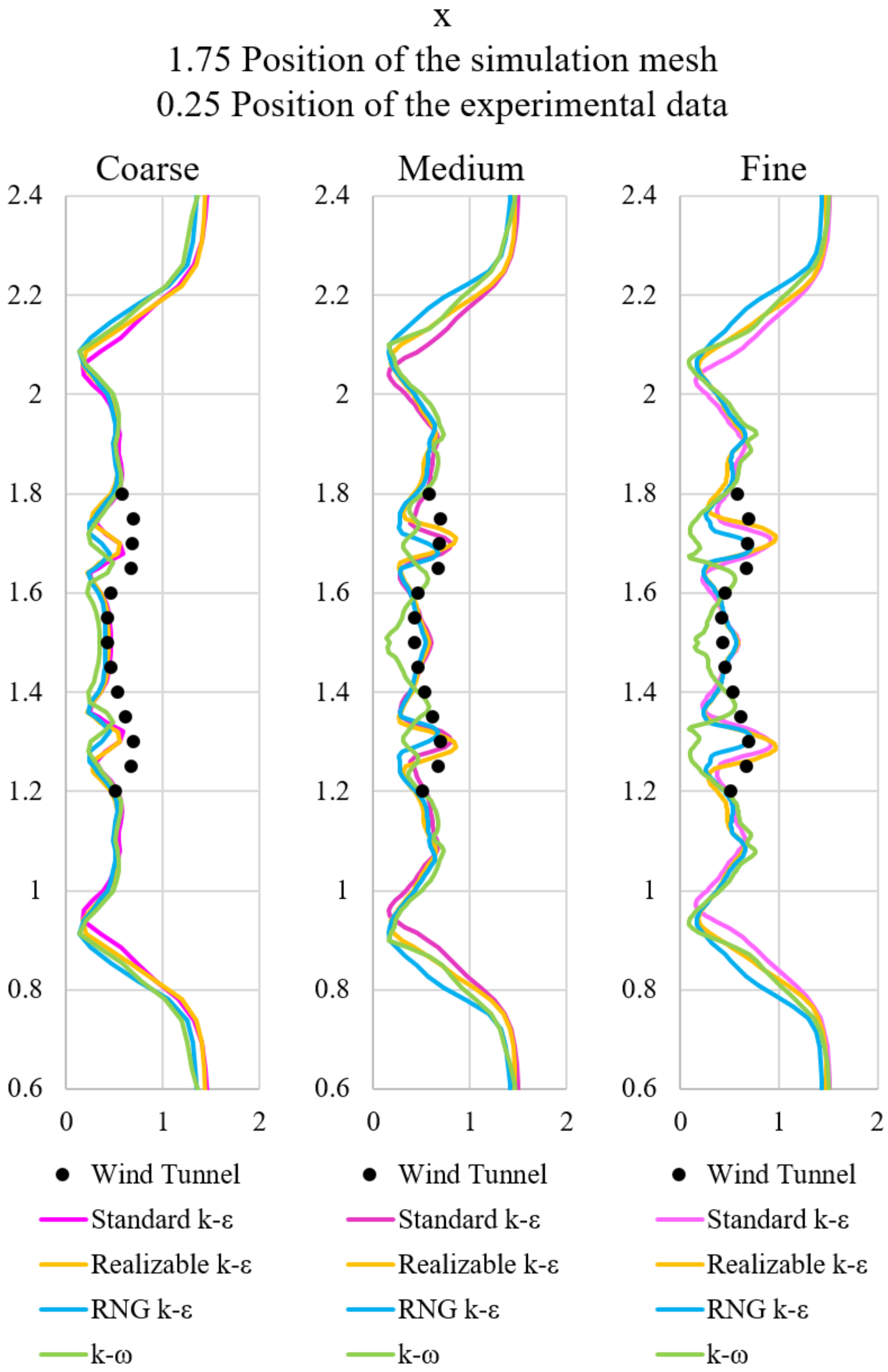

Figure A 13. Grid resolution study x = 1.75/0.25

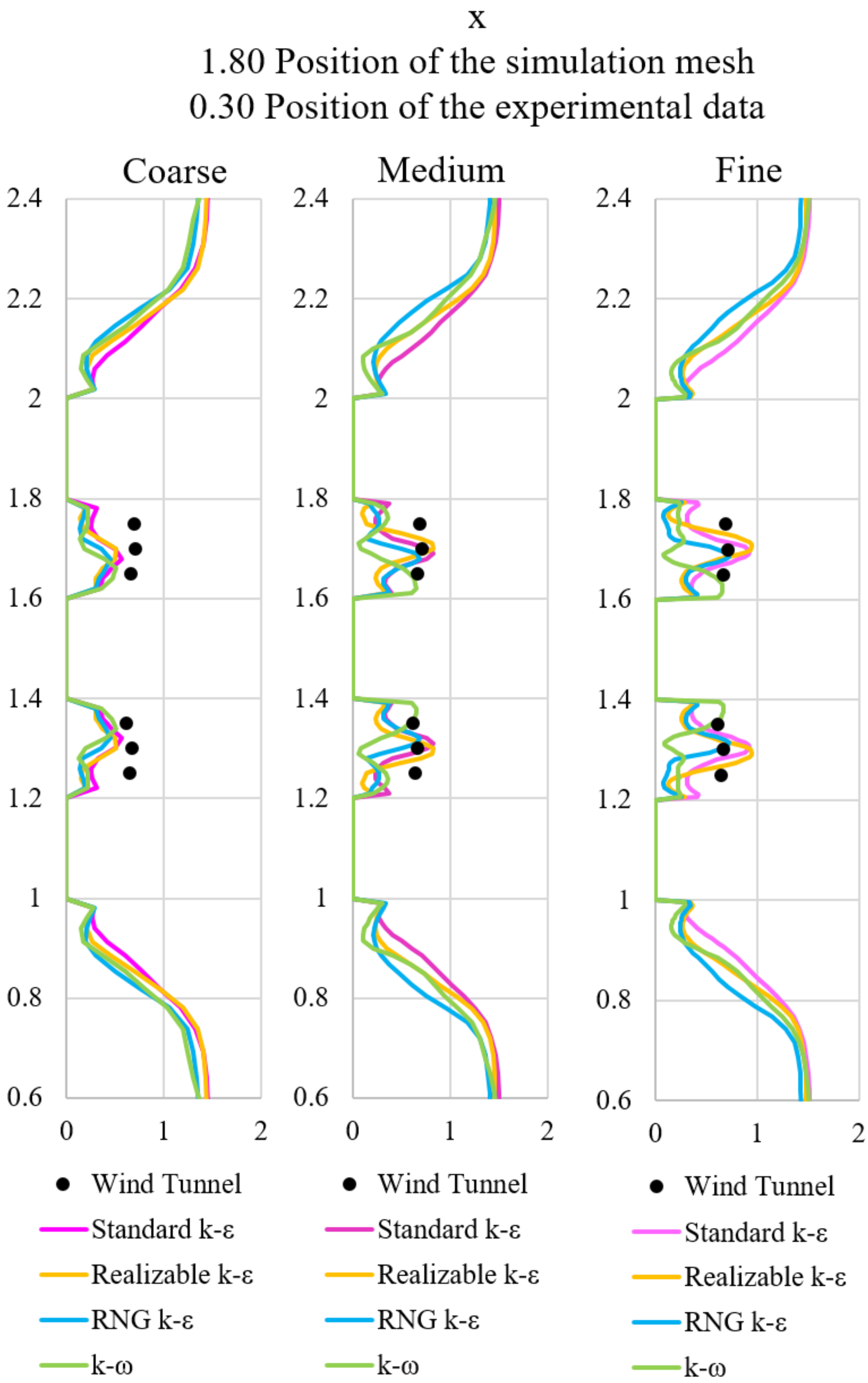

Figure A 14. Grid resolution study x = 1.80/0.30

APPENDIX B

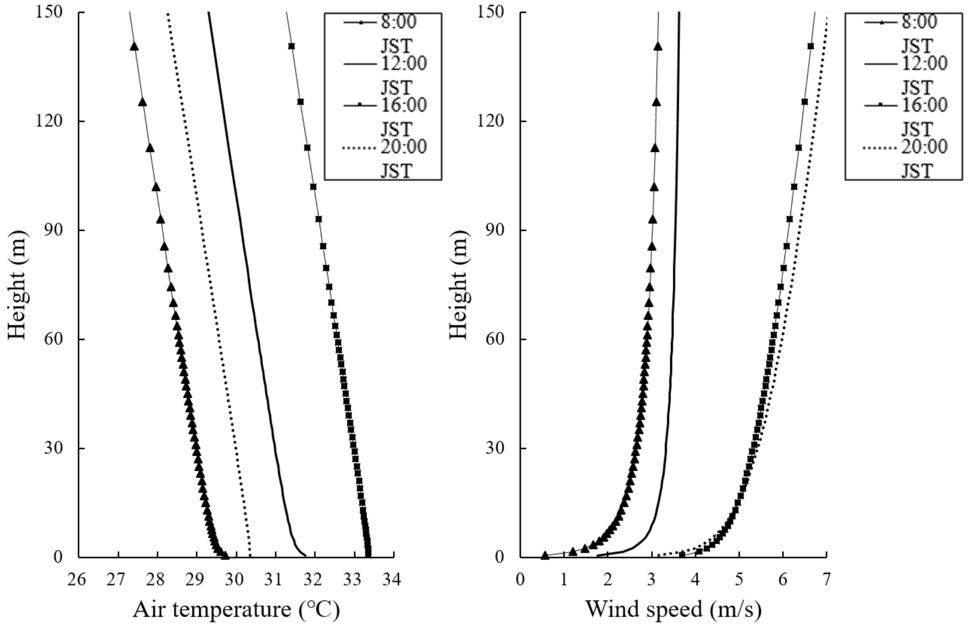

(a) (b)

Figure B 1. Boundary conditions for (a) air temperature and (b) wind speed at 08:00, 12:00, 16:00, and 20:00 JST.

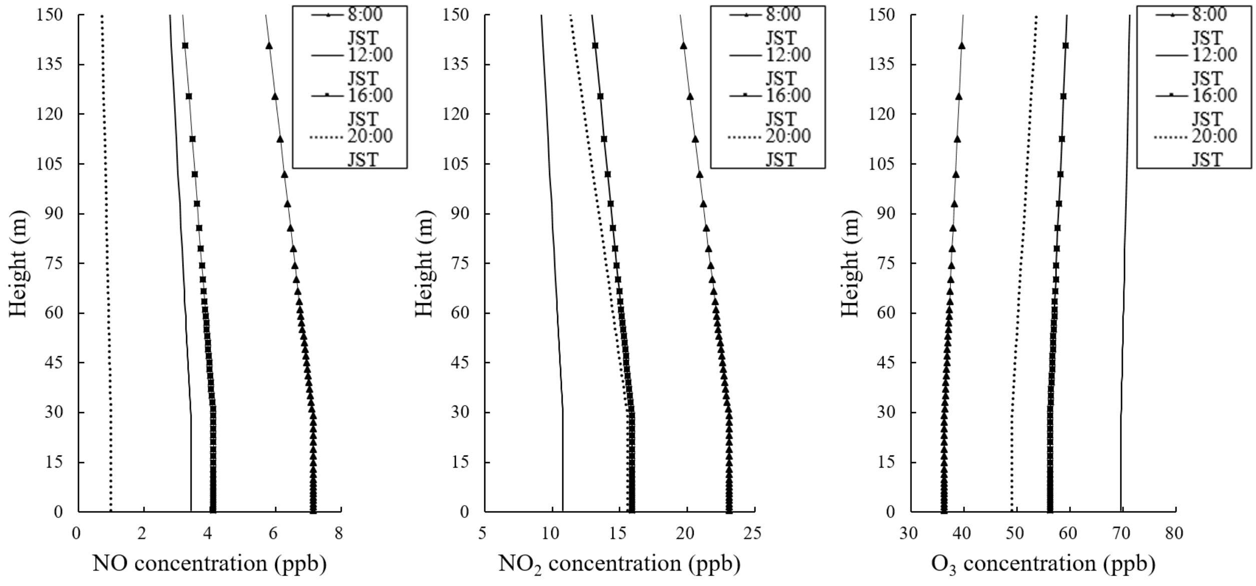

(a) (b) (c)

Figure B 2. Boundary conditions for (a) NO, (b) NO_2, and (c) O_3 concentrations at 08:00, 12:00, 16:00, and 20:00 JST

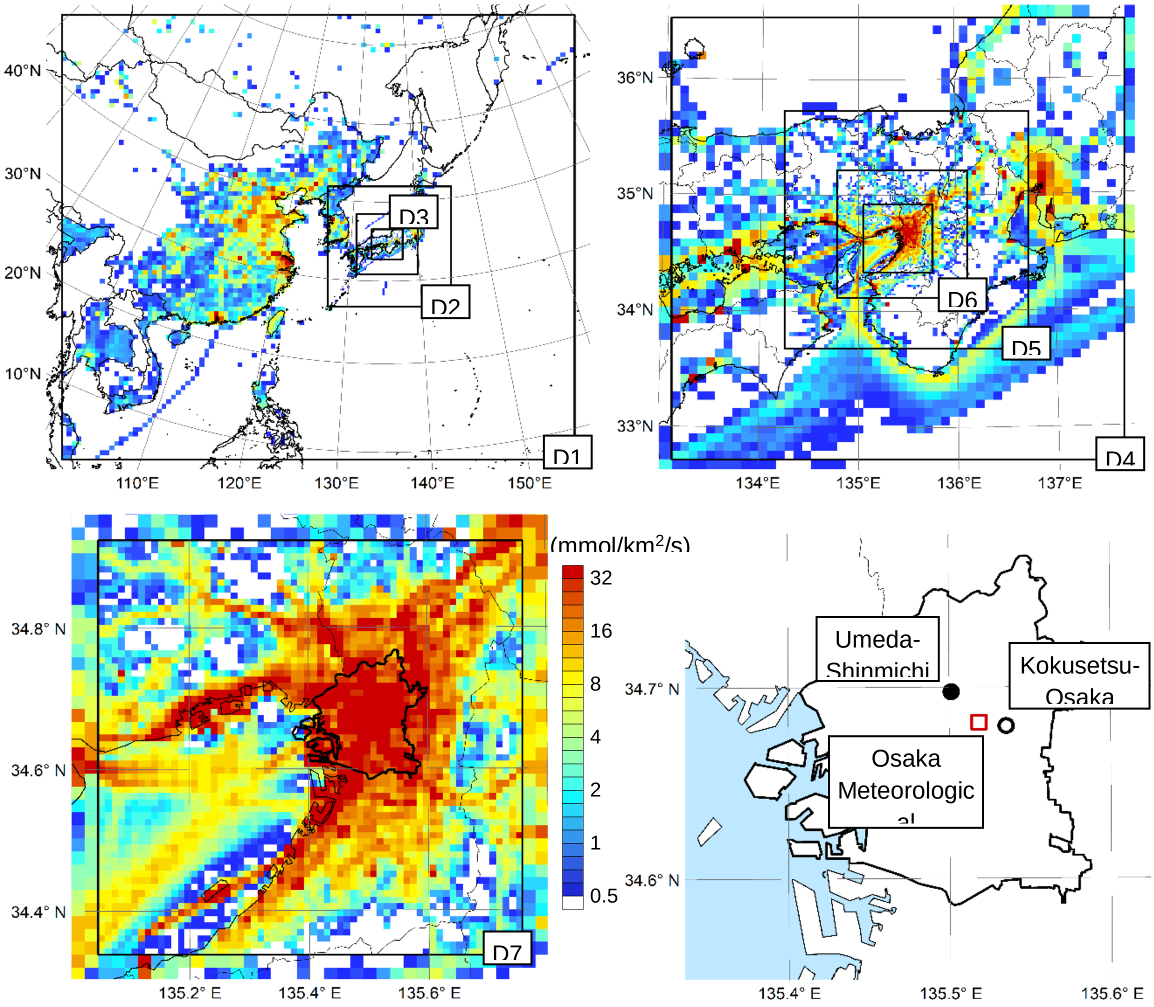

Figure B 3. Spatial distributions of mean NO_x emission intensity in CMAQ modeling domains from D1 covering East Asia to D7 covering Osaka Prefecture, and locations of observation sites in Osaka City used for model validations

Table B 1. WRF and CMAQ configurations

	Parameter	Setting
	Simulation period	June 24–August 31, 2010
	Map projection	Lambert conformal conic
	Horizontal grid spacing	64 (D1), 32 (D2), 16 (D3), 8 (D4), 4 (D5), 2 (D6), 1 (D7) km
	Vertical domain	Surface to 100 hPa with 30 layers (middle height of 1st, 2nd, 3rd layer ≅ 28, 92, 190 m)
WRF v3.7	Horizontal grid number	120 × 108 (D1), 64 × 64 (D2), 64 × 64 (D3), 64 × 64 (D4), 68 × 68 (D5), 72 × 72 (D6), 76 × 76 (D7)
	Topography / Landuse	30″ data by United States Geological Survey (USGS) / 30″ data by USGS, 100-m data by Geospatial Information Authority of Japan
	Initial and boundary	Atmosphere over Japan: Mesoscale model grid point value data by JMA; Sea surface temperature: High-resolution, real-time, global sea surface temperature analysis data by U.S. National Centers for Environmental Prediction (NCEP); Others: Final operational global analysis data by NCEP
	Grid nudging	G_{uv} = 3.0 (D1), 3.0 (D2), 3.0 (D3), 2.4 (D4), 1.2 (D5), 0.6 (D6), 0.3 (D7) × 10^{-4} s^{-1} for the entire simulation period and vertical layers
	Microphysics	WRF single-moment 6-class scheme
	Cumulus	Kain-Fritsch scheme (D1, D2, D3)
	Planetary boundary layer	Yonsei University scheme
	Surface	Noah land surface model
	Long- / Short-wave radiation	Rapid radiative transfer model / Dudhia scheme
CMAQ v5.1	Horizontal grid number	108 × 96 (D1), 52 × 52 (D2), 52 × 52 (D3), 52 × 52 (D4), 56 × 56 (D5), 60 × 60 (D6), 64 × 64 (D7)
	Meteorology	Hourly WRF output data processed with Meteorology-Chemistry Interface Processor v4.3

Initial and boundary	Model for Ozone and Related Chemical Tracers v4
Emission	Anthropogenic in Japan: JEI-DB (vehicle), Emission inventory by Ocean Policy Research Foundation (ship), EAGrid2010-JAPAN (others); Anthropogenic outside Japan: Emission inventory for Hemispheric Transport of Air Pollution v2; Biogenic: Model of Emissions of Gases and Aerosols from Nature v2.04
Gas phase chemistry	CB05
Aerosol phase chemistry	Sixth generation CMAQ aerosol module

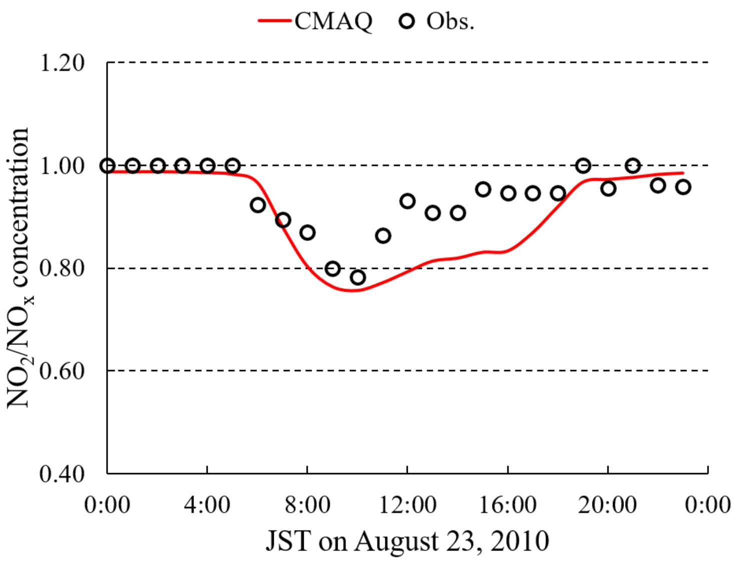

Figure B 4. Diurnal variations of the CMAQ-simulated and observed NO_2/NO_x concentration ratio at the Kokusetsu-Osaka station for monitoring ambient air pollution on 23 August 2010

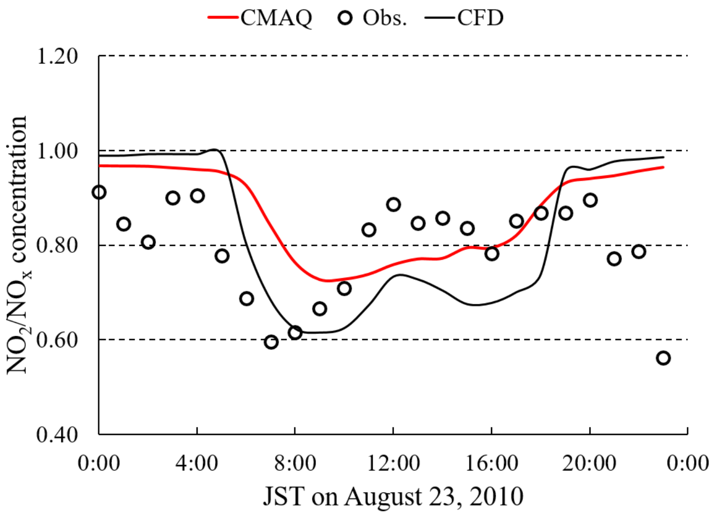

Figure B 5. Diurnal variations of the CMAQ-simulated, observed and CFD-simulated NO_2/NO_x concentration ratio at the Umeda-Shinmichi station for monitoring roadside air pollution on 23 August 2010

Figure B 4 shows the diurnal variations of the CMAQ-simulated and observed NO_2/NO_x concentration ratio at the Kokusetsu-Osaka station for monitoring ambient air pollution on 23 August 2010. Figure B 5 shows the diurnal variations of the CMAQ-simulated, observed and CFD-simulated NO_2/NO_x concentration ratio at the Umeda-Shinmichi station for monitoring roadside air pollution on 23 August 2010. In the morning hours, a sharp decrease of the NO_2/NO_x ratio is observed due to the increase of the NO_x emission rates related to the morning traffic (Figure 5.5). In the night hours, due to the NO_x titration an increase of the NO_2/NO_x

ratio is observed. Figure B 4 and Figure B 5 demonstrate the behavior of the reactive pollutants (NO, NO_2 and O_3) depending on the time of the day and the NO_x emission rates.

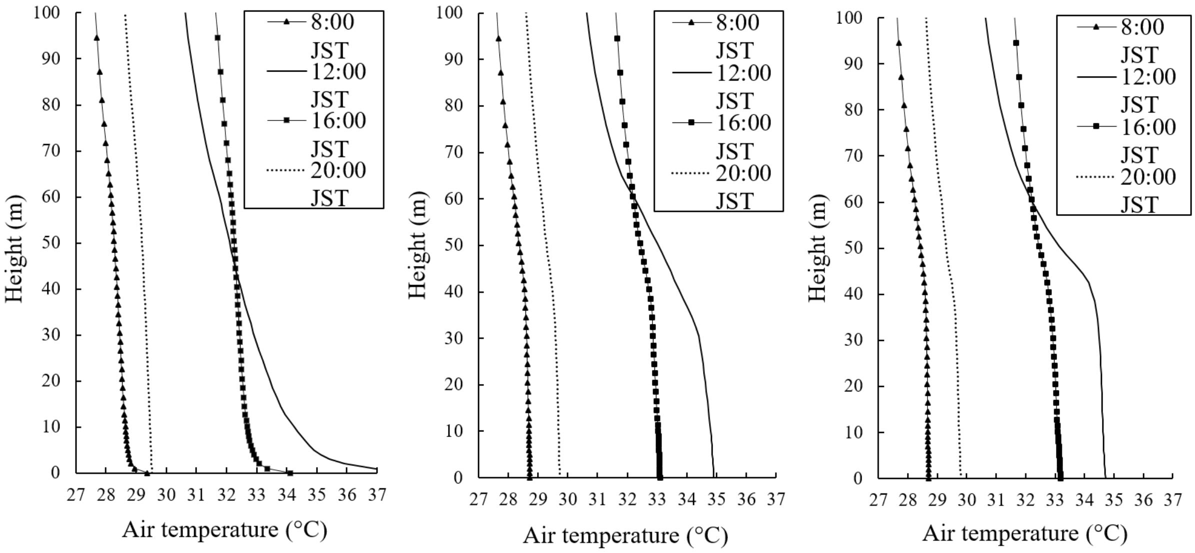

(a) (b) (c)

Figure B 6. Vertical air temperature profiles at 08:00, 12:00, 16:00, and 20:00 JST on National Route 25 for the points a) P1 located at y = 230 m; b) P2 located at y = 350 m; c) P3 located at y = 390 m (Figure 2a).

Figure B 6 shows the vertical air temperature profiles as a result of the surface energy model and the building envelope model at 08:00, 12:00, 16:00, and 20:00 JST for the reference points P_1 (y= 230 m), P_2 (y= 350 m), and P_3 (y= 390 m), located in the middle of National Route 25 as indicated in Figure 5.2a. The three locations showed higher temperatures at 12:00 JST and 16:00 JST. The high temperature on the road at 12:00 JST is because of the sun position overhead, and at 16:00 JST, because of the radiation already absorbed by buildings. In location P_1 (y= 230 m), the air temperature shows a different profile in comparison with P_2 and P_3 due to the free circulation of the wind in the southern part of the analysis area. At locations P_2 (y= 350 m) and P_3 (y= 390 m), the air temperature decreases when moving away from the surface level, especially when above the level of the building roof (~30 meters). At 12:00 JST, the slight westerly wind coming in the north of the urban canyon gives a reduction in the air temperature, but at the same time a wind flowing from south to east (Figure 5.3 and Figure 5.7) in the street canyon prevents the westerly wind from reaching further into the street canyon. At 16:00 JST, hot air is moved from the middle of the street canyon to northern areas, as a consequence, the air temperature at location P_3 (y = 390 m) is slightly higher than at location P_2 (y= 350 m).